

Ph.D. Thesis

**REGION OF INTEREST BASED PET IMAGE
COMPRESSION USING LINEARLY PREDICTED
WAVELET COEFFICIENTS**

Submitted to

COCHIN UNIVERSITY OF SCIENCE AND TECHNOLOGY

for the award of the degree of

Doctor of Philosophy

by

ARYA DEVI P. S.

Under the guidance of

Dr. Mini M. G.

RESEARCH GUIDE
DEPARTMENT OF ELECTRONICS
MODEL ENGINEERING COLLEGE
COCHIN – 682 021, INDIA

FEBRUARY 2016

**REGION OF INTEREST BASED PET IMAGE COMPRESSION USING LINEARLY
PREDICTED WAVELET COEFFICIENTS**

Ph.D. Thesis in the field of Molecular Image Compression

Author

Arya Devi P.S.
Research Scholar
Department of Electronics Engineering
Model Engineering College
Cochin,– 682 021, India
e-mail: aryaps@mec.ac.in

Research Advisor

Dr. M. G. Mini
Research Guide
Department of Electronics Engineering
Model Engineering College
Cochin,– 682 021, India
e-mail : mininair@mec.ac.in

February, 2016

Dedicated to.....

My Parents, Husband & Kid

CERTIFICATE

This is to certify that this thesis entitled, ***Region of Interest based PET image Compression using Linearly Predicted Wavelet Coefficients*** is a bonafide record of the research work carried out by Ms. Arya Devi P.S. under my supervision in the Department of Electronics, Model Engineering College, Kochi. The result presented in this thesis or parts of it have not been presented for any other degree(s) from any other university.

I further certify that the corrections and modifications suggested by the audience during pre-synopsis seminar and recommended by the Doctoral committee of Ms. Arya Devi. P. S are incorporated in this thesis.

Cochin - 682021
29th February 2016

Dr. M.G. Mini
Supervising Guide

DECLARATION

I hereby declare that the work presented in this thesis entitled *Region of Interest based PET image Compression using Linearly Predicted Wavelet Coefficients* is a bonafide record of the research work carried out by me under the supervision of Dr. M.G. Mini, Associate Professor, in the Department of Electronics Engineering, College of Engineering, Cherthala and Research Guide, Model Engineering College, Thrikkakkara. The result presented in this thesis or parts of it have not been presented for other degree(s) from any other institutions.

ARYA DEVI P. S.

Cochin – 21
29th February 2016

Acknowledgements

I would like to express my deepest sense of gratitude to my research guide, **Dr. M.G. Mini**, HOD, Department of Electronics Engineering, Cherthala for her excellent guidance and incessant encouragement. It has been a great pleasure and privilege to work under her and she was always there whenever I needed help.

I am much grateful to **Prof. (Dr.) V. P. Devassia**, Principal, Model Engineering College, for the whole hearted support and constant encouragement.

I would like to express my sincere thanks to **Dr. Jayasree V.K. and Dr. Jayachandran E.S.**, former Heads, Department of Electronics Engineering, Model Engineering College, for their valuable suggestions and constant support and encouragement rendered to me.

Sincere thanks are due to **Dr. Vinu Thomas**, Assoc. Professor, Department of Electronics Engineering, Model Engineering College and **Dr. Jessy John**, HOD, Biomedical Engineering, Model Engineering College, for providing adequate help and fruitful suggestions.

I take this opportunity to express my sincere thanks to **Mr. Binesh T. and Ms. Bindu C.J.**, Asst. Professors, Model Engineering College for the constant encouragement and support rendered to me.

I immensely acknowledge the financial assistance rendered by **Kerala State Council for Science, Technology and Environment (KSCSTE)**, Thiruvananthapuram for carrying out some of the activities reported in this thesis.

A word of mention is deserved by Ms. Rekha Lakshmanan, my fellow researcher who has been a constant support and encouragement throughout my research period.

I thank all the research scholars of the department, especially Mrs. Aparna Devi P. S, Mrs. Jibi John, Mrs. Shiji T P, Mr. Jagadeeshkumar P and Mr. Joseph George K N for their friendly and supportive attitude.

I thankfully bear in mind the sincere co-operation and support I received from the **library and administrative staff** of Model Engineering College, Thrikkakkara.

It is beyond words to express my gratitude to my parents, my husband and Chinnu for their sacrifice in connection with preparation of my thesis. I am sure I could not have completed this great task without their support and cooperation. I also thank my in-laws for their support and understanding.

ARYA DEVI P.S

ABSTRACT

Objective: Positron Emission Tomography (PET) is a nuclear medicine technique, which can be used to visualize pathologies at much finer molecular level. Compressing a medical image is a challenging task as loss of vital data needed for correct diagnosis can not be tolerated. Even though compression with high compression ratio (cr) is more efficient in terms of storage and transmission needs, there is no guarantee to preserve the characteristics needed in medical diagnosis. The diagnostically important region, i.e., region of interest (ROI) of the image is compressed with low cr and the remaining part of the image, i.e., background (BG) is compressed with high cr , so that useful information is preserved and high cr is obtained.

Method: The proposed system develops a ROI based compression technique for PET images, based on wavelet and linear prediction concepts. In the proposed system, the image is enhanced and segmented to obtain ROI. The enhancement technique developed is used as preprocessing technique to assist in obtaining a suitable ROI. The segmentation is difficult in case of PET images due to inherently poor spatial resolution and signal to noise ratio (SNR). A two stage segmentation technique having Gabor annulus filtering as first stage and region growing with automatic seed

selection as the second stage is developed and evaluated. A compression technique utilising linear prediction on wavelet coefficients, has been developed and its variants are studied. The image inside ROI is compressed with lower cr while BG is compressed with a higher cr . The three parts of the system- enhancement, segmentation and compression are integrated to suit PET images. An extension or modification of the work is carried out on mammographic images also. **Results:** The image quality is evaluated both subjectively and objectively. A PET image could be reduced to 4.5% of its original size. The enhancement, segmentation and compression techniques developed are also evaluated separately. The successful lesion capture rate achieved using this technique is 93.8% and missed out lesions are primarily located in the lungs. **Conclusions:** The proposed method is particularly suited to whole body PET images. With certain modifications, it could be applied to mammographic images also.

KEYWORDS: Linear Prediction; Positron Emission Tomography; Wavelet Transform; Region of Interest (ROI); Image Compression; Mammogram; Structural Similarity (SSIM); Enhancement; Segmentation; Region Growing; Gabor Annulus filtering; Peak Signal to Noise Ratio (PSNR).

Contents

	Page No
<i>Acknowledgements</i>	<i>ix</i>
<i>Abstract</i>	<i>xi</i>
<i>Contents</i>	<i>xiii</i>
<i>List of Figures</i>	<i>xvii</i>
<i>List of Tables</i>	<i>xxi</i>
<i>Abbreviations</i>	<i>xxiii</i>
CHAPTER 1	1
INTRODUCTION	1
1.1 Molecular imaging	1
1.1.1 Magnetic resonance imaging.....	2
1.1.2 Optical imaging	3
1.1.3 Nuclear medicine techniques.....	3
1.1.4 Ultrasound imaging.....	4
1.2 Medical images and processing	5
1.2.1 PET Imaging.....	6
1.2.2 X-ray mammography.....	15
1.2.3 Image processing techniques.....	19
1.3 Need for compression	22
1.4 Motivation	23
1.5 Objective of the work	24
1.6 Layout of the Thesis	25
CHAPTER 2	27
LITERATURE REVIEW	27
2.1 Introduction	27
2.2 State of art on image enhancement	28
2.2.1 Image enhancement in PET images.....	28
2.2.2 Image enhancement in mammograms.....	31
2.3 Literature survey on image segmentation	35

2.3.1	Segmentation techniques on PET images.....	36
2.3.2	Segmentation of breast region from mammographic images.....	38
2.4	Current trends in image compression.....	41
2.5	Conclusion.....	50
	CHAPTER 3.....	51
	IMAGE ENHANCEMENT USING STATIONARY WAVELET TRANSFORM AND UNSHARP MASKING.....	51
3.1	Introduction.....	51
3.2	Background.....	53
3.2.1	Image enhancement techniques used with medical images.....	53
3.2.2	Stationary wavelet transform.....	56
3.2.3	Modulus maxima and Detail modulus.....	59
3.2.4	Unsharp masking.....	60
3.3	Measures to quantify image enhancement techniques.....	62
3.4	Proposed enhancement using SWT and unsharp masking.....	64
3.4.1	Enhancement of PET images.....	66
3.4.2	Enhancement of mammographic images.....	67
3.5	Results and Discussion.....	68
3.5.1	PET images.....	68
3.5.2	Mammographic images	72
3.6	Conclusion.....	78
	CHAPTER 4.....	79
	SEGMENTATION OF REGION OF INTEREST.....	79
4.1	Introduction.....	79
4.2	Framework.....	81
4.2.1	Widely used segmentation methods with medical images.....	81
4.2.2	Gabor annulus filtering.....	82
4.2.3	Region growing.....	84
4.2.4	Eccentricity.....	86
4.3	Evaluation of segmentation techniques.....	87

4.4	Segmentation approach for ROI separation in PET images.....	90
4.4.1	Experimental determination of GA filter parameters.....	93
4.4.2	Unsupervised evaluation and results.....	94
4.4.3	Comparison using CREASEG software.....	102
4.5	Augmentation of developed approach X-ray images.....	108
4.5.1	Results and Discussion.....	110
4.6	Conclusion.....	112
CHAPTER 5.....		113
COMPRESSION TECHNIQUES		113
5.1	Introduction.....	113
5.2	Basic Compression.....	113
5.2.1	Compression models.....	114
5.2.2	Image compression techniques.....	117
5.3	Wavelet and related concepts.....	118
5.3.1	Basic definition of wavelet transform.....	120
5.3.2	One dimensional DWT (1D DWT).....	120
5.3.3	Two dimensional DWT (2D DWT).....	122
5.3.4	Correlational properties of wavelet transform.....	123
5.4	Linear prediction.....	124
5.5	Performance measures.....	126
5.6	Compression techniques using linear prediction and DWT.....	129
5.6.1	Generalised algorithm steps.....	130
5.6.2	Row/column wise LP on row/column wise 1D DWT.....	132
5.6.3	Row and column wise LP on row/column wise 1D DWT.....	132
5.6.4	Row and column wise LP on 2D DWT.....	134
5.7	Results and Discussion.....	135
5.7.1	Row/column wise LP on row/column wise 1D DWT.....	135
5.7.2	Row and column wise LP on row/column wise 1D DWT.....	142
5.7.3	Row and column wise LP on 2D DWT.....	148
5.8	Conclusion.....	156

CHAPTER 6.....	159
ROI BASED IMAGE COMPRESSION.....	159
6.1 Introduction.....	159
6.2 Philosophy.....	159
6.2.1 Set Partioning in Heirarchial Trees (SPIHT) Algorithm.....	160
6.2.2 Arithmetic coding.....	163
6.2.3 Deflate algorithm.....	164
6.3 ROI based compression scheme for PET images.....	165
6.3.1 Results and Discussion.....	167
6.4 ROI based compression for mammograms.....	175
6.4.1 Results and Discussion.....	176
6.5 Conclusion.....	180
CHAPTER 7.....	181
CONCLUSIONS.....	181
7.1 Introduction.....	181
7.2 Summary, conclusions and future scope.....	181
7.2.1 PET image compression.....	181
7.2.2 Mammographic image compression.....	182
7.2.2 Future Scope.....	183
<i>References</i>	<i>185</i>
<i>Publications</i>	<i>197</i>
<i>Resume</i>.....	<i>199</i>

List of Figures

	Page No
Fig. 1.1 Images reconstructed from same raw data	8
Fig. 1.2 A random background event	9
Fig. 3.1 SWT decomposition and filters	57
Fig. 3.2 Two dimensional SWT decomposition and filters	58
Fig. 3.3 Decomposition and reconstruction using SWT	59
Fig. 3.4 Waveform in unsharp masking image enhancement system	61
Fig. 3.5 Generalised flow chart of proposed enhancement algorithm	65
Fig. 3.6 Result of proposed method	67
Fig. 3.7 Result of proposed method	68
Fig. 3.8 Original and enhanced slices having no lesion	69
Fig. 3.9 Original and enhanced slices having two lesions	69
Fig. 3.10 (a) Contrast of original and enhanced images having no lesion	70
Fig. 3.10 (b) Contrast of original and enhanced images having lesions	70
Fig. 3.11 (a) EMEE of original and enhanced images having no lesion	71
Fig. 3.11 (b) EMEE of original and enhanced images having lesions	71
Fig. 3.12 PSNR of images with and without lesions	72
Fig. 3.13 (a) Original and enhanced images having circumscribed masses	73
Fig. 3.13 (b) Original and enhanced images having microcalcification	73
Fig. 3.13 (c) Original and enhanced images having no abnormality	73
Fig. 3.13 (d) Original and enhanced images having architectural distortion	74
Fig. 3.13 (e) Original and enhanced images having spiculated masses	74
Fig. 3.14 Contrast comparison of original and enhanced images	76
Fig. 3.15 Comparison of EMEE for original and enhanced images	76
Fig. 3.16 Pie chart for CII	76
Fig. 3.17 PSNR comparison	77
Fig. 4.1 Block diagram of proposed method	90
Fig. 4.2 Illustration of proposed algorithm	92
Fig. 4.3 Segmented images for various GA parameters	93
Fig. 4.4 GA filtered output of an image with a single lesion	95

	Page No
Fig. 4.5 GA filtered output of an image without any lesion	95
Fig. 4.6 GA filtered and dilated output of image with a single lesion	96
Fig. 4.7 GA filtered and dilated output of image with no lesion	96
Fig. 4.8 Region growing output	97
Fig. 4.9 Segmentation of an image with two lesions	98
Fig. 4.10 Segmentation of an image with single lesion	98
Fig. 4.11 Segmentation of an image without any lesion	99
Fig. 4.12 Mask comparison at two stages of segmentation: 2 lesions	99
Fig. 4.13 Mask comparison at two stages of segmentation: no lesion	100
Fig. 4.14 (a) Comparison of Dice coefficient	106
Fig. 4.14 (b) Comparison of PSNR	106
Fig. 4.14 (c) Comparison of Hausdorff distance	107
Fig. 4.14 (d) Comparison of dice MSSD	107
Fig. 4.15 Original and ROI segmented mammograms : Different abnormalities	110
Fig. 4.16 Plot of performance measures	111
Fig. 5.1 Image compression model	115
Fig. 5.2 Encoder and decoder	116
Fig. 5.3 Single level decomposition in 2D DWT computation	122
Fig. 5.4 Two level decomposition in 2D DWT computation	123
Fig. 5.5 Flow chart for generalised compression/decompression algorithm	131
Fig. 5.6 Reconstruction of medical image using row wise decomposition	136
Fig. 5.7 Reconstruction of natural image using row wise decomposition	136
Fig. 5.8 Zoomed version of Fig. 5.6 by a factor of 2	137
Fig. 5.9 Zoomed version of Fig. 5.7 by a factor of 4	137
Fig. 5.10 Performance curves for algorithm using row wise decomposition	138
Fig. 5.11 Original and reconstructed images:Using column wise decomposition	139
Fig. 5.12 Comparison of variations of PSNR, NMSE with cr	140
Fig. 5.13 (a) Variation of PSNR with number of coefficients	140
Fig. 5.13 (b) Variation of NMSE with number of coefficients	141
Fig. 5.13 (c) Variation of compression ratio with number of coefficients	141
Fig. 5.14 Comparison of original and reconstructed image	143
Fig. 5.15 Comparison of zoomed versions of original and reconstructed image	143

	Page No
Fig. 5.16 Performance curves comparison	144
Fig. 5.17 Original images from ModelFest database	146
Fig. 5.18 Reconstructed images using row wise decomposition	146
Fig. 5.19 Original images from ModelFest database rotated by 90 degree	147
Fig. 5.20 Reconstructed images using column wise decomposition	148
Fig. 5.21 Performance parameters for CR images	150
Fig. 5.22 Performance parameters for CT images	151
Fig. 5.23 Performance parameters for MR images	152
Fig. 5.24 Performance parameters for US images	153
Fig. 5.25 Original and reconstructed image	154
Fig. 6.1 Two level wavelet decomposition with spatial orientation tree	160
Fig. 6.2 Block diagram of deflete algorithm	165
Fig. 6.3 Result of segmentation (lesion in lungs)	168
Fig. 6.4 Result of segmentation (lesion in liver)	169
Fig. 6.5 Original and decomposed images of slice 206 of MM2_10	171
Fig. 6.6 Plot of <i>cr</i> percentage vs level of decomposition of BG	172
Fig. 6.7 Plot of PSNR vs level of decomposition of BG	173
Fig. 6.8 Plot of MSSIM vs level of decomposition of BG	173
Fig. 6.9 Decompressed images of mdb245 compared with different <i>cr</i>	177
Fig. 6.10 Original and Decompressed versions of images used in with <i>cr</i>=19	179

List of Tables

	Page No
Table 3.1 Comparison of performance measures for different types of images	75
Table 3.2 Comparison of CII in different enhancement	77
Table 4.1 Effect of various λ on segmented area and MSSIM	94
Table 4.2 Performance measures for 2 stages of segmentation	101
Table 4.3 Comparison of number of lesions detected in segmented images	102
Table 4.4 Algorithm ranked acc. to Dice, PSNR, Hausdorff and MSSD	108
Table 4.5 Segmentation evaluation	111
Table 6.1 Performance measures with number of coefficients retained	170
Table 6.2 Comparison of performance measures: images with and without lesion	174
Table 6.3 Comparison of performance measures: various levels	176
Table 6.4 Comparison of performance measures: different cr	177
Table 6.5 Performance measures for compression	178

Abbreviations

BG	-	Background
CAD	-	Computer Aided Diagnosis
CII	-	Contrast Improvement Index
CR	-	Computed Radiography
CT	-	Computed Tomography
DWT	-	Discrete Wavelet Transform
EMEE	-	Enhancement Measure by Entropy
FDG	-	Fluoro- Deoxy Glucose
GA	-	Gabor Annulus
HVS	-	Human Visual System
LP	-	Linear Prediction
MRI	-	Magnetic Resonance Imaging
MSSD	-	Mean Sum of Square Distance
MSSIM		Mean Structural Similarity
NAE	-	Normalised Absolute Error
NMSE	-	Normalised Mean Square Error
PET	-	Positron Emission Tomography

PSNR	-	Peak Signal to Noise Ratio
ROI	-	Region of Interest
SNR	-	Signal-to-Noise Ratio
SPECT	-	Single Photon Emission Computed Tomography
SPIHT	-	Set Partitioning in Hierarchial Trees
SSIM	-	Structural Similarity Index
SUV	-	Standardised Uptake Value
SWT	-	Stationary Wavelet Transform
US	-	Ultrasound
WB	-	Whole Body
<i>cr</i>	-	Compression Ratio
1D DWT	-	One Dimensional DWT
2D DWT	-	Two Dimensional DWT

CHAPTER 1

INTRODUCTION

Molecular Imaging is a new discipline in medicine, which has evolved as the integration of three specific areas of specialization; namely cell biology, molecular biology and diagnostic imaging. This has evolved from the need to better understand the fundamental molecular pathways inside organisms in a non-invasive manner. More recently, the term ‘Molecular Imaging’ has been used for the non-invasive imaging of molecular, genetic and cellular processes in vivo. The clinical applications of molecular imaging include the use of nuclear medicine, magnetic resonance imaging (MRI) and ultrasound (US).

There are two basic applications for molecular imaging. The first is diagnostic imaging to determine the location and extent of targeted molecules specific to the disease being assessed. The second is applying therapy to specific disease targeted molecules. The basic principle of the diagnostic imaging application is derived from the ability of cell and molecular biologists to identify specific receptor sites associated with target molecules that characterize the disease process to be studied. The biology teams then develop molecular imaging agents, which will bind specifically to the target molecules of interest [1].

1.1 Molecular imaging

In the early twenty first century, the intersection of molecular biology and in vivo imaging emerged into a new discipline called

molecular imaging, which enabled the visualisation of the cellular function and the follow up of the molecular process in living organisms without perturbing them. The multiple and numerous potentialities of this field are applicable to the diagnosis of diseases such as cancer, and neurological and cardiovascular diseases.

Molecular imaging plays a pivotal role in guiding the management of cancer: diagnosing, staging - extent and location, assessing therapeutic targets, monitoring therapy and evaluating prognosis. It is playing an increasingly significant role in conditions such as tumours, dementias (Alzheimer's and others), movement disorders, seizure disorders and psychiatric disorders. It offers unique insights that allow a more personalized approach to evaluation and management of heart diseases.

The different categories of molecular imaging modalities are magnetic resonance imaging (MRI), optical imaging, nuclear medicine techniques, and ultrasound (US). They are construed in terse in the subsequent subsections.

1.1.1 Magnetic resonance imaging

MRI uses a powerful magnetic field to align the magnetization of some atoms in the body, and then uses radio frequency fields to systematically alter the alignment of this magnetization. This causes the nuclei to produce a rotating magnetic field detectable by the scanner and this information is recorded to construct an image of the scanned area of the body. MRI has the advantages of having very high spatial resolution and is very adept at morphological imaging and functional imaging [2]. While MRI provides very high resolution (up to 10 μm) and unlimited depth of penetration, it is, however, limited by low sensitivity, with detectabilities in the milli to micro molar (10^{-3} to 10^{-6}) range [2].

1.1.2 Optical imaging

Optical imaging uses the behaviour of visible, ultraviolet, and infrared light used in imaging. The imaging techniques include two major classes: fluorescence and bioluminescence imaging [2]. Fluorescence is the property of certain molecules to absorb light at a particular wavelength and to emit light of a longer wavelength after a brief interval known as the fluorescence lifetime. Bioluminescence is the process of light emission in living organisms. While the total amount of light emitted from bioluminescence is typically small and not detected by the human eye, an ultra sensitive CCD camera can image bioluminescence. The downside of optical imaging is the lack of penetration depth, especially when working at visible wavelengths.

1.1.3 Nuclear medicine techniques

Nuclear medicine techniques provide practically unlimited depth penetration and have very high sensitivities, in the nano molar (10^{-9}) range. Single photon emission computed tomography (SPECT) and positron emission tomography (PET) are two nuclear medicine techniques in imaging. SPECT uses γ -rays emitted from radioactive isotopes attached to pharmaceutical tracers that are specific to certain physiological, metabolic and pathological activities. The γ -rays which are emitted during radioactive decay pass out of the body and are collected by detectors (gamma cameras) placed around the patient. The detectors measure the distribution of the tracer within the body, and produce images which show the functional or metabolic activities of relevant organs.

In SPECT a rotating gamma camera, with one, two or three detector heads, rotates around. The main advantage of SPECT is absence of

superpositioning of overlying and underlying signals. Pseudo colour is often added to images to increase clarity [3]. PET works by injecting the patient with radioactive isotopes that emit particles called positrons. When a positron meets an electron, the collision produces a pair of gamma ray photons having the same energy but moving in opposite directions. From the position and delay between the photon pair receptor, the origin of the photons can be determined.

PET is a functional modality that can be used to visualize pathologies at much finer molecular level. This is achieved by employing radioisotopes that have different rates of intake for different tissues. The patient is surrounded by multiple rings of gamma photon detectors, so no detector rotation is required. In PET two γ -ray photons are produced at same time. PET images have higher SNR and better spatial resolution (~2 mm) when compared with SPECT but at the sacrifice of high price [3].

1.1.4 Ultrasound imaging

In ultrasound imaging, a sound wave is typically produced by a piezoelectric transducer encased in housing. Strong, short electrical pulses from the ultrasound machine make the transducer ring at the desired frequency. The frequencies can be anywhere between 2 and 18 MHz. The sound is focused to produce an arc shaped sound wave from the face of the transducer. The wave travels into the body and comes into focus at a desired depth. The sound wave is partially reflected from the layers between different tissues. Some of the reflections return to the transducer. The return sound wave vibrates the transducer and turns the vibrations into electrical pulses that travel to the ultrasonic scanner where they are processed and transformed into a digital image [2].

1.2 Medical images and processing

Medical imaging systems, take input signals which arise from various properties of the body of a patient, such as its attenuation of x-rays or reflection of ultrasound. The resulting images can be continuous (analog) or discrete (digital); the former can be converted into the latter by digitization. The challenge is to obtain an output image that is an accurate representation of the input signal, and then to analyze it and extract as much diagnostic information from the image as possible.

An imaging system senses or responds to an input signal, such as reflected or transmitted electromagnetic radiation from an object, and produces an output signal or image. The sensor array, placed at the focal plane, produces outputs proportional to the integral of the radiation received at each sensor during the exposure time, and these values become the terms in a two dimensional matrix, which represents the scene called a sampled image. The physical disposition of sensors facilitates the collection of data into an array, but the values themselves are still integrals and hence continuous; they need to be quantized to a discrete scale before the image is a digital image. Digital images can be represented by an array of discrete values, which makes them amenable to storage and manipulation within a computer [3].

Imaging systems can be classified as direct and indirect systems. The direct imaging acquires data as recognizable image, whereas indirect imaging requires data processing or reconstruction steps before the image is available for observation. Direct imaging can be subdivided further, depending on whether the image is acquired as a whole, parallel acquisition, or in parts, serial acquisition. The optical microscope or scintillation

camera can be considered as examples for serial acquisition direct imaging system while scanning microdensitometer is an example of parallel acquisition direct imaging. X-ray, PET,CT etc. are the examples of indirect imaging systems [4].

Imaging systems can possess health hazards if proper care and precautions are not administered. The main hazards of medical imaging are exposure to ionising radiation, anaphylactoid reactions i.e., life threatening allergic conditions due to iodinated contrast media, contrast induced nephropathy i.e., kidney related problems and MRI safety issues. For the safety of patients all the imaging systems follow ALARA (As Low As is Reasonably Achievable) principle [5].

From the general imaging system let us move to specific imaging systems used in the work under consideration. In this work the input used is PET images. An extension/ modification of the work is carried out on computed radiographic images viz., mammographic images also.

1.2.1 PET imaging

PET imaging is the injection (or inhalation) of a substance containing a positron emitter (radio nuclide), the subsequent detection of the emitted radiation by a scanner, and the computation of a digital image that represents the distribution of the radiotracer in the body. A radio-nuclide is a nonstable specific combination of protons and neutrons that make up a nucleus, which will eventually decay. Many radio-nuclides emit a positron upon decaying. The positron is a subatomic particle identical to the electron but opposite in charge. Even though many radio-nuclides decay via positron emission, only a few have been used much for PET imaging. The most commonly used are: C-11, N-13, O-15, F-18, Rb-82 [6].

1.2.1.1 Physics behind PET

Positron annihilates nearby electron when it loses its kinetic energy after travelling a short distance in the tissue. Annihilation results in the production of two photons which move in opposite directions from each other, and having 511 keV energy. The photons are directed towards the depicted ring of detectors. The detectors consist of a scintillator, which converts energy from the 511 keV photon into many lower energy light photons, and a photomultiplier, which converts the light into an electronic pulse. The creation of two electronic pulses at the same time indicates that there was an annihilation somewhere in the column or line of response (LOR) connecting the associated detectors. During the scan, coincidence counts are recorded for each LOR. The number of coincidence counts obtained on a particular LOR indicates the amount of radioactivity present along that line during the scan. A parallel set of LORs then measures a projection of the radioactivity distribution [6].

1.2.1.2 Image reconstruction

The raw data from PET detector ring is stored and displayed in a sinogram. The lines of response are sorted into parallel subsets and each subset represents a projection angle. Each angle is represented by a row in an image. The image reconstruction starts with raw data (sinograms) and produces cross sectional images that represent that radioactivity distribution. The two popular algorithms for reconstructing PET images are filtered back projection (FBP), and ordered subsets expectation maximization (OSEM) and results are shown in Fig 1.1

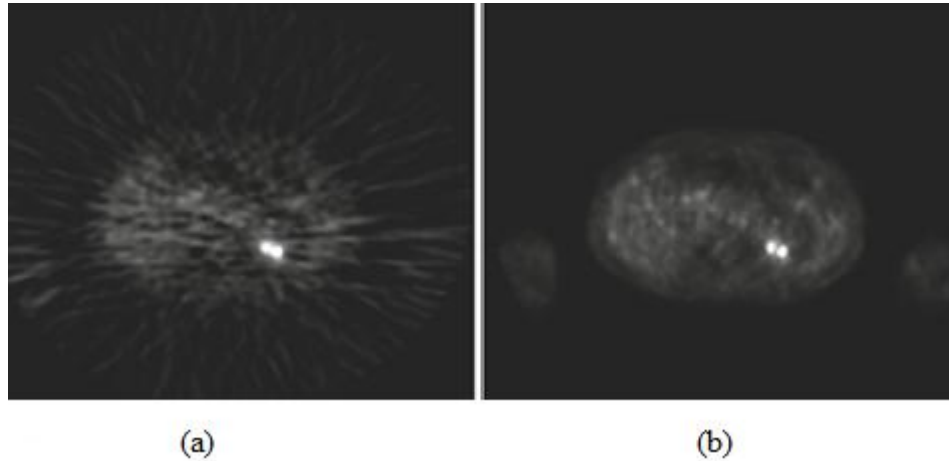


Fig. 1.1 Images reconstructed from the same raw data a) reconstructed with filtered back projection (FBP) b) ordered subsets expectation maximization (OSEM)

The images that result from PET provide quantitative information. After corrections and image reconstruction, each image is a pixel by pixel representation of the radiotracer concentration at scan time. The scan protocols can be performed to provide more physiologically meaningful quantitation, such as glucose metabolic rate, or blood flow. The knowledge about the radiotracer concentration in arterial blood that is finely sampled, is required for this physiological quantitation. The acquisition of dynamic data is also required because the repeated scans starting at injection time show the time course of radiotracer in the tissue of interest [6].

1.2.1.3 Background events

Background events in PET imaging include the scattered event and the random event which are detrimental to the quality of the resulting images. In a scattered event, one or both of the photons scatter in body tissue, changing direction and losing energy, but it is still detected. In general, scattered events will have in-plane and out-of-plane components. To limit the number of events with substantial out-of-plane components,

shielding called septa is used in front of and behind the detector ring. The septa in addition to reducing the number of scattered events, also minimises the number of events lost to detector dead time and number of random events.

A random event is depicted in Fig 1.2. The two photons measured are from different annihilations. It is possible to measure four photons simultaneously from simultaneous annihilations but, the probability of all four photons leaving the body unscattered is quite small.

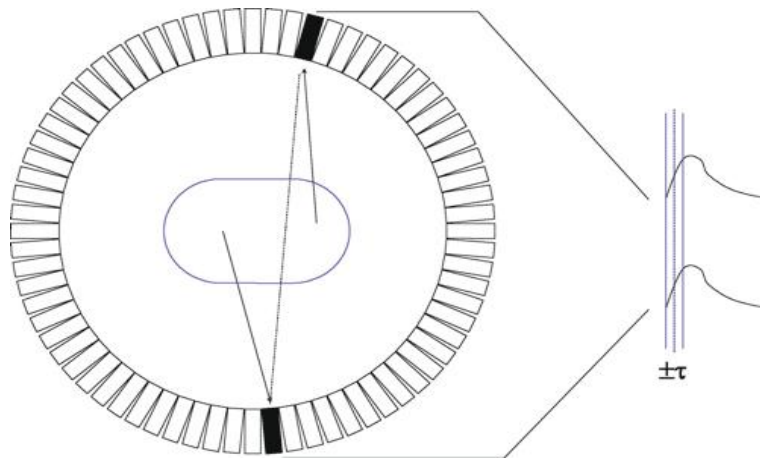


Fig. 1.2 A random background event. Annihilation photons from two independent decays are emitted and detected at approximately the same time

The rate at which random coincidences will be measured between detectors A and B is given by

$$R_R = 2\tau R_A R_B \quad (1.1)$$

where R_A and R_B are the rates at which detectors A and B are detecting photons, respectively, and 2τ is the size of the timing window. This timing window is analogous to the energy window used to discriminate between

scattered and nonscattered photons. The window should be large enough to allow true events to be accepted, at the same time small enough to exclude as many random events as possible.

Counts measured during a PET scan include true, scattered, and random events. The term prompt is given for any intime coincidence. It is given by the equation given below:

$$P = T + S + R \quad (1.2)$$

where P , T , S , and R , are the prompt, true, scattered, and random events, respectively. We desire to reconstruct images only with T events. We require an estimate of true events T' , which is obtained as follows:

$$T' = P - S' - R' \quad (1.3)$$

where S' and R' are estimates of the number of scattered events and random events.

The noise equivalent count (NEC) parameter provides an estimate of image signal to noise ratio as a function of T , S , and R . A simplified equation to find NEC is given below;

$$NEC = \frac{T}{(1 + \frac{S}{T} + \frac{R}{T})} \quad (1.4)$$

This could refer to the statistical quality of data on a specific line of response, or the image quality resulting from all lines of response [6].

1.2.1.4 Spatial resolution

The spatial resolution of PET images is determined by factors viz. positron range, photon non-collinearity and size of detector. The effects contributed by positron range and photon non-collinearity are relatively

small. Size of the detector can be controlled so as to improve spatial resolution. Smaller detectors give better resolution.

The main problem with the miniaturisation of PET detectors crystals is that it is not feasible to couple each crystal to its own photo multiplier if crystals are small and numerous. This problem is solved by coupling a matrix of crystals to a small number of photo multiplier tubes. The relative pulse heights from the photo multiplier signals are used to determine which crystal in the matrix was actually hit. This scheme leads to a large reduction in the required number of photo multipliers [6].

1.2.1.5 Attenuation correction

Attenuation is the loss of coincidence events through scatter or absorption of one or both of the annihilation photons in the body. While the photon energy is higher in PET than that of any single photon emission radio-nuclide and the linear attenuation coefficient is relatively low, the requirement of detecting both photons yields a higher overall event per event attenuation probability. For objects of the size of a head, approximately 25% of photon pairs survive. For a small abdomen, approximately 10% survive. For a very large abdomen, the number surviving can be 1% or smaller.

The image quality is degraded because of the decreased counts obtained from large body regions. This effect cannot be corrected, but can only be offset by using a higher injected dose or a longer scan time. Another implication of attenuation is the loss of quantitation in the measurement of radioactivity concentration and other quantities derived from it. An additional factor with attenuation is the introduction of image

artifacts, that is, features that make the image qualitatively unrepresentative of the actual radioactivity distribution.

Attenuation correction takes into account the attenuation factor for each line of response. The probability that photons emitted along each line of response will survive is the attenuation factor. The reciprocal of this factor, the attenuation correction factor, can be applied for each line of response, resulting in an estimate of the number of counts that would have been attained on each LOR. Attenuation correction can be obtained with a transmission scan. A conventional scheme for PET transmission scanning uses one or more Ge-68 rods that orbit around the body, inside the detector ring for 1–5 min per bed position. Attenuation factors for each line of response are determined by dividing the counts obtained during a transmission scan by the counts obtained during a blank scan, which is a transmission scan performed with an empty gantry. A third option for attenuation correction is to use x-ray CT as the transmission data. Much short scans provide much lower noise corrections [6].

1.2.1.6 PET Quantitation

Quantitative use of PET data requires accurate corrections for attenuation, scatter, random events, and dead time. The first step in quantitation is producing images whose pixel values represent the radioactivity concentration of the imaged object. Calibration factors are also needed to translate the corrected counts to radioactivity values.

Standardised uptake value (SUV) is an index that normalizes for the injected dose and body size in a simple way. The SUV is calculated as

$$SUV = \frac{\text{Radioactivity Concentration}}{\text{Injected Dose/Body Mass}} \quad (1.5)$$

SUV can also be interpreted as the concentration of tracer measured in a region, divided by the average concentration throughout the body. Individual pixels can be calculated as SUV values, and regions of interest statistics (typically maximum and mean) can be reported in SUV [6].

The perception gained about PET imaging basics helps to have a better understanding of the images in the database under deliberation. Simulated PET data are widely used in the development and validation studies of PET image acquisition and processing methods. The synthetic data should resemble the original data as close as possible in case of statistical properties, contrast, bias, and artifacts. The simulated database ONCOPET_DB [7] is one such database which is used for the validation of this work.

1.2.1.7 ONCOPET_DB database

ONCOPET_DB has whole body (WB) PET images which should represent the complex activity distributions. The ^{18}F -FDG (Fluoro Deoxy Glucose) activity distribution of simulated database was derived from 70 PET exams (43 men's exams and 27 women's exams) acquired with an ECAT EXACT HR+ (CTI/Siemens, Knoxville) scanner, fully corrected and reconstructed with the attenuation-weighted ordered subsets expectation maximization (AW-OSEM) algorithm using six iterations, 16 subsets, and a Gaussian isotropic post filtering of 8 mm full width at half maximum (FWHM).

The ONCOPET_DB database is composed of 100 WB PET simulated images, including 50 normal cases coming from different realizations of noise of the healthy model and 50 pathological cases including lesions of calibrated uptakes and various diameters. The phantom

used for generation of database was generated from the segmentation of two CT scans of the head and torso of a standard adult male having height 175 cm and weight 70.3 kg. This resulted in a 192 x 96 x 243 voxelized phantom with isotropic voxels of 3.57 x 3.57 x 3.57 mm³. The simulated image volumes are 128 x 128 x 375 with voxel dimension of 5.0625 x 5.0625 x 2.4250 mm³.

A model of lesion extent based on the clinical description of lymphoma patients is used. Lymphoma affects the lymphatic system through the lymph nodes and other organs implied in the immune system. It mostly affects young adults and is particularly reactive to conventional treatments, such as chemotherapy or radiotherapy. PET is used for the crucial part of staging and treatment follow up of lymphoma, due to a higher sensitivity and specificity than anatomical medical imaging modalities. Lymphoma is characterized by small lesions that are mainly localized in the lymph nodes and can also extend in other organs such as the liver, the spleen, and the lungs. Despite high detection performances of oncologists, difficult cases of hardly visible residual lesions, particularly during the therapeutic follow up, remain a diagnostic challenge.

The adult human body contains at least 700 lymph nodes with a diameter of about 6 mm, which makes their anatomical localization hard to describe. In the phantom used lymph nodes in the thoracic and mediastinal areas are located in a structure corresponding to the blood pool. Lesions were approximated by spheres of 7, 10.5, and 14 mm diameter. Lesions were not allowed to stand closer than four pixels (approximately 14 mm) to the organ edges, except in the blood pool. In addition, overlapping lesions were forbidden to avoid clusters' generation. The attenuation coefficient of the lesions is that of water. The mediastinal (above the diaphragm) and lumbar (below the diaphragm) forms represent 50% and 10%, respectively

and last 40% of cases correspond to the spread of diffuse lesions in the whole upper torso. The main targeted organs are the lungs and the blood pool for the mediastinal form and the liver, the spleen, and the blood pool for the lumbar form.

The lesions are localized for 80% of the cases in lymph nodes and 20% in the other organs. The total number of lesions per image was set to five for first set of 25 images and for a second set of 25 images we have ten lesions per image. The distributions of lesions are in the same organs with a probability of 30% each for the lungs, the liver, and the blood pool, respectively, and 10% for the spleen. For first series of pathological images, a total of 125 spherical lesions—105 in the lymph nodes, 4 in the liver, 15 in the lungs, and 1 in the spleen are present. The second series has a total of 250 spherical lesions—75 in the lymph nodes, 75 in the liver, 75 in the lungs and 25 in the spleen [7].

This database was primarily designed for the PET image processing community to be used for the evaluation of various algorithms that may impact contrast recovery of small structures due to partial volume effect, reconstruction and quantification, as well as detection studies or image processing methods.

1.2.2 X-ray mammography

X-ray imaging has been used in clinical diagnosis since the discovery of x-rays. X-rays are generated in an evacuated x-ray tube, which consists of a cathode and an anode. Heating a tungsten filament within the cathode releases electrons by thermal excitation. Increasingly negative voltages applied to the cathode cup focus the electrons into a narrow beam or even switch off the beam entirely [8]. The electrons are accelerated

towards the positive (50–120 kV) anode, where they strike an embedded tungsten target, producing x-rays.

X-rays interact with the body either by photoelectric absorption or scattering. In photoelectric absorption the x-ray photon is absorbed liberating an electron from the inner shell of an atom, while in scattering, only part of the x-ray photon energy is used to liberate an electron from an outer shell and the photon changes direction. The photoelectric absorption contributes to radiation dose and consequently to the risk of biological damage to the patient. The scattering results in a loss of image quality. As a result of these interactions the intensity of the beam is reduced. The beam intensity is proportional to the number of X-ray photons in it. Different tissues affect the beam by differing amounts, depending on their thickness (t) and the attenuation coefficient (μ) of the material.

As on present day, computer radiography is popular. Computer radiography uses an imaging plate which comprises of a screen coated with a storage phosphor. When the imaging plate is exposed to x-rays, electrons absorbed by the phosphor are excited to higher energy levels and are trapped there, resulting in a latent (or hidden) image. The latent image in the imaging plate is read by scanning the plate in a raster pattern with a well focused laser beam. The laser light stimulates the release of the trapped electrons, accompanied by the release of blue light, which is converted to a voltage by a photomultiplier; the voltage signal is digitized and stored in a computer.

X-ray mammography is one of the most challenging areas in medical imaging field. It is used to distinguish subtle differences in tissue type and detect very small objects, while minimizing the absorbed dose to the breast. Since the various tissues comprising the breast are radiologically

similar, the dynamic range of mammograms is low. Special x-ray tubes capable of operating at low tube voltages (25–30 kV) are used, because the attenuation of x-rays by matter is greater and predominantly by photoelectric absorption at small x-ray energies, resulting in a larger difference in attenuation between similar soft tissues and, therefore, better subject contrast. However, the choice of x-ray energy is a compromise: too low an energy results in insufficient penetration with more of the photons being absorbed in the breast, resulting in a higher dose to the patient. Most modern x-ray units use molybdenum targets, instead of the usual tungsten targets, to obtain an x-ray output with the majority of photons in the 15–20 keV range.

Currently, most mammograms are visually examined by humans in search of subtle and complicated indicators of breast cancer. Reading mammograms can be a tedious and time consuming task. A computer assisted diagnosis software is able to highlight suspicious areas in digital mammograms automatically for checking by a human expert [3].

The knowledge acquired from basics of X-ray mammography helps in having a better perception of images considered in this work for validation. The mammographic database mini-MIAS [9] contemplated here is explained in next section.

1.2.2.1 Mini-MIAS database

The mini-MIAS mammographic database by J Suckling contain normal images and images having different abnormalities. The breast abnormalities that can indicate breast cancer are masses, calcifications, architectural distortion and bilateral asymmetry. Breast Imaging-Reporting

and Data System (BI-RADS), a quality assurance tool has defined the above said breast abnormalities.

According to BI-RADS, a mass is defined as a space occupying lesion seen in at least two different projections. If a potential mass is seen in only a single projection it is called 'asymmetry' or 'asymmetric density' until its three dimensionality is confirmed. Masses have different density (fat containing masses, low density, isodense, high density), different margins (circumscribed, micro-lobular, obscured, indistinct, spiculated) and different shape (round, oval, lobular, irregular). Round and oval shaped masses with smooth and circumscribed margins usually indicate benign changes. On the other hand, a malignant mass usually has a spiculated, rough and blurry boundary.

Calcifications are deposits of calcium in breast tissue. Benign calcifications are usually larger and coarser with round and smooth contours. Malignant calcifications tend to be numerous, clustered, small, varying in size and shape, angular, irregularly shaped and branching in orientation.

Architectural distortion is defined as distortion of the normal architecture with no definite mass visible, including spiculations radiating from a point and focal retraction or distortion at the edge of the parenchyma. Architectural distortion of breast tissue can indicate malignant changes especially when integrated with visible lesions such as mass, asymmetry or calcifications. Architectural distortion can be classified as benign when including scar and soft tissue damage due to trauma.

Asymmetry of breast parenchyma between the two sides is a useful sign for detecting primary breast cancer. Bilateral asymmetries of concern

are those that are changing or enlarging or new, those that are palpable and those that are associated with other findings, such as microcalcifications or architectural distortion. If a palpable thickening or mass corresponds to an asymmetric density, the density is regarded with a greater degree of suspicion for malignancy.

The mini-MIAS database contains 322 images in PGM format having various abnormality features as well as normal ones. The size of individual images in the database is 1024x1024 pixels. It also includes radiologist's 'truth' markings on the locations of any abnormalities that may be present.

The abnormalities present in the images in the database are classified into microcalcifications, circumscribed masses, architectural distortion, spiculated masses and miscellaneous categories. The breast density and severity of abnormality are also specified.

1.2.3 Image processing techniques

The rapid, continuous momentum in computerised medical image visualisation, advances in analysis methods and computer aided diagnosis caused the development of medical image processing into one of the most important fields within scientific imaging. The main challenge in this field is to process and analyze the images in order to effectively extract, quantify, and interpret the information to gain understanding and insight into the structure and function of the organs being imaged. The general goal is to understand the information and put it to practical use.

Some of the main challenges in medical image processing are image enhancement and restoration, automated and accurate segmentation of

features of interest, automated and accurate registration and fusion of multi-modality images, classification of image features, namely characterization and typing of structures, quantitative measurement of image features and an interpretation of the measurements and development of integrated systems for the clinical sector.

Imaging science has expanded its lines of investigation as segmentation, registration and visualization. Segmentation brings out the ability to accurately recognise and delineate all the individual objects in an image scene. Registration involves finding the transformation that brings different images of the same object into strict spatial (and/or temporal) congruence. Visualisation involves the display, manipulation, and measurement of image data. Another area involved in imaging science is compression. Image compression deals with reducing the size of the image so that its storage and transmission become less taxing in terms of space and bandwidth needed. Compression is possible because images tend to contain redundant or repetitive information.

The major strength in the application of computers to medical imaging lies in the use of image processing techniques for quantitative analysis. Medical images are primarily visual in nature and limited by inter observer variations and errors due to fatigue, distractions, and limited experience. The interpretation of an image by an expert depends on the experience and expertise in the field and this is subjective. Computer analysis done with appropriate care and logic, can potentially add objective strength to the interpretation of the expert. Thus we can improve the diagnostic accuracy and confidence of even an expert with many years of experience.

The basic medical image processing are grouped, broadly, into five fundamental classes: image enhancement, restoration, analysis, compression and synthesis. Image enhancement helps an image to either look better to an observer, a subjective phenomenon, or to perform better in a subsequent processing class. Enhancement involves adjusting the brightness of the image, or its contrast and smoothing an image that contains a lot of noise or speckle. The sharpening of an image makes the edges within it more clearly visible. This is another image enhancement technique.

Images are often significantly degraded in the imaging system, and image restoration is used to reverse this degradation. This would include reversing the effects of: uneven illumination, non linear detectors which produce an output (response) that is not proportional to the input (stimulus), distortion, caused by poorly focusing lenses or electron optics. Image analysis involves taking measurements of objects within an image, preferably automatically, and assigning them to groups or classes. Image segmentation involves isolation of the objects of interest from the rest of the image, measurement of features such as size, shape and texture. This allows classification of the objects within an image, preferably automatically, and assigning them to groups or classes [4].

Image synthesis creates new images from other images or non image data. The reconstruction of axial tomographic images from projection data as in computed tomography is an example of image synthesis.

Image compression reduces the amount of data needed to describe the image. Compression reduces the file size so that the image can be more

efficiently stored or transported electronically, in a shorter time. Alternative storage schemes can store the information more effectively, i.e. in smaller files, and decompression algorithms can be used to retrieve the original image data.

1.3 Need for compression

In a developing nation like ours, the emergence of telemedicine is a boon. Currently, medical applications have been integrated with mobile devices and are being used by medical personnel in treatment centres for retrieving and examining patient data especially, medical images. Mobile telemedicine with applications in emergency health care, teleradiology, telecardiology, telepathology, teledermatology and teleoncology have become popular to provide prompt and efficient patient care. The rural and remotely located people can be provided same level of diagnosis by experts as city dwellers. In the telemedicine field, for easy transmission of medical images it is advisable for the images to have reduced sizes. This necessity direct us to the area of compression in field of medical images. Compressing a medical image is a challenging task as we can not afford to lose vital data needed for correct diagnosis.

The two components in image which can be adjusted to receive compression are redundancy and irrelevancy. Redundancy reduction removes duplication while irrelevancy reduction omits parts of signals that will not be noticed. The different types of redundancies are spatial, temporal and spectral. The main techniques are lossless, lossy compression, predictive coding and transform coding.

The main elements of an image compression system are source encoder, quantiser and entropy encoder. Source Encoder performs

transform coding. Quantiser reduces the number of bits needed to store transformed coefficients. Entropy Encoder uses Huffman coding, Arithmetic coding or Run Length Encoding. All these elements reduce redundancy and irrelevancy.

Lossy compression is more efficient in terms of storage and transmission needs but there is no guarantee to preserve the characteristics needed in medical diagnosis. To avoid the above risks, there is another option that the diagnostically important region, i.e., region of interest (ROI) of the image is lossless compressed and the remaining part of the image, i.e., background (BG) is lossy compressed with high compression ratio(cr), as a consequence both the requirements are satisfied in one go i.e. preserving the useful information and the high cr [10].

1.4 Motivation

It is advisable to have a centralized database for medical images for quick reference to obtain a correct diagnostic. In the case of MRI images, PET images etc. the comparison of images having pathology with healthy ones, and comparison of images prior to and post the start of treatment may be beneficial. But in today's scenario, images are not stored for longer time due to storage constraints. If compression of images can be done without the loss of important details, it will help in this context.

In case of teleconsultations, patient may have to wait in imaging apparatus till the remotely located diagnosing radiologist gets a good image from which he can deduce. In this case if compression of image without losing quality can be achieved, convenience and comfort of patient can be improved. Imaging apparatus can be utilized better and storage cost can be reduced. The reduction in transmission time helps the patient to get a quick

medication. Better bandwidth utilisation in the case of image transmission can also be achieved.

1.5 Objective of the work

About ten years back, a hospital on the average needed 1-2 TB for storing medical images and it increased to about 50-100 TB in next five years. The annual storage requirement increases at the rate of 20%-100%. In many of the hospitals the images are not stored for longer time due to storage constraints. Small size of the image is advantageous in case of medical image transmission in terms of bandwidth conservation. Even though emerging technologies offer many new methods for reducing image size and better bandwidth conservation, the increase in the number of images always outperform image compression techniques.

The purpose of medical image compression is to express image with less data to save storage space and transmission time, based on the premise that true information in original image will be preserved. The cost of transmission of images can be reduced and bandwidth utilisation can be made more efficient. The demand for medical image transmission indicates that there is always room for better and novel methods in image compression.

Even though lossless compression provides efficiency in terms of storage and transmission needs, the diagnostic quality of the image may be compromised in some cases. In diagnostically lossless compression, it is of immense importance that the image quality should be maintained and tests should be conducted to ensure that a reconstructed image has not lost diagnostically relevant information. Therefore, the medical image compression is really a challenging area and has good scope for the future

trends at the same time it can meet out the current requirements of telemedicine, teleconsultation, e-health and teleradiology [10].

Among the medical images, molecular images can give functional imaging rather than anatomical details. But the resolution of such images is less and compression of such images possesses a challenge, that loss of any diagnostic detail is not affordable.

The main objective of this work is to develop a novel and efficient ROI based scheme for image compression for molecular images that preserves the true diagnostic information, at the same time reduce storage and transmission costs. The additional objectives are to develop a method to detect ROI that suits the type of molecular image under consideration and to investigate the use of developed method in the field of e-health and teleradiology. The work also aims to extend the techniques developed for compression to other biomedical imaging modalities.

1.6 Layout of the Thesis

The thesis is systematised in the subsequently explained manner in 7 chapters. In the first chapter molecular imaging, medical image processing techniques, and databases used are explained. The motivation and objective of the work are also discussed in the introduction chapter.

The work done in this research can be partitioned as enhancement, segmentation and compression. The literature review on the three modules are represented in Chapter 2. The literature survey is done separately for PET images and mammographic images in case of enhancement and segmentation. The state of the art in medical image compression going through ROI, PET images and mammograms are also discussed here.

The newly developed preprocessing technique is discussed in Chapter 3. The background of the enhancement technique like stationary wavelet transform and unsharp masking are examined here. The measures used to quantify enhancement and the general medical image enhancement methods are also discussed in this chapter

Chapter 4 furnishes the chronicles of the ROI segmentation techniques devised. The theory of gabor annulus filtering and region growing are discussed in this chapter. The widely used medical segmentation techniques and quantification of image segmentation are the other topics examined here.

The compression techniques newly envisaged are elucidated in Chapter 5. The basics of compression and performance measures are also delineated in this chapter. The philosophy behind the developed technique; wavelets and linear prediction are also analysed in this chapter.

Integrating the different modules of the work together is a work in itself. Chapter 6 is dedicated towards that cause and the results and inferences are discussed here.

Chapter 7 is the concluding chapter, wherein the observations and deductions already brought out in the previous chapters are summarized. The suggestions for further work are also given in this chapter.

CHAPTER 2

LITERATURE REVIEW

2.1 Introduction

Literature survey is an essential step in research process. It helps the researcher to have broadened knowledge about the area under study, bring clarity and focus to the research problem and derive own methodology. In this chapter we deal with the literature survey conducted in connection with the research work done. The work can be mainly divided into three modules: image enhancement, image segmentation for ROI extraction and image compression to be applied on ROI and the BG. The literature survey on all the three modules are conducted separately.

Image enhancement process an image so as to make it more suitable than the original image for a particular application. The main purpose of image segmentation is to divide an image into regions which are meaningful for a particular task. Compressing an image is reducing its size without degrading image quality.

The first section gives a survey on image enhancement on PET images and mammographic images while the second section of the chapter deals with the trends in the segmentation of PET and mammographic images. The last section discusses about different image compression techniques and ROI based compression.

2.2 State of art on image enhancement

Image enhancement processes consist of a collection of techniques that seek to improve the visual appearance of an image or to convert the image to a form better suited for analysis by a human or a machine. It accentuates or sharpens image features such as edges, boundaries, or contrast to make a graphic display more useful for analysis. Image enhancement includes techniques such as contrast and intensity manipulation, noise reduction, background removal, edges sharpening and filtering.

2.2.1 Image enhancement in PET imaging

PET is a nuclear medicine medical imaging technique that produces a three dimensional image of functional processes in the body [11]. The basic principle of PET is based on the detection of photons emitted from the patient after the injection of a short lived radio-pharmaceutical like FDG. These photons are detected by the PET scanner and allow the reconstruction of a three dimensional image [12]. In PET imaging, the patient is injected with radioactive isotopes that emit particles called positrons. When a positron meets an electron, the collision produces a pair of gamma ray photons having the same energy but moving in opposite directions. From the position and delay between the photon pair receptor, the origin of the photons can be determined. The patient is surrounded by multiple rings of gamma photon detectors, so no detector rotation is required. PET images have spatial resolution of about 2 mm [3]. PET can be used to quantitatively measure physiological parameters, such as blood flow, or glucose metabolic rate [6].

The advantages of PET are clear localisation of regions of metabolism in brain and heart, identification and sizing of heart infarcts and quantitative permeability for brain tissue. PET imaging allows the evaluation of a drug by identifying and measuring regional metabolic changes as a result of drug therapy. PET is also highly sensitive to early signs of any disease. In PET images, exact location and extent of the lesion are measured by detecting early biochemical changes and checking whether the targeted tissue is metabolically active. The doctor can assess the biochemical process underlying the abnormality of an organ accurately with interpretation of good quality PET images [12].

The downside of PET is its relatively low spatial resolution, as a result of which its role in detecting direct invasion to adjacent structures such as stomach or duodenum or encasement of blood vessels become limited. Another short coming of PET imaging is the blurring nature of PET images and the high noise to signal ratio. The blurriness and the low spatial resolution in PET images, leads to a need for an enhancement technique that is capable on enhancing the quality of PET images without altering its dominant features [13].

Davis and Abidi [12] developed a method for modelling the noise in PET images and the noise was filtered utilising the spectral characteristics and mapping to polar coordinates which resulted in the enhancement of images. The developed technique considers PET signal characteristics, data collection and data reconstruction. The enhancement obtained had been evaluated by visual inspection and quantitative measurement are not done. The image database used in this is not a publicly available one.

Another method developed for edge enhancement in PET images was implemented by higher order derivative systems that emphasised the details in PET images. A private database consisting of PET images of brain was used. The higher order derivative filters were compared against Sobel filter for edge detection and found to have given satisfactory results regarding the generation of continuous edges and clear details. Visual inspection had been the measure of performance under study [13].

A 3 Dimensional (3D) wavelet based image processing tool, a wavelet filter was suggested for denoising and enhancement of dynamic PET image data in [14]. The filter based on multi scale thresholding and cross-scale regularization was used. Brain images from a private database had been utilised for the study and the correlation between processed and unprocessed values of total volume and binding potential were used to quantitatively express enhancement.

The enhancement by reconstruction of PET data by using expectation maximization had been discussed in [15]. The Shepp-Logan phantom image was used as input in the method. The enhancement was implemented in the image reconstruction phase and visual comparison with reconstructed image using filtered back projection (FBP) algorithm is used for evaluation and the former is found to be better .

The RGB image was changed to XYZ and YUV colour space to ensure a better quality PET image with minimal data loss [16]. Structural similarity index (SSIM) and visual information fidelity (VIF) were compared for edge detected versions of original and enhanced images. The images from Mayo Clinic had been used for the study and brain is the imaged body part. The XYZ model had better SSIM and VIF values of 0.7245 and 0.4575 respectively.

A technique was proposed by Yavirabdi, Samir and Bartoli [17] based on the interpolation of subband images derived using DWT which worked well with both 2D and 3D images, enhanced the image details and preserved the edges. Visual comparison and peak signal to noise ratio (PSNR) were used as performance measures. The average PSNR value of about 27dB was obtained for 2D slices.

Jin *et al.*, [18] enhanced PET images by denoising using a 3D wavelet expansion and thresholding with cross-scale regularization. A private database of brain PET images and liver SPECT images were used for the study in this case. Wavelet thresholding was compared with brushlet denoising and suggested the fusion of the two methods. Here also visual inspection was the performance measure used for evaluation.

Greechi *et al.*, [19] integrated anatomical information from CT to enhance PET images and hence produce a better PET/CT fusion. A private database and NEMA IEC body phantom without lungs was used as input database. The enhancement was evaluated by visual inspection and to effect the enhancement CT images were required.

2.2.2 Image enhancement in mammograms

The usual task of mammogram enhancement is to increase the contrast between ROI and BG and to sharpen the edges or borders of regions of interest [20]. However, some image enhancement techniques may distort diagnostic features, appearance and shape, leading to wrong diagnosis [21]. The main problem is the under enhancement of some regions and the over enhancement of others. Under enhancement can cause false negatives, while over enhancement can cause false positives [20].

The methods used to manipulate mammogram images can be categorized into four main categories; the conventional enhancement techniques, the region based enhancement techniques, the feature based enhancement techniques, and the fuzzy enhancement techniques. Conventional enhancing techniques are fixed neighbourhood techniques that modify images based on global properties. Region based methods for enhancing the contrast of mammogram features are based on the surroundings i.e., local properties. The feature based enhancement methods are those methods that utilise wavelet domain enhancement while the fuzzy enhancement techniques are methods that apply fuzzy operators and properties to enhance mammogram features [22].

The histogram equalization technique associated with watershed algorithm was tried out by Schiabel, Santos and Angelo [23] to have enhancement before segmentation. The segmentation technique results were used to evaluate the enhancement method. A sensitivity of 92% was obtained for 252 regions extracted from 132 mammograms.

Sampat and Bovik [24] proposed filtering and thresholding of radon transform of the image to enhance the spiculations in mammograms so as to assist in a spiculated mass detection technique of image. The algorithm was tested on the Digital Database for Screening Mammography (DDSM). The algorithm was modified for architectural distortion. Visual inspection was used as evaluation parameter for assessing the algorithm in this case.

Dabour [25] proposed an algorithm based on wavelet based level dependent thresholding and mathematical morphology for digital mammogram enhancement. Contrast improvement index (CII) is used for comparing the method with other methods like VisuShrink and BayesShrink. The proposed method was found to be superior to others.

Mohanalin, Kalra and Kumar [26] presented fuzzy algorithm based on Normalized Tsallis entropy to enhance the contrast of microcalcifications in mammograms. This was done in two phases, where in phase I the image had been fuzzified using Gaussian membership function while in phase II, using the non uniformity factor calculated from local information, the contrasts of microcalcifications were enhanced while suppressing the background heavily. The proposed approach improved the detection with the detection of microcalcifications from meager 80.21% true positives with 8.1 false positives to 96.25% true positives with 0.803 false positives.

Jiang, Yao and Wason [27] enhanced microcalcifications in digital mammograms by using the combined approach of fuzzy logic and structure tensors. The structure tensor operator and fuzzy enhancement operator were arranged in parallel to process the input digital mammograms. While the structure tensor operator processed the digital mammograms and produced a corresponding eigen image to highlight the ROIs, the fuzzy enhancement operator fuzzified the mammogram via the maximum fuzzy entropy principle in fuzzy domain. The proposed algorithm outperformed the existing benchmark in terms of cost figures across the whole range of true positive fractions.

Yu and Bajaj [28] described a fast approach based on localized contrast manipulation to enhance image contrast. This method was based on fast computation of local minimum, maximum, and average maps using a propagation scheme. The method had been tested on medical images including brain MR images, chest CT images and mammography images. The results were evaluated by visual inspection.

Sivaramakrishna *et al.*, [29] compared the performance of several contrast enhancement algorithms: adaptive unsharp masking, contrast limited adaptive histogram equalization, adaptive neighbourhood contrast enhancement, and wavelet based enhancement in a preference study. In a majority of the cases with microcalcifications, the adaptive neighbourhood contrast enhancement algorithm provided the most preferred images (58%), followed by the unsharp masking algorithm. Feature based enhancement methods can be used to enhance both masses and microcalcifications.

Chang and Laine [30] suggested an enhancement algorithm based on overcomplete multiscale wavelet analysis. The algorithm detected directional features and removed unwanted perturbations. Here visual inspection by radiologist suggested that the enhanced image was much more naturally close to original mammogram than those processed with other methods.

Another method proposed by Gagnon *et al.*, [31] put forward a simple multiscale sharpening enhancement algorithm based on the hidden zero crossing property of the complex symmetric daubechies wavelets. The algorithm was tested on low contrast digitized mammograms and to improve visual quality denoising with thresholding was suggested. In this case visual comparison had been done instead of quantitative evaluation of algorithm.

Papadopouloa, Fotiadisb and Costaridouc [32] found that local range modification (LRM) and wavelet based linear stretching suited for enhancement of images with microcalcifications. The databases used here were mini-MIAS and the Nijmegen database while the conclusions were arrived using ROC analysis with area under ROC curve A_z is 0.932 for LRM and 0.926 for the wavelet based linear stretching.

Scharcanski and Jung [33] described an approach for noise suppression and enhancement of mammogram images and that was effective in screening dense regions of the mammograms. The image preprocessing was designed to enhance the local contrast in dense regions adaptive manner. The image denoising process also was adaptive, and the selection of a gain factor provides the desired detail enhancement. This method required less user adjustment parameters and visual comparison had been done with original image.

H Stefanou *et al.*, [34] employed two different methods for image enhancement. The first method utilised correlation between wavelet coefficients at successive levels non linearly to effect adaptive enhancement of mammogram. In the other method typical thresholding and non linear mapping followed by high pass filtering was used. While employing higher levels of decomposition first method was better as blurring does not increase with the levels.

Rajkumar and Raju [35] compared their bit plane decomposition of top hat image with six other thresholding algorithms; SURE shrink, Level dependent wavelet threshold, level dependent Visual shrink, Normal Visual shrink and modified level independent Visual shrink. They have claimed their method to be better with average contrast improvement index (CII) of 1.243.

2.3 Literature survey on image segmentation

Image segmentation classifies or clusters an image into several parts or regions according to a feature of image, like the pixel value or the frequency response. The image segmentation methods can be categorised into region based segmentation, data clustering, and edge base

segmentation. There are three main characteristics which influence the segmentation of an object in an image: object boundaries, object homogeneity and object shape. Object boundaries and object homogeneity are image or signal based characteristics which are therefore affected by image specific disturbances like noise or reconstruction artifacts. They are modality dependent while object shape is modality independent. The concepts of object boundary, object homogeneity and object shape have a strong influence on the development of segmentation methods. Segmentation techniques try to detect boundaries and homogeneous regions in the images and incorporate shape information to restrict the shape of the resulting segmentation [36].

2.3.1 Segmentation techniques on PET images

PET is a functional modality that can be used to visualize pathologies at much finer molecular level. This is achieved by employing radioisotopes that have different rates of intake for different tissues [3]. The inherent noise in the PET images, provide less quantitative information about the qualitative features that can be perceived by experienced medical practitioners. The image regions should be delineated to identify and quantify information from PET images. The segmentation of PET images becomes a difficult task due to the inherently poor spatial resolution and signal to noise ratio. The physical degrading effects such as scatter, attenuation, partial volume effect, and patient motion during scanning add further complications to the segmentation task [37]. The intensity range of PET images is large and the intensity values depend heavily upon clinical factors like injection time and dose of radioisotopes and patient factors like tissue uptake and body weight. Normal tissues also uptake different levels of isotope and sometimes these uptake can be more than the tissues with

lesions. Thus there can be an overlap in the intensity range of normal and abnormal tissue, which makes the segmentation more difficult [11].

The majority of work performed on PET image segmentation utilises thresholding. Amira *et al.*, [38] suggested a method for PET segmentation utilising the Bayesian information criterion, expectation maximisation and multiscale Markov model to model spatial correlations between neighbouring image voxels. Hsu *et al.*, [39] proposed Poisson gradient vector flow with genetic algorithm to automatically find the contour of liver in the PET images.

Li *et al.*, [40] put forward the idea of a two stage method integrating the adaptive region growing algorithm and the dual front active contour model. Spectral clustering and graph based segmentation proposed by Bagci *et al.*, [41] and Yang and Grigsby [42] mitigated the difficulty of segmenting complex boundaries in low contrast images and were found to be superior to the existing thresholding approaches in PET image segmentation. Abdoli *et al.*, [43] presented a deformable active contour model based on the method proposed by Chan and Vese and obtained more accurate tumour volume delineation from PET images.

Zeng *et al.*, [44] proposed volumes of interest segmentation method which employed a hierarchical approach combining improved local and global intensity active surface modelling and alpha matting, and achieved subvoxel segmentation accuracy. Foster *et al.*, [45] propounded a new segmentation algorithm based on clustering approach with the affinity propagation to segment PET images for quantification of tuberculosis in small animal models. A review conducted by Foster *et al.*, [46] on the state of the art image segmentation methods for PET scans of body images, as

well as the recent advances in PET image segmentation techniques, pointed resolution related issues, noise and large variability in the shape, texture, and location of pathologies as factors that significantly affect PET image segmentation. They also indicated the lack of standardization between different segmentation techniques and the need for a publicly available database of PET images for evaluating new and old methods.

Zaidi and Naqa [47] conducted a literature survey and categorised various PET image segmentation methodologies as image thresholding methods, variational approaches, learning methods and stochastic modelling based techniques. Manual methods have time consumption as their major impediment, while hard decision making and sensitivity to motion artefacts attributes to the constraints in thresholding techniques. Variational approaches were sensitive to image noise whereas computational complexity and challenges in feature selection offered limitations to learning methods. Even though stochastic modelling techniques could deal with noise in the PET images, the main concerns were the effect of initialization and convergence to local optimal solutions. This suggested for combination of different methodologies to have a good and effective segmentation [47].

2.3.2 Segmentation of breast region from mammographic images

The methods used to separate the region of interest from the background are usually referred to as the segmentation. In image segmentation, the image is decomposed into regions that are semantically uniform. However, since images themselves provide only semantically poor information, image segmentation is essentially an application oriented problem that requires either strong intervention of human experts or application specific solutions [48].

Breast region segmentation has been a topic of interest in research from as early as 1980s. Many new techniques have been developed in that area. The histogram based techniques and gradient based techniques are early works in this field. The polynomial model based, active contour based and classifier based techniques later joined the band wagon [49].

Segmenting out ROI in mammographic image has proven to be a challenge because normally boundary for breast tissue is not clearly defined. Often, for such analysis, the boundary for the ROI must first be drawn out manually by the radiologist. Nordin et.al [50] suggested a semi automated tool in ROI selection which was more efficient than hand drawn method while still maintaining a significant amount of human control compared to a fully automated method.

Fei Qi, Jinjian Wu and Guangming Shi [51] suggested a method that detect the ROIs automatically based on human visual system (HVS). In this algorithm, the properties of pixels such as the contrast, location and edges are analyzed, and the pixels were enhanced according to the sensitivity of HVS. Then these factors were combined to a salient map, which classifies each pixel of the image in relation to its perceptual importance. Finally, the ROIs were segmented according to the salient map.

Janaki, Tamilarasi and Kumar [52] proposed four techniques based on mixed raster content layering, block based thresholding, region growing and active contour algorithms for determining a ROI that could improve the compression process. The performance of segmentation and compression revealed that the enhanced active contour model followed by mixed raster content based segmentation and region growing algorithm is efficient and could be considered as a promising candidate for image enhancement

techniques for medical imaging systems. The performance was measured in terms of cr and PSNR.

Developing ROI for computer aided diagnosis algorithm would reduce the number of unnecessary biopsies in patients with benign disease and thus avoid patients' physical and mental suffering, with a bonus of reducing health care costs [53]. The accurate segmentation of the breast region in mammograms allowed the search for abnormalities to be limited to the region of the breast without undue influence from the background of the mammogram. It also facilitated enhancements for techniques such as comparative analysis, which includes the automated comparison of corresponding mammograms [54]. Breast segmentation was essential to exclude the background information in analyzing mammogram image [55].

Nagi *et al.*, [53] used morphological preprocessing and seeded region growing (SRG) algorithm to enhance and segment breast profile region from mammogram for using in computer aided detection systems. They have used digital mammogram images acquired from Malaysian patients treated at the Universiti Malaya Medical Centre, Kuala Lumpur and the mini-MIAS database. The performance indices used here are true positive, true negative and false positive.

Maitra *et al.*, [54] suggested a four step algorithm for accurate breast contour detection. The four steps were binary homogeneity enhancement algorithm, followed by edge detection algorithm and breast boundary detection algorithm, and finally proposed breast boundary smoothing algorithm. The results were verified with ground truth using metrics; correctness and completeness.

It was found that entropy of mammogram near breast boundary is high. This fact was utilised by Yadav and Dass [56] to segment breast region from mammograms. They had tested the algorithm on 103 mammographic images taken from CityU image database of different profiles and visual results were evaluated by experts.

Yapa and Harada [57] presented a new algorithm for estimating skin line and breast segmentation using fast marching algorithm. But this algorithm required user involvement for selecting an initial seed region and an end point on the breast edge. The performance of the algorithm was tested on mini-MIAS database and showed a completeness of 0.87 and correctness of 0.99.

Wani *et al.*, [58] compared different breast region segmentation and found Yapa and Harada technique better among others in terms of accuracy of breast segmenting boundary. They found out that histogram modification techniques could not perform well in the presence of noise.

2.4 Current trends in image compression

Image compression is a key issue to be addressed in the area of transmission and storage of images. The storage and transmission of large volumes of image data is a challenging task owing to limited storage space and bandwidth. With the emerging technologies, there are promises of unlimited bandwidth. But the need and availability of images outgrow the increase in network capacity. The high costs involved in providing large bandwidth and huge storage space further necessitates the need for image compression.

Digital imaging and communications in medicine (DICOM) standard was created for the distribution and viewing of medical images such as CT scans MRIs and USs [66]. This standard defined how to encode pixel data either without compression, or by using various irreversible or reversible, nonproprietary image compression schemes. Basically all compression schemes were based on the same technical principles using entropy coding, decorrelation and quantization steps. Arithmetic coding and Huffman coding were the widely used ones in entropy coding. Prediction schemes predicted a certain sample value by a linear or nonlinear combination of its spatial neighbours and encode the difference of the sample value and its prediction (prediction error). A decorrelating transformation enabled spatially correlated input samples to be described by just a few prominent base functions, resulting in a few corresponding weighting coefficients. The statistical distribution of those weighting coefficients, also called transformation coefficients, was not uniform and is suitable to be efficiently encoded by entropy coders. In quantisation, the continuous range transformation coefficients were mapped to a significantly smaller number of representative coefficient values. One measure of image quality that was extensively used was PSNR. PSNR could not correlate well with visual quality, so structured similarity image metric (SSIM) was a better choice as performance measure. Receiver operating characteristic (ROC) methods were used to measure diagnostic accuracy [67].

Information theoretic approach based on minimum relative entropy (MRE) suggested by R Sukanesh, et.al [59] for image compression used region growing for reconstruction. The compression ratio obtained was 12 while maximum PSNR of 33 had been achieved.

Grgic, Ravnjak, and Zovko-Cihlar [60] pointed that wavelet transform had better SNR than JPEG for higher compression ratio. The inference was arrived from experiments on natural images.

Eskicioglu and Fisher [61] listed out Average Difference (AD), Normalised Mean Square Error (NMSE), Normalised Absolute Error (NAE) and Maximum Difference (MD) as some of the image quality measures and suggested the use of graphical evaluation along with numerical quality measures. They proposed Hoska plot as a graphical evaluation tool with superior judgement qualities.

Makhoul [62] gave an exposition of linear prediction in the analysis of discrete signals. The use of linear prediction in data compression was also reviewed. For purposes of transmission, particular attention was given to the quantization and encoding of the reflection (or partial correlation) coefficients.

Huang, *et al.*, [63] studied the correlation properties of wavelet transform coefficients. By employing the high correlation property of wavelet transform coefficients along the same prediction channels, a hybrid image coding system was proposed and designed. For hybrid image coding, a unitary transform had been applied in one direction first for the decorrelation and the prediction filtering was then performed along the other direction for removal of redundancy.

According to Udomhunsakul and Hamamoto [64], wavelet transforms compacted image energy into smaller numbers of coefficients and had good localization characteristics in both the spatial and frequency domain and the choice of wavelet filters was a very vital factor to gain a good coding performance. The evaluation was done on US modality images

and the image quality is measured both subjectively and objectively using MD, NAE and NMSE.

Villasenor, Belzer and Liao [65] opined that regularity was not a sufficient criterion to determine the quality of image compression. Multilevel analysis and synthesis filter bank could be evaluated by considering reconstruction obtained from only lowest level reference signal. The reference signal was finely quantized while details were coarsely quantized. Maximum information about original signal was packed into reference signal. Decomposition could result in artifacts if reference signals alone were used.

Vidhya and Shenbagadevi [68] presented a method for compression in which DICOM images are decomposed by Cohen-Daubechies Feauveau (CDF) biorthogonal wavelet and set partitioning in heirarchical trees (SPIHT) coded. DWT coefficients are organized into different subsets and important ones are transmitted first. This method gives good subjective quality and PSNR exceeding 35dB when compared with JPEG and fractal method.

Shahoseini *et al.*, [69] suggested a method for compression of ultrasound images based on wavelet decomposition, entropy coding and thresholding. The method was evaluated using *cr*, NMSE, NAE and PSNR criterion. The wavelet db1 outperformed other wavelets considered, in *cr* with a value of 12.17% without thresholding and utilising threshold obtained a value 5.54%.

Another method for image compression put forward by Kai *et al.*, [70] performed integer wavelet transform on images and then HVS filter them and finally coded them. HVS filters were used for noise shaping. Here compression was based on contrast sensitivity function. The validation was

done on the medical images including CT and MRI. At the same bit rate, SPIHT method, performed better in terms of PSNR than the proposed algorithm but it can achieve better subjective visual quality, and performs better in the aspects of compression ratios and coding/decoding time. The compression ratios obtained are 17.12 and 15.06 for proposed one and for SPIHT respectively.

Bairagi and Sapkal [71] suggested that biorthogonal4.4 wavelets were most suitable for medical image compression application with least MSE and high PSNR of 23.16 dB. They claimed that images compressed so bore close correlation with the original. The evaluation was done on privately obtained MR and CT images and the results were reassessed subjectively also.

Knezovic *et al.*, [72] suggested pixel prediction on the basis of causal set of surrounding pixels. Contextual error modelling and entropy encoding completed compression procedure. The method was named as classification and blending predictive coder and showed better results for images from different modalities. The performance measure used in this case was bit rate. The proposed method was compared with context based adaptive lossless image coder (CALIC) algorithm, JPEG-LS, and JPEG2000 lossless compression.

Chen and Tseng [73] proposed a lossless wavelet based image compression scheme with adaptive prediction. The correlation between wavelet coefficients was analyzed to identify a proper wavelet basis function, and then predictor variables were statistically tested to determine which relative wavelet coefficients should be included in the prediction model. The prediction differences were encoded by an adaptive arithmetic

encoder. The proposed innovative approach integrating correlation analysis for selecting wavelet basis function with predictor variable selection fully achieves high accuracy of prediction. The wavelet based image compression with adaptive prediction method and four famous lossless compression methods: SPIHT, JPEG2000, CALIC, and SSM, are experimentally compared. The results showed that the proposed method achieved the highest compression rates for CT, MRI, and ultrasound images.

Menegaz [74] reviewed various lossless compression techniques such as differential pulse code modulation, hierarchical interpolation, bit plane encoding, multiplicative autoregression and difference pyramids. Differential pulse code modulation and pyramids offered a *cr* in the range of 1.5-3 and 1.4-3.4 respectively. Even though bit plane coding did not improve *cr*, it outperformed other technique in terms of image quality. The model based multiplicative autoregression was application dependent and complex when it came to implementation. CALIC had proved to be the most effective and, as such, it was often taken as the benchmark for performance in lossless medical image compression.

Zukoski *et al.*, [75] suggested ROI based compression in which lossless compression for ROI and lossy compression for back ground were used. In this approach image was subtracted from prestored image and that residual image is losslessly compressed. An improvement in compression ratio as high as 82% could be obtained when compared with fully lossless JPEG compression.

Ansari and Anand [76] proposed a compression scheme based on Contextual ROI mask, DWT and entropy encoding. The proposed context based DWT and general DWT methods like EBCOT, Implicit and Maxshift

are compared for different cases of US images and cr varied from 8.0018:1 to 128.4705:1 and bpp from 1.0 to 0.0625. The performance parameters MSE, PSNR, coefficient of correlation (CoC), percentage of transform coefficients zeroed and the percentage of energy retained are also calculated. The context based DWT is found to be better.

Ansari and Anand [77] proposed another method in which the contextual part of the image was encoded selectively. Region of interest is coded on the high priority basis with a very low compression rate (high bits per pixel) and the background of the image was separately encoded with a low priority and a high compression rate (low bpp). As a result, high over all compression rates, better diagnostic image quality and improved performance parameters like cr , MSE, PSNR and CoC are obtained. It was found that the proposed method gave more than 10% improvement in the PSNR value, in the bpp range of 0.0625 to 1.00 and the cr value of as high as from 10:1 to 256:1 for the same bit rate with a better quality of the reconstructed medical image judged on the basis of the HVS and the mean opinion scores (MOS).

Dalhbom *et al.*, [78] found that whole body(WB) PET imaging produced the large quantity of data and its short and long term storage was a big problem. With available error free compression techniques compression of about 3:1 could be obtained.

Tsai, *et.al.*, [79] proposed a full frame wavelet image coding approach for WB PET images. It adopted the zero tree data structure, bit plane coding and adaptive arithmetic coding to improve the coding efficiency. This lossy image compression increased the data size reduction

and kept the reconstructed images visually indifferent to the original images at compression ratio up to 10:1 in clinical image quality evaluation.

Euclid Seeram [80] in his study observed that a literature survey showed that image compression studies in molecular images are sparse. An early study reported the *cr* of 10.8-20 using the discrete cosine transform for lossy compression of cardiac nuclear images. Another method using wavelet and SPIHT algorithm reported a *cr* of 90:1 for static liver images. The investigation of the impact of wavelet compression at different quality levels (degrees of quantization) on radioisotope image quality using the modulation transfer function of images was done. The authors concluded that in the higher quality levels, wavelet compression smoothed the data and preserved most diagnostic information in the images.

Dahlbom *et al.*, [81] achieved compression of WB PET by removing all negative values and by masking the transaxial images such that all pixel elements located outside the body contour were set to zero. Three different masking schemes based on geometrical shapes (circular, rectangular and elliptical) were evaluated and compression ratios close to 1:6 was achieved.

Masood *et al.*, [82] did literature survey for brain image compression and highlighted several methods used in brain PET image compression. A method based on the masking concept provided a *cr* of 7. Another method for 3D PET compression utilised adaptive differential pulse coded modulation and a universal variable length coder to carry out the compression process.

Wang and Huang [83] detected the breast boundary by comparing the gray levels in a neighbourhood. The breast was segmented from non

breast region and breast region is compressed using a predictive lossless technique while the information in the non breast region is discarded and obtained an average compression ratio of about 7:1. Digital mammograms were compressed on the fly while they are created.

Wong, Guan, and Kong [84] utilised a self organising neural network to segment breast region from non breast regions. Here also non breast region was discarded and breast region was compressed using nearly lossless JPEG and obtained an average compression ratio of 9.80:1.

Grinstead *et al.*, [85] used content based image compression to mammography. By using a quad tree fractal encoding scheme to generate focus attention area (ROI), a combination of lossy and lossless techniques provided compression 4-6 times that of standard lossless compression and maintained fidelity of ROI and obtained compression ratio 14:1 on average.

Maxshift method suggested by Askelof, Carlander and Christopoulos [86] was based on scaling of the wavelet coefficients after the wavelet transformation and quantization. By sufficiently scaling the wavelet coefficients used to reconstruct the ROI, all the information pertaining to the ROI was placed before the information pertaining to the rest of the image (background), in the code stream. By varying the quantization of the image and by truncation of the code stream, different quality for the ROI and the background could be obtained. The increase in file size for the image due to the ROI coding was approximately a few percent.

A selective coefficient mask shift (SCMShift) coding method was proposed by Tahoces *et al.*, [87]. The technique, implemented over ROIs, was based on shifting the wavelet coefficients that belong to different

subbands, depending on the coefficients relative to the original image. This method allowed: (1) codification of multiple ROIs at various degrees of interest, (2) arbitrary shaped ROI coding, and (3) flexible adjustment of the compression quality of the ROI and the background. No standard modification for JPEG2000 decoder was required. An average compression ratio of 16:1 was achieved.

Rapesta, Sagrista and Llinas [88] introduced a ROI coding method that was able to prioritize multiple ROIs at different priorities, guaranteeing lossy to lossless coding. The proposed ROI coding through component prioritization method used techniques of rate distortion optimization combined with a simple yet effective strategy of ROI allocation that employed the multicomponent support of JPEG2000 code stream. ROI coding through component prioritization method allowed progressive lossy to lossless recovery for the ROI and the background, did not penalize the coding efficiency, permitted to recover exclusively a requested ROI through the component scalability feature of JPEG2000, and achieved a fine grain accuracy.

2.5 Conclusion

This chapter helps to understand the works done currently in the areas of enhancement, segmentation and compression in case of PET and mammographic images. The lack of a common reference database of images representing different imaging modalities and/or pathologies impedes a clear classification and comparison of the many of the proposed algorithms.

CHAPTER 3

IMAGE ENHANCEMENT USING STATIONARY WAVELET TRANSFORM AND UNSHARP MASKING

3.1 Introduction

The motivation of this work is the development of a ROI based compression scheme for medical images. The ROI separation can be better effected if the image is preprocessed before ROI segmentation. Preprocessing techniques are applied to improve the readability of the image which helps in more correct diagnosis. The popular preprocessing techniques are enhancement, normalization, noise removal, image resampling, mathematical operations and manual correction. A good preprocessing techniques that can make effective segmentation of the images under study is found to be image enhancement. Image enhancement processes consist of a collection of techniques that seek to improve the visual appearance of an image or to convert the image to a form better suited for analysis by a human or a machine. It accentuates or sharpens image features such as edges, boundaries, or contrast to make a graphic display more helpful for display and analysis. The enhancement does not increase the inherent information content of the data, but it increases the dynamic range of the chosen features so that they can be detected easily.

Image enhancement improves the acuity of image by modification of intensity functions, image spectral content or by mixture of these. The enhancement operations include removing and blurring noise, increasing contrast and revealing details. Enhancement of certain features can

sometimes be accompanied by undesirable effects. The valuable information can be lost or enhanced image may be a poor representation of the original. While going for enhancement it should be kept in mind that enhancement cannot provide any information that is not in the original image. If the image does not contain the feature to be enhanced then enhancement will only improve noise and unwanted components in the image.

Medical images are often deteriorated due to noise from various sources of interference and other phenomenon that affect measurement in imaging and data acquisition systems. The nature of physiological system under investigation and procedures used in imaging reduce the contrast and visibility details. In many medical images the discernment between normal and abnormal tissue is indistinct. So if noise levels are relatively high accurate diagnosis becomes difficult. Enhancement, in many cases improves the quality of image and this facilitates correct and quick diagnosis. In general, enhancement gives clearer image for a human observer while they form a preprocessing step for automated analysis.

Keeping the need of image enhancement in ROI selection in ROI based compression, two methods, closely related are developed for enhancement of PET images and mammographic images. Next, in this chapter, the premises around which the newly developed preprocessing technique is based, an overview of various image enhancement techniques used with medical images, explanation of the developed method and the results are discussed.

3.2 Background

The image enhancement techniques used with medical images and the philosophies like stationary wavelet transform (SWT), modulus maxima and unsharp masking on which the new algorithm is based are discussed in this section.

3.2.1 Image enhancement techniques used with medical images

Image enhancement techniques that are used with medical images [89] are mainly categorised as pixel based, transformation based, local operator based, multiple image based and spectral domain based. The pixel based techniques take only pixel gray level value and does not take the values of neighbourhood and whole image characteristics into consideration. The display systems have non linear characteristics resulting in non linear intensity profile of the image when displayed. A transform inverse to the non linearity of the display is applied for correction. The determination of non linearity characteristic could be difficult in practice.

Intensity scaling is another method of image enhancement which can be utilised when dynamic range of the acquired image exceeds or is below par than the characteristics of display system. It allows the observer to focus on specific intensity bands that may be of special interest to the observer. If f_1 and f_2 define the intensity band of interest, a scaling transformation is defined as

$$e = \begin{cases} f \rightarrow f_1 \leq f \leq f_2 \\ 0 \rightarrow otherwise \end{cases} \quad (3.1)$$

$$g = \left\{ \frac{e - f_1}{f_2 - f_1} \right\} \cdot f_{\max} \quad (3.2)$$

where e is an intermediate stage, g is the output image and f_{\max} is maximum intensity of the display.

Even though intensity scaling enhances the image information present in specific intensity bands effectively, it cannot give apriori information to identify the useful intensity bands. If we can maximise the information conveyed from the image to the user by distributing the intensity information from the image as uniformly as possible over available intensity band, it will be useful. The normalised histogram of the image is interpreted as probability density function of the intensity image in this approximate realisation of information theoretic approach. The histogram equalisation method belongs to this approach and in this method the histogram of the input image is mapped to a new maximally flat histogram.

The histogram of any image can be defined as

$$h(i) = \sum_{m=0}^{M-1} \sum_{n=0}^{N-1} \delta(f(m, n) - i), \rightarrow i = 0, 1, \dots, P - 1 \quad (3.3)$$

where f is intensity of the pixel; m and n define the pixel position; P is the maximum number gray levels in the image;

$$\delta(w) = \begin{cases} 1 \rightarrow w = 0 \\ 0 \rightarrow otherwise \end{cases} \quad (3.4)$$

The total number of pixels in the image $M \times N$ is also the sum of all the values in $h(i)$. So in order to distribute the intensity profile of the image most uniformly, each bin of the histogram should have a pixel count of $(M$

$\times N)/P$. For redistribution of pixels in the image we need to know normalised cumulative histogram $H(j)$.

$$H(j) = \frac{1}{M \cdot N} \sum_{i=0}^j h(i) \rightarrow j = 0, 1, \dots, P-1 \quad (3.5)$$

The normalized cumulative histogram is used to map the original gray levels in the image and the new gray levels required for enhancement. The enhanced image $g(m,n)$ will have a maximally uniform histogram and defined as follows:

$$g(m,n) = (P-1) \cdot H(f(m,n)) \quad (3.6)$$

Local operators enhance the image by providing new value for each pixel in a manner that depends only on the pixel under consideration and pixels in its neighbourhood. The local operators include linear spatial filters implemented with kernel convolution, non linear operators and local area histogram equalization. Noise suppression by mean filtering, median filtering, and edge enhancement also belong to this type of enhancement.

In multiple image based enhancement techniques we have image averaging and image subtraction methods. Image averaging is used when large number of input images are available and noise is additive in nature with zero mean and is independent of the image. Image subtraction is performed with two images having considerable similarities between them to enhance the differences between them.

Linear filters can also be implemented in frequency domain by modifying Fourier transform of the original image and taking the inverse Fourier transform. When an enhanced image $g(m,n)$ can be obtained by

convolving an original image $f(m,n)$ with kernel $w(m,n)$

$$g(m, n) = f(m, n) * w(m, n) \quad (3.7)$$

The convolution theorem states that $G(u,v)$, the fourier transform of $g(m,n)$ is given by

$$G(u, v) = F(u, v) \cdot W(u, v) \quad (3.8)$$

where $F(u,v)$ and $W(u,v)$ are the fourier transforms of the image and kernel respectively. Here the enhancement is directly obtained in the frequency domain by multiplying $F(u,v)$ with $W(u,v)$ on pixel to pixel basis.

Even though there exist many algorithms for image enhancement, additional algorithms are required for further improvement in image quality. Computationally more intensive algorithms take the advantages of context based and object based information in the image. The diverse nature of the medical images and their associated problems make it difficult to prescribe a single method for enhancement that can solve all the difficulties.

3.2.2 Stationary wavelet transform

Many new algorithms have been proposed in the area of image enhancement in the wavelet domain till recently. DWT is one of the wavelet transforms used in image processing. DWT decomposes an image into different subband images, which gives approximation of the image, vertical details, horizontal details and diagonal details [90]. The SWT is another transform which has been used in several image processing applications.

The basic idea of SWT is to fill the gap caused by decimation in the standard wavelet transform. This results in over determined representation

of the original data, having much statistical potential [91]. The SWT is an inherently redundant scheme as the output of each level of SWT contains the same number of samples as the input. So for a decomposition of N levels, there is a redundancy of N in the wavelet coefficient. SWT is similar to the DWT except that the filters are up-sampled instead of sub-sampling the signal at each level of decomposition. Each level's filters are up-sampled versions of the previous ones. The one dimensional SWT decomposition is stated here to have a clear understanding of two dimensional signals, i.e., images. The decomposition and filters are shown in Fig 3.1 [92].

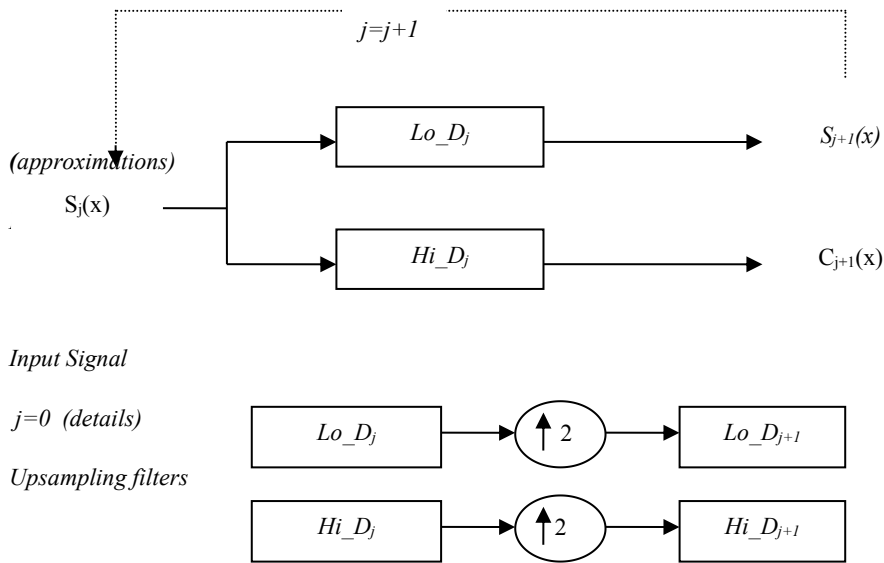


Fig. 3.1 SWT decomposition and filters

In Fig 3.2, the two dimensional SWT decomposition along with filters are shown. H_j and L_j represent high pass and low pass filters at scale j , resulting from interleaved zero padding of filters H_{j-1} and L_{j-1} ($j > 1$). LL_0 is the original image and the output of scale j , LL_j , would be the input of scale $j+1$. LL_{j+1} denotes the low frequency (LF) estimation after the stationary

wavelet decomposition, while LH_{j+1} , HL_{j+1} and HH_{j+1} denote the high frequency (HF) detailed information along the vertical, horizontal and diagonal directions, respectively.

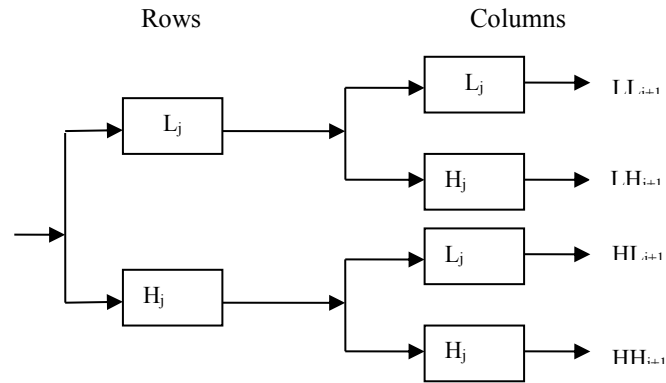


Fig. 3.2 Two dimensional SWT decomposition and filters

The single level decomposition and reconstruction using SWT of standard image 'rice' is shown in Fig 3.3.

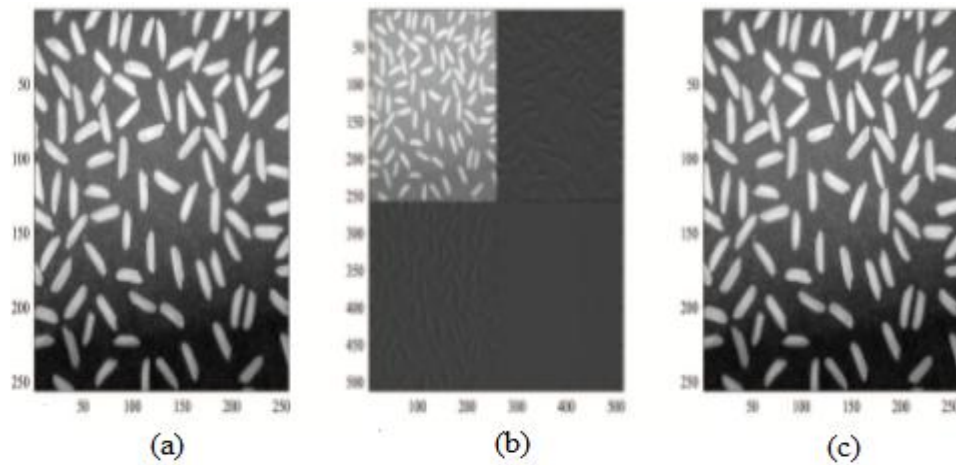


Fig. 3.3 Decomposition and reconstruction using SWT (a) Original Image (b) Single level decomposed coefficients (c) Reconstructed image

3.2.3 Modulus maxima and Detail modulus

The modulus maxima of the wavelet transform provide a nearly complete characterization of an image. A definition of local maxima of the wavelet transform modulus is: Let $Wf(s, x)$ be the wavelet transform of a function $f(x)$. The modulus maximum is any point (s_0, x_0) , such that $|Wf(s_0, x)| < |Wf(s_0, x_0)|$ when x belongs to either a right or the left neighborhood of x_0 , and $|Wf(s_0, x)| \leq |Wf(s_0, x_0)|$ when x belongs to the other side of the neighborhood of x_0 . The local maxima of the wavelet transform modulus provide enough information to detect and analyze all discontinuities inside images [93]. Consider wavelet decomposition of an image $f(x, y)$ at scale j , an approximation and three detail images represented as $W_j^h f$, $W_j^v f$ and $W_j^d f$, where the superscripts h , v and d denote the horizontal, vertical and diagonal details, are obtained. Mallat and Zhong characterize the image edges at scale j by the local modulus maxima denoted as $M_j f$

$$M_j f(x, y) = \sqrt{|W_j^h f(x, y)|^2 + |W_j^v f(x, y)|^2} \quad (3.9)$$

The detail modulus can be thought of as an extension of wavelet modulus maxima. Considering the fair treatment of edges at different orientations, detail modulus can be defined as

$$D_j f(x, y) = \sqrt{|W_j^h f(x, y)|^2 + |W_j^v f(x, y)|^2 + |W_j^d f(x, y)|^2} \quad (3.10)$$

The detail modulus gives a better characterisation of edges making it useful for image enhancement [94].

3.2.4 Unsharp masking

Unsharp masking is explained here in frequency domain. The image is effectively scanned with two overlapping apertures, one at normal resolution and the other at a lower spatial resolution, which upon sampling produces normal and low resolution images $F(j,k)$ and $F_L(j,k)$, respectively. An unsharp masked image

$$G(j,k) = \frac{c}{2c-1} F(j,k) - \frac{1-c}{2c-1} F_L(j,k) \quad (3.11)$$

is then generated by forming the weighted difference between the normal and low resolution images, where c is a weighting constant. Typically, c is in the range $3/5$ to $5/6$, so that the ratio of normal to low-resolution components in the masked image is from 1.5:1 to 5:1. Fig 3.4 illustrates typical scan signals obtained when scanning over an object edge [95].

The masked signal has a longer duration edge gradient as well as an overshoot and undershoot, as compared to the original signal. Subjectively, the apparent sharpness of the original image is improved. A low resolution image is obtained by the convolution of the image with a uniform $L \times L$ impulse response array. The sharpening effect is stronger as L increases and c decreases. High boost filtering is a type of unsharp masking [96].

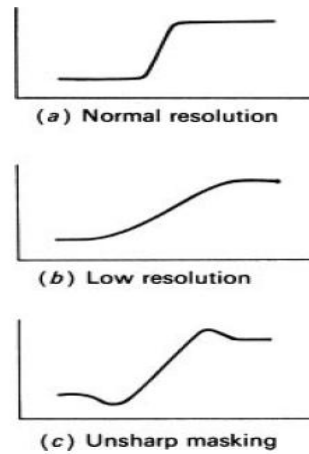


Fig. 3.4 Waveform in unsharp masking image enhancement system

A high boost filter can be defined as a weighted combination of original image ($I_{Original}$) and the high pass filtered version of the image ($I_{Highpass}$). It is also called as high frequency emphasis filter. The high boost filter I_{HBF} is defined as

$$I_{HBF} = K.I_{Original} + I_{Highpass} \quad (3.12)$$

The weight is decided by K and weighted version of original image is added to the high pass filtered image to get high boost filtered image [97]. The high boost filter not only preserves the low frequency information but also enhances the high frequency detail information. This enhances the similarity feature value within similar regions and dissimilarity feature value among the dissimilar regions. The high boost filter is simple and implementation cost is less.

3.3 Measures to quantify image enhancement techniques

Any image processing algorithm can be evaluated in two ways- subjectively and objectively. The subjective evaluation assess the image processing procedure by visual appeal while objective evaluation gives a numerical value as feedback on the assessment of the method. The greatest difficulty in image enhancement is quantifying the criterion for enhancement and, therefore, a large number of image enhancement techniques are empirical and require interactive procedures to obtain satisfactory results.

The objective measures used here for measuring enhancement are contrast, measure of enhancement, entropy, contrast improvement index and PSNR. The contrast of an image is evaluated by employing the metric function given:

$$C_c = \frac{1}{MN} \sum_{i=1}^M \sum_{j=1}^N f'^2(i, j) - \left| \frac{1}{MN} f'(i, j) \right|^2 \quad (3.13)$$

where M and N are height and width of the image, respectively, and $f'(i, j)$ is the enhanced image. The larger the value of C_c , the better the contrast of the image.

A quantization measure of contrast enhancement defined by a CII, is expressed as

$$CII = \frac{C_{processed}}{C_{original}} \quad (3.14)$$

where $C_{processed}$ and $C_{original}$ are the contrasts of the processed and original images, respectively. C is the average value of the local region contrast in the processed or original image. Thus, the CII value of original image is

equal to one. The local contrast is measured as $(X_{\max} - X_{\min}) / (X_{\max} + X_{\min})$ in its local window size while X is the intensity of the pixel[98].

The measurement of enhancement or measure of improvement (EME) is another performance measure used in this work. For defining enhancement measure by entropy (EMEE), consider an image $x(n,m)$ be split into $k_1 k_2$ blocks $w_{kl}(i,j)$ of sizes $l_1 \times l_2$. EMEE is given as

$$EMEE = \max_{\phi \in \{\Phi\}} \chi(EME(\phi)) \quad (3.15)$$

where $\chi(EME(\Phi))$ is defined as

$$\chi(EME(\phi)) = \left(\frac{1}{k_1 k_2} \sum_{i=1}^{k_1} \sum_{j=1}^{k_2} \frac{I_{\max; k, l}^w}{I_{\min; k, l}^w} \log \frac{I_{\max; k, l}^w}{I_{\min; k, l}^w} \right) \quad (3.16)$$

Enhancement is pointed by a value for EMEE higher than one [99].

Entropy is a statistical measure of randomness that can be used to characterize the texture of the input image. Entropy is defined as given below

$$H = -\sum p^* \log_2 p \quad (3.17)$$

where p contains the histogram counts . In another words, it is defined as

$$H = -\sum_{i=1}^L P(i) \log_2 P(i) \quad (3.18)$$

where $P(i)$ is the probability of occurrence of i^{th} gray level and L is the number of gray levels. A higher value in entropy indicates better quality of the image.

PSNR can also be used as a measure to quantify enhancement. It is defined as

$$PSNR = 10 \log_{10} \frac{(L-1)^2}{\frac{1}{MN} \sum_{i=1}^M \sum_{j=1}^N [f'(i,j) - f(i,j)]^2} \quad (3.19)$$

where $f(i,j)$ is the original image of size $M \times N$, $f'(i,j)$ is the enhanced image and $L-1$ is the maximum possible value in $f(i,j)$. A small value of PSNR indicates that image is of poor quality [8].

The image quality evaluation methods can also be classified as full reference methods and no reference methods. In full reference image quality assessment methods, the image quality is evaluated by comparing it with a reference image that is assumed to have perfect quality while no reference metrics assess the quality of an image without any reference to the original one.

3.4 Proposed enhancement using SWT and unsharp masking

The proposed method starts with 2D SWT decomposition of the image and finding the detail modulus of each level. Using absolute maximum of the modulus and a threshold T_n , only some of detail coefficients are retained while the rest is discarded. A high pass filtered image is obtained by discarding all the remaining coefficient, and it is used for high boost filtering. The enhanced image is obtained by adding high pass filtered image to the original one. The algorithm can be modified to suit different types of medical images. The flow chart for generalised algorithm is given below in Fig 3.5

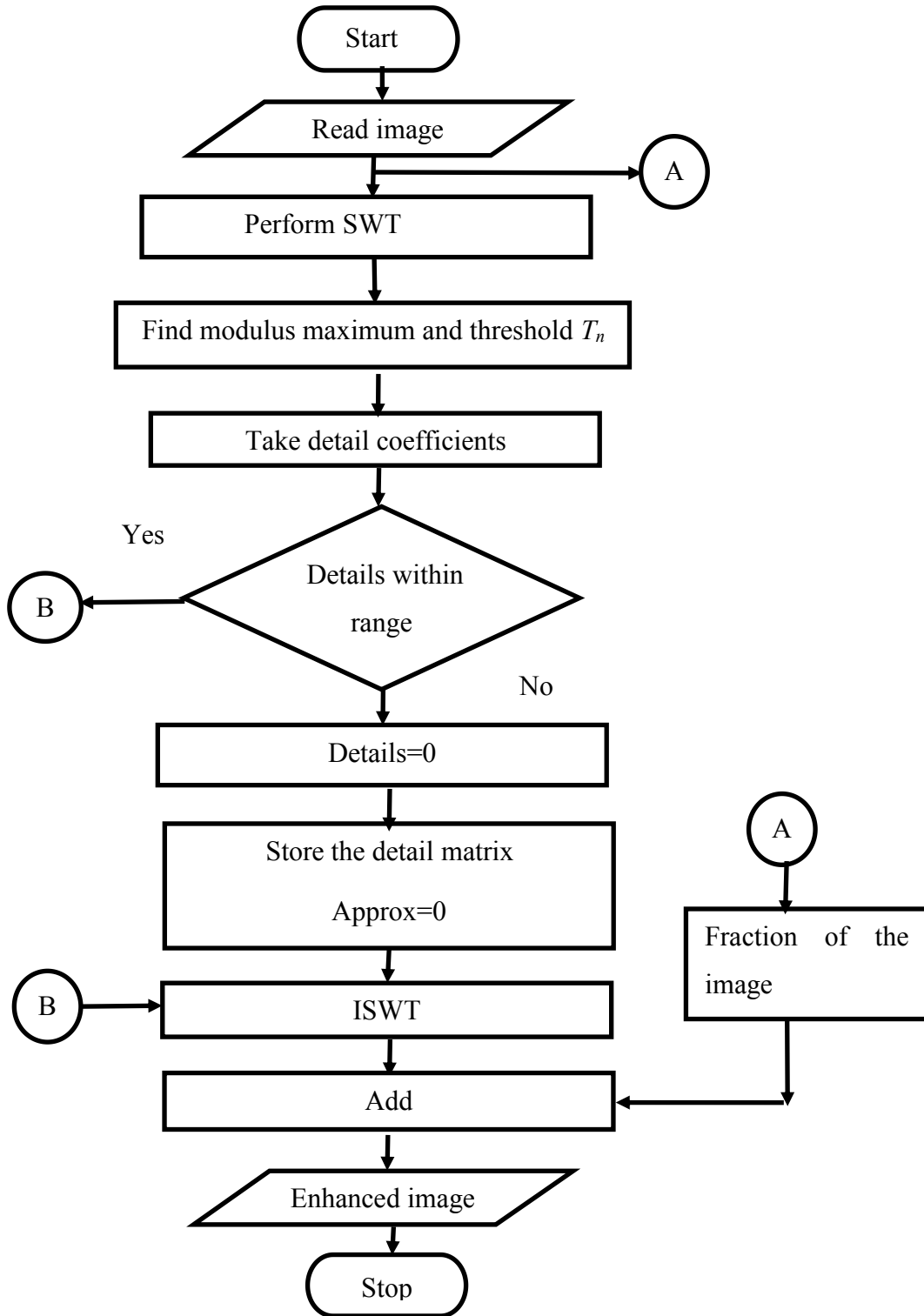


Fig. 3.5 Generalised flow chart of proposed enhancement algorithm

3.4.1 Enhancement of PET images

The generalised algorithm described in the previous section is applied with slight modifications to suit enhancement of PET images. SWT is performed on the image up to 3 levels. For each level, the absolute maximum wavelet coefficient, called detail modulus maximum, is computed. A threshold number T_n is set to include all wavelet coefficients whose absolute value is within the range of the threshold of the wavelet detail modulus.

Let $D_{if}(x,y)$ be detail modulus of the image at the level i which has highest absolute value M_i among all the coefficients of each scale. Any wavelet coefficients $Wf(2^i, x, y)$ at each scale satisfying either of the following:

$$\begin{aligned} Wf(2^i, x, y) &\leq -M_i + T_n \text{ if } Wf(2^i, x, y) < 0; \\ Wf(2^i, x, y) &\geq M_i - T_n \text{ if } Wf(2^i, x, y) \geq 0. \end{aligned} \quad (3.20)$$

are kept unchanged, whereas all the other wavelet coefficients are set to zero before the reconstruction of the image. The approximation is also put to zero and the inverse SWT is calculated. The resultant image contains only details in the image. This high pass filtered image is the reconstructed image. The original image is enhanced by adding reconstructed image to the original. Fig 3.6 shows the enhancement of an image using the proposed method.

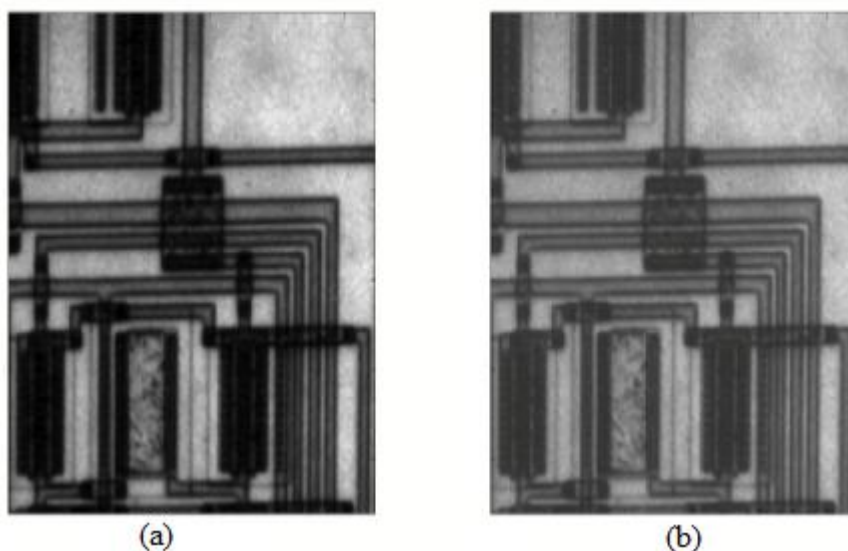


Fig. 3.6 Result of proposed method (a) Original and (b) Enhanced image

3.4.2 Enhancement of mammographic images

The method used is same as in previous sections. For mammographic images absolute maxima of wavelet coefficient is used instead of detail modulus. SWT is performed on the cropped image of size 256 x 256 up to 3 levels. For each level, the absolute maximum wavelet coefficient, called wavelet modulus maximum, is computed. Applying determined threshold T_n on the absolute maxima of wavelet modulus, only a few detail coefficients are retained. A high pass filtered image obtained as a result of reconstruction and a fraction of this is used for unsharp masking. The algorithm is shown below:

Algorithm

1. Get the input image
2. Divide the image into blocks of size 256 x 256.
3. Find SWT of the block
4. Obtain modulus maxima and decide the threshold

5. Check if details lie within range specified by modulus and threshold store it otherwise make details zero
6. Put approximation to zero
7. Perform ISWT with new approximation & details which results in HPF image
8. Add a fraction of result from step7 to image from step2 to get the enhanced image

The original image and image from result of the proposed method is given Fig 3.7

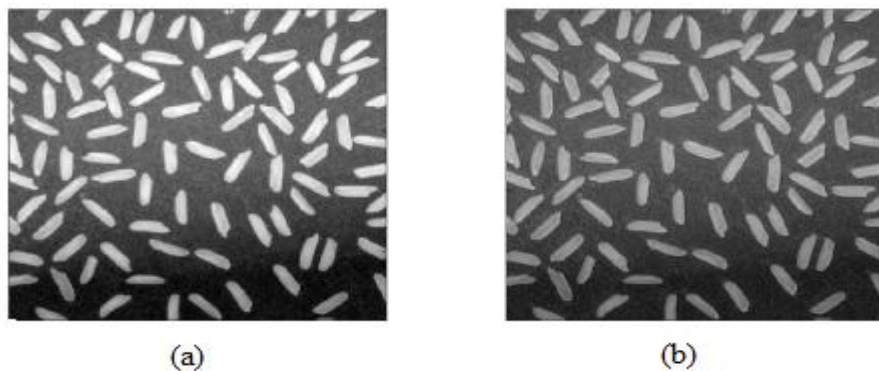


Fig. 3.7 Result of proposed method (a) Original and (b) Enhanced image

3.5 Results and Discussion

The results of the algorithm are discussed for both PET images and mammographic images. The validation for PET images is done on Oncopet_DB database while for mammographic images the mini-MIAS database is used.

3.5.1 PET images

Oncopet DB is a freely available realistic simulated database of whole body ^{18}F -FDG PET images for oncology. SUV are used to measure FDG uptake. The SUV normalisation of FDG uptake for the body surface

area is used here. This normalisation is minimally affected by body size [100].

To reduce the complexity of computation each of the axial slices is taken one by one and processed. The wavelet chosen here is *symlet5*. The original and enhanced slice from the PET image without any lesion is shown in Fig 3.8 while Fig 3.9 shows that of an image having two lesions.

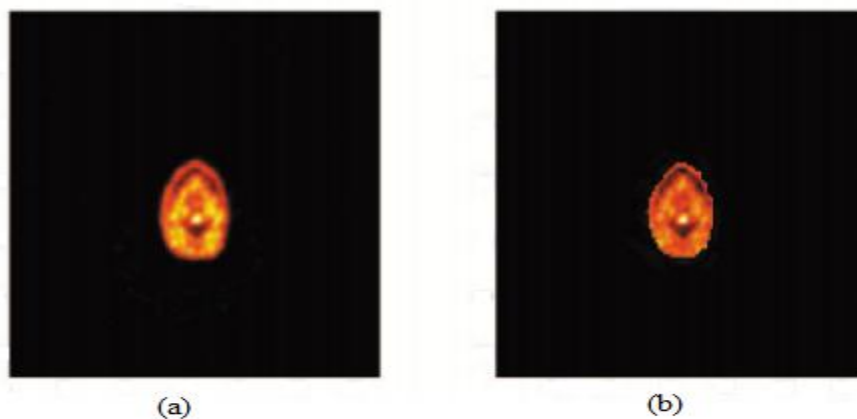


Fig. 3.8 (a) Original and (b) Enhanced slices having no lesion

The contrast, CII, EMEE, entropy and PSNR of the corresponding slices in the original and enhanced images are calculated and compared.

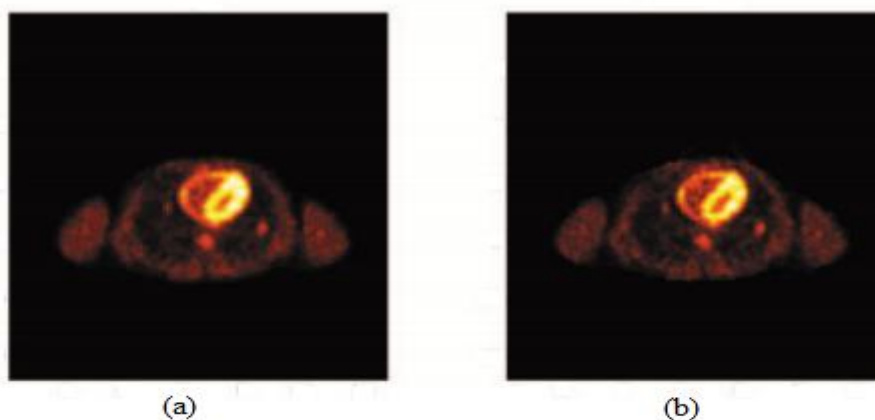


Fig. 3.9 (a) Original and (b) Enhanced slices having two lesions

The plot of average contrast of images with lesions and without lesions and that of the enhanced images are shown in Fig 3.10(a,b). A clear improvement in contrast is observed in the images enhanced using the proposed method. The average value of contrast for normal images is increased by about 40 after enhancement, while for images having lesions it is increased by about 22.

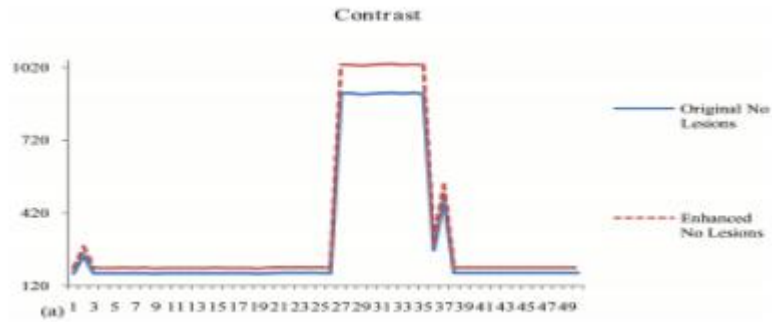


Fig. 3.10 (a) Contrast of original and enhanced images having no lesion

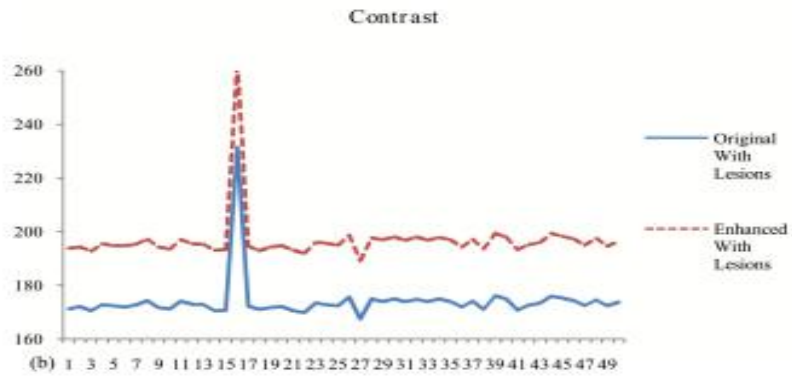


Fig. 3.10 (b) Contrast of original and enhanced images having lesions

The mean CII for images with lesions and without lesions are measured as 11 and 16 respectively using the proposed method. The local contrast is obtained by dividing the image into blocks of size 7x7 pixels. This window size gives optimum value for CII.

The average value of EMEE for normal images as well as those having lesions is increased by an amount of 3. The average EMEE for normal and abnormal images in original and enhanced versions are plotted in Fig 3.11. A boost of about 2 in average entropy value is obtained for normal images as well as images with lesion.

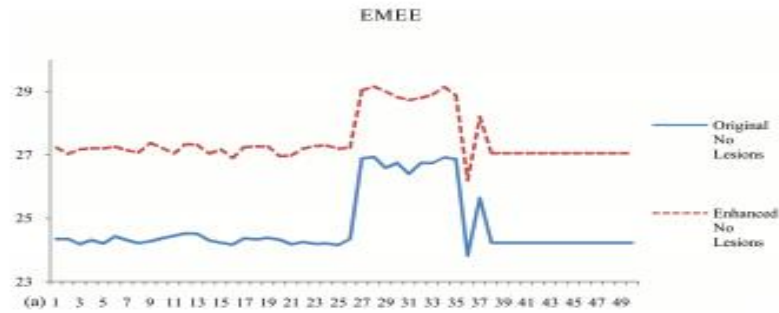


Fig. 3.11 (a) EMEE of original and enhanced images having no lesion

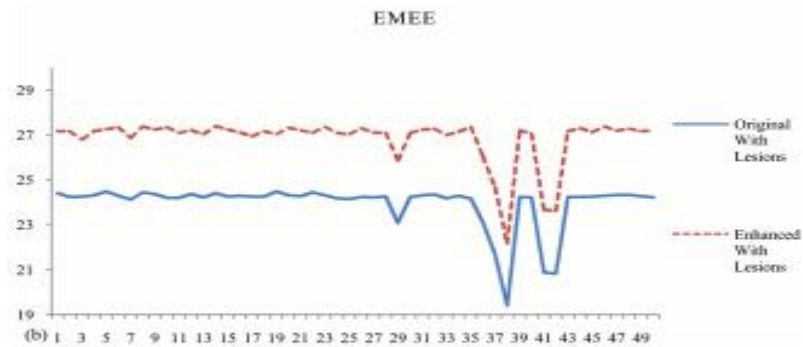


Fig. 3.11 (b) EMEE of original and enhanced images having lesions

The PSNR value in decibels is calculated between the corresponding slices in the original and enhanced images. The plot of average PSNR value of images with and without lesions is given in Fig 3.12 and it clearly shows the occurrence of enhancement. The average

value of PSNR in dB for images with lesions is 39.97 while for normal images it is 39.87.



Fig. 3.12 PSNR of images with and without lesions

The proposed method used detail modulus of SWT coefficients and high boost filtering to achieve enhancement of PET images. The performance measures viz., contrast, CII, EME, entropy and PSNR are evaluated and they clearly show the enhancement. Hence it is evident that the proposed method is suitable in improving diagnostic information from PET images.

3.5.2 Mammographic images

The mini-MIAS database of mammograms contains 322 images of size 1024x1024. It also includes radiologist's 'truth'-markings on the locations of any abnormalities that may be present. Normal images as well as images containing various types of abnormalities were enhanced using proposed method. The results of enhancement for various types of normal and abnormal mammogram images are shown in Fig 3.13(a-e).

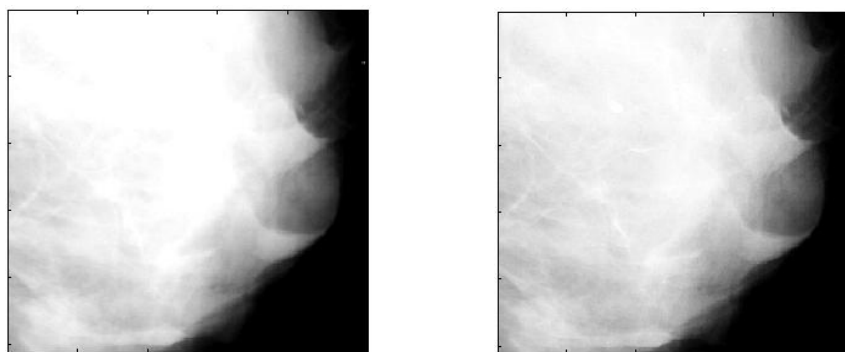


Fig. 3.13 (a) Original(L) and enhanced(R) images with circumscribed mass

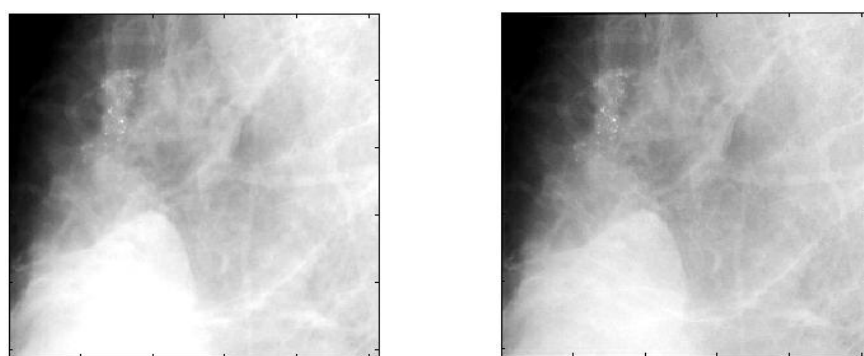


Fig. 3.13 (b) Original(L) and enhanced(R) images with microcalcification

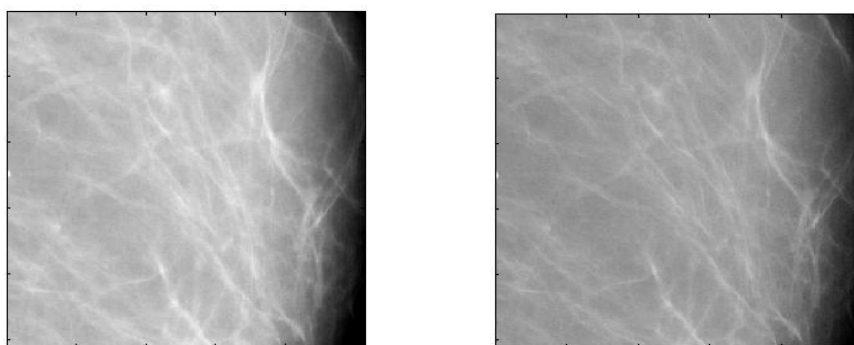


Fig. 3.13 (c) Original(L) and enhanced(R) images with no abnormality

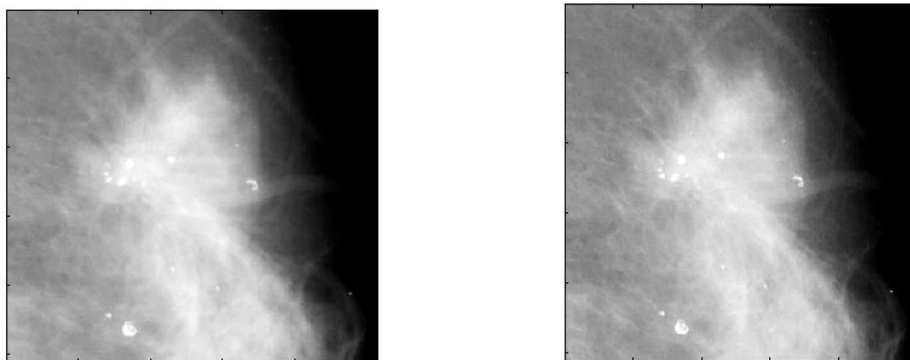


Fig. 3.13 (d) Original(L) and enhanced(R) images with architectural Distortion

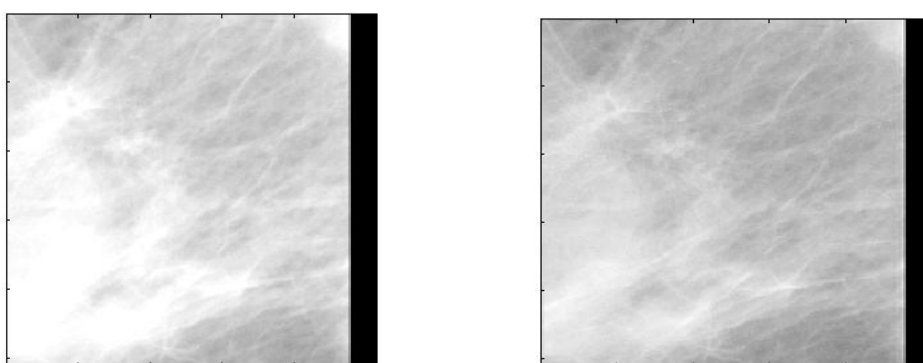


Fig. 3.13 (e) Original(L) and enhanced(R) images having spiculated mass

The image enhancement is quantified by performance measures like contrast, CII, EMEE and PSNR. The average value of performance measures for each type of image in the database is calculated and the results are tabulated in Table 3.1 which clearly show the improvement in image quality.

Table 3.1 Comparison of performance measures for different types of images

Type of image	Original / Enhanced	Performance Measures			
		<i>Contrast</i>	<i>EMEE</i>	<i>CII</i>	<i>PSNR</i>
Circumscribed Mass	Original	1105.61	2.30	1.32	35.86
	Enhanced	1122.72	2.75		
Microcalcification	Original	1335.62	2.59	1.64	35.88
	Enhanced	1368.75	2.98		
Normal	Original	176.21	1.74	1.08	37.68
	Enhanced	181.59	2.15		
Architectural Distortion	Original	1077.07	2.23	1.24	36.31
	Enhanced	1104.37	2.74		
Miscellaneous	Original	739.24	2.23	1.32	36.12
	Enhanced	770.41	2.63		
Spiculated Mass	Original	1740.12	1.97	1.52	35.03
	Enhanced	1791.59	3.31		

The plots of contrast and EMEE against different types of images are shown in Fig 3.14 and Fig 3.15 respectively.

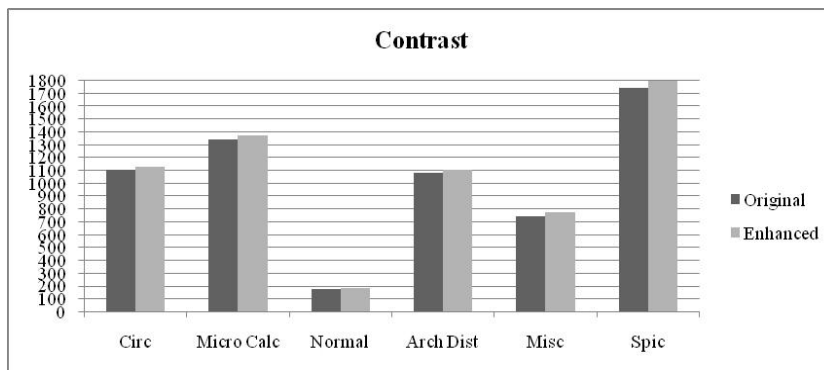


Fig. 3.14 Contrast comparison of original and enhanced images

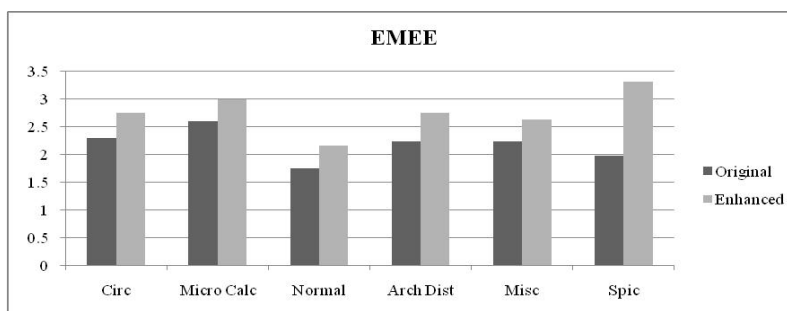


Fig. 3.15 Comparison of EMEE for original and enhanced images

From the pie chart of CII given in Fig 3.16 we can see that there is not much difference in CII between different categories of images. The overall contribution to CII from normal images is found to be less than those images with abnormalities. The minimum CII for normal images as is expected as normal images are having uniform gray level distribution.

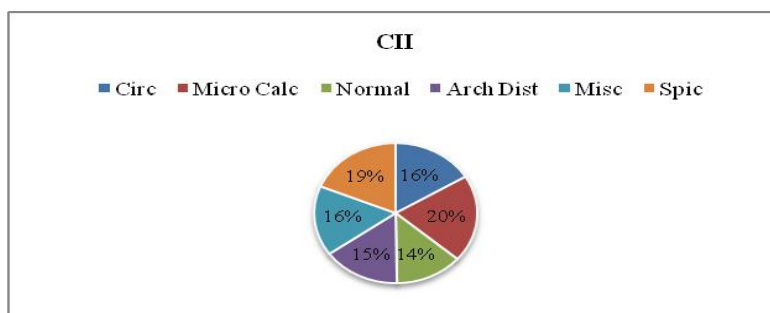


Fig. 3.16 Pie Chart of CII

Rajkumar K K and G Raju [35] compared enhancement techniques based on wavelet and top hat filtering and bit plane wavelet decomposition methods in terms of average CII using same database. The comparison shown in Table 3.2 indicates that the proposed method offers a better CII.

Table 3.2: Comparison of CII in different enhancement methods

Method	CII
Top Hat	1.027
Wavelet decomposition (Sure Shrink)	1.165
Top Hat +Sure Shrink	1.242
Top Hat + level dependent Wavelet Shrink	1.203
Top Hat +Visual Shrink	1.186
Top Hat +level dependent Visual Shrink	1.188
Top Hat +modified level independent Visual Shrink	1.185
Top Hat +Bit Plane decomposition	1.069
Proposed method	1.353

The PSNR values also indicate enhancement in the quality of images. The plot shown in Fig 3.17 suggests that normal images show better PSNR.

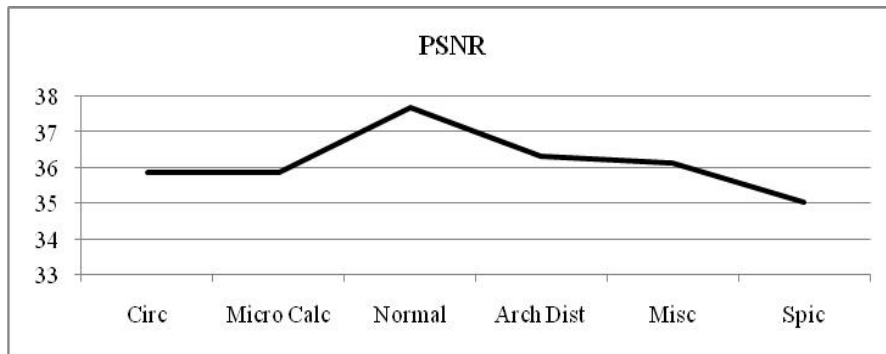


Fig. 3.17 PSNR Comparison

The use of SWT and modulus maxima removes the noise present in the image and makes it visually appealing. The enhancement is demonstrated both subjectively and objectively using contrast, EMEE, CII and PSNR. The increase in contrast is found to be less for normal images when compared with the ones having any sort of abnormality which is in agreement with the already known fact that the contrast is more for images having any kind of abnormality. Thus it can be concluded that this method may be used as a preprocessing step in computer aided diagnosis of breast cancer from mammographic image

3.6 Conclusion

This chapter deals with the development of an image enhancement technique as a preprocessing step prior to ROI segmentation. The enhancement technique developed utilizes SWT and detail modulus. The technique is modified using modulus maxima to suit mammographic images. The developed method is evaluated objectively using various measures.

CHAPTER 4

SEGMENTATION OF REGION OF INTEREST

4.1 Introduction

ROI based compression is the scheme of compression in which diagnostically important regions are compressed with a lower compression ratio while the remaining region termed BG is compressed with higher compression ratio. Thus both the requirements i.e., high quality and high compression ratio are met in a go. The separation or extraction of ROI is done by image segmentation. Segmentation is the partitioning of an image into meaningful regions, most frequently to distinguish objects or regions of interest (foreground) from everything else (background). It is an essential step prior to the description, recognition or classification of an image or its constituents. There are two major approaches for segmentation – region based methods, in which similarities are detected, and boundary based methods, in which discontinuities (edges) are detected and linked to form boundaries around regions.

The segmentation approaches can be classified according to both the features and the technique used. The features include gray values (brightness), texture and gradient magnitudes. Segmentation techniques can be classified as either contextual or noncontextual. Noncontextual techniques ignore the relationships that exist between features in an image; pixels are simply grouped together on the basis of some global attribute, such as gray level. Contextual techniques additionally exploit the relationships between image features. Contextual techniques include:

region based techniques, such as region growing, where connected regions are found based on some similarity of the pixels within them; boundary based techniques, where edge based methods are used to delineate the boundaries between regions; and other methods, such as active contours and watershed segmentation [3].

In medical imaging, automated delineation of different image components is used to analyse anatomical structure and tissue types, spatial distribution of functions and activity, and pathological reasons. Segmentation can be used as initial step for visualisation and compression. Segmentation of an object can be achieved either by identifying all pixels belonging to the object or by locating those that form its boundary. The segmentation by identifying the pixels belonging to an object is based on attributes of pixels like intensity, texture etc., while locating boundary pixels involve image gradients which have high values at the edges [89].

In some medical imaging applications, the presence of various structures with different properties suggest the use of specifically designed sequence of multiple segmentation techniques. The initial steps can be fundamental techniques to reduce data and elaborate robust time consuming techniques can follow. The best choice of techniques and their order depends on the problem and computational resources.

This chapter describes the framework of segmentation techniques developed for PET and mammographic images, segmentation evaluation, algorithms used and results obtained.

4.2 Framework

The framework of segmentation technique developed explains widely used segmentation methods in medical imaging and theory of gabor annulus filtering, region growing and eccentricity.

4.2.1 Widely used segmentation methods with medical images

In medical imaging, segmentation is important for feature extraction, image measurements and display. There is no standard image segmentation technique that has produced satisfactory results for all imaging applications. The different assumptions about nature of analysed images lead to different algorithms. The image segmentation techniques can broadly be classified as region segmentation and edge segmentation methods. Region segmentation methods search for regions satisfying homogeneity criteria while edge segmentation methods look for edges between the regions with different characteristics.

In thresholding, a threshold is selected and image is divided into group of pixels having values less than the threshold and pixels with values greater than or equal to the threshold. Suppose we have an image $f(x,y)$ and the histogram of the image gives the information that the object and background pixels are grouped into two dominant modes. Let us select a threshold T to separate the modes. The thresholded image $g(x,y)$ is given as

$$g(x,y) = \begin{cases} 1 & \text{for } f(x,y) \geq T \\ 0 & \text{for } f(x,y) < T \end{cases} \quad (4.1)$$

If the image has more than two types of regions, it can be segmented by applying several individual thresholds or by using multithresholding techniques. Global thresholding even though simple and

computationally fast, fails when contrast between object and background is low or when the image is noisy or when background intensity varies significantly across the image.

Clustering algorithms partition the image into sets or clusters of pixels that have strong similarity in feature space. The basic operation is to examine each pixel and assign it to a cluster that best represent the value of its characteristic feature vector of interest.

Region growing assigns adjacent pixels or regions to the same segment if their pixel values are close enough, according to some preselected criteria of closeness. Region growing is found in medical image segmentation examples like segmenting ventricles on cardiac images, extraction of blood vessels on angiography data and extraction of brain surface.

Edge based algorithms find the object boundaries and segment regions enclosed by the boundaries. They operate using edge operators like Prewitt, Sobel or Roberts. Contour following and graph searching are other edge based segmentation methods widely used.

4.2.2 Gabor annulus filtering

The traditional Gabor wavelet filter is a complex plane wave restricted by a Gaussian envelope, and is defined as follows:

$$G(x, y) = \frac{1}{2\pi\sigma_x\sigma_y} e^{-\pi\left[\frac{(x-x_0)^2}{\sigma_x^2} + \frac{(y-y_0)^2}{\sigma_y^2}\right]} e^{i[2\pi f_0 x]} \quad (4.2)$$

The first exponent is an elliptical Gaussian, with standard deviation σ_x in the waveform direction, and σ_y in the perpendicular direction. The

second exponent is the complex plane wave with frequency f_0 in the x direction. (x_0, y_0) specify the centre coordinates of the filter in the spatial domain. The filter defined in the above equation can be treated as a ‘mother wavelet’, which can be scaled and rotated to produce a family of filters. When an input image is applied to these filters through convolution, they will produce a maximum response in areas of the image containing features or patterns which match the specific scale and orientation of these filters.

Gabor wavelet filters are a method of extracting the spatial location of underlying frequencies within an image. Each filter provides a maximal response in areas of an image where there is an underlying pattern or image feature with the same frequency characteristics as the filter, at the same scale and orientation. The ability of Gabor wavelets to respond strongly to more general image features based on underlying textures and frequencies is key to the design of the Gabor annulus (GA) technique.

Gabor wavelets have the calibre to identify image features and patterns at definite scales and orientations. This expertise is employed in GA approach to detect circular features. In this technique, the traditional Gabor filter is offset by a radius and encloses the origin. It is defined as

$$G(x, y) = \frac{1}{2\pi\sigma_0} e^{-\pi \left[\frac{(r-r_0)^2}{\sigma} \right]} e^{i[2\pi f_0(r-r_0)]} \quad (4.3)$$

$$\text{where } r = \sqrt{(x - x_0)^2 + (y - y_0)^2}$$

Here σ represents the standard deviation of the Gaussian envelope in the waveform direction. The envelope expands radially outwards from the

centre of the filter which is specified by coordinates (x_0, y_0) and r_0 denotes the radius of the ‘annulus’ shape.

The filter responds to circular image features made up of matching radial frequencies on their boundaries. The centre of the circular image feature is identified by finding the location where the filter response will be the strongest. The GA technique creates a family of filters at various scales which can be utilised to match circular image features at various sizes within the image. The filters are radial symmetric so that rotations need not be created at different orientations [101].

4.2.3 Region growing

Region growing can be considered both as region based image segmentation method and pixel based image segmentation method. The neighbouring pixels of initial ‘seed points’ are analysed to decide whether the pixel neighbours should be added to the region. Region growing approaches exploit the important fact that pixels which are close together have similar gray values [102]. In region growing, an initial set of small areas are iteratively merged according to similarity constraints.

Region growing is a bottom-up procedure that starts with “seed” pixels, and then grows regions by adding neighbouring pixels that have similar properties like brightness, colour, texture, gradient and geometric properties to the seed. Connectivity is used to define the pixels which are the neighbouring ones. We can specify a variance for the property; region growing stops when a pixel is encountered that is not within this variance. The seeds can be chosen interactively although automatic segmentation is preferable.

Starting with a particular seed pixel and letting this region grow completely before trying other seeds biases the segmentation in favor of the regions which are segmented first. This can have several undesirable effects: the current region dominates the growth process and ambiguities around the edges of adjacent regions may not be resolved correctly, different choices of seeds may give different segmentation results and problems can occur if the (arbitrarily chosen) seed point lies on an edge. One way to counter these problems is to scatter seed points randomly around the image and grow from several seed points simultaneously [3].

The steps involved in region growing are as follows:

- 1) Start by choosing an arbitrary seed pixel and compare it with neighboring pixels
- 2) Region is grown from the seed pixel by adding in neighboring pixels that are similar, increasing the size of the region
- 3) When the growth of one region stops we simply choose another seed pixel which does not yet belong to any region and start again.
- 4) The whole process is continued until all the pixels belong to some region [8].

The selection of seed points can affect segmentation results and different choices of seed points may produce different results [103].

Region growing techniques are generally better in noisy images where edges are extremely difficult to detect. They are particularly useful with images which have multi modal histograms.

4.2.4 Eccentricity

Eccentricity is one of the important image boundary descriptor. The major axis and minor axis are the two descriptors used to define eccentricity. The line segment connecting two extreme points that comprises diameter of the boundary is called major axis while the line perpendicular to major axis and of such length that a box passing through outer four point of intersection of the boundary with two axes encloses the boundary is minor axis. The ratio of major to minor axes is defined as eccentricity [8].

Eccentricity can be computed by principal axes method. The principal axes of a shape is defined as two segments of lines that cross each other perpendicularly through the centroid representing directions with zero cross correlation. The covariance matrix of the contour is given by

$$C = \begin{pmatrix} c_{xx} & c_{xy} \\ c_{yx} & c_{yy} \end{pmatrix} \quad (4.3)$$

The lengths of the two principal axes equal the eigen values λ_1 and λ_2 of the covariance matrix C. The eigen values are calculated as

$$\lambda_1 = \frac{1}{2} \left[c_{xx} + c_{yy} + \sqrt{(c_{xx} + c_{yy})^2 - 4(c_{xx}c_{yy} - c_{xy}^2)} \right] \quad (4.4)$$

$$\lambda_2 = \frac{1}{2} \left[c_{xx} + c_{yy} - \sqrt{(c_{xx} + c_{yy})^2 - 4(c_{xx}c_{yy} - c_{xy}^2)} \right]$$

The eccentricity is given as ratio of λ_2 to λ_1 . The value is between 0 and 1. If the eccentricity is 0 the shape is a circle and value 1 shows that the shape is a line segment [3].

Selection of a segmentation task for a particular goal is always difficult and sometimes combinations of different segmentation techniques are used to achieve a required segmentation. For every image processing technique it is important to have a proper evaluation. In the next section we will see the evaluation measures for segmentation.

4.3 Evaluation of segmentation techniques

The appraisal of segmentation can be subjective or objective. In subjective evaluation the quality of segmentation is decided by a viewer who uses his knowledge and experience for discretion. In objective measures, the quality is assessed in numeric values. The objective evaluation can be classified as supervised evaluation and unsupervised evaluation. The supervised evaluation methods evaluate segmentation algorithms by comparing the resulting segmented image against a manually segmented reference image, which is referred to as a gold standard or ground truth. The degree of similarity between the human and machine segmented images determines the quality of the segmented image. Unsupervised evaluation methods evaluate a segmented image based on how well it matches a broad set of characteristics of segmented images as desired by humans [104,105,106,107,108,109]. For evaluating proposed segmentation technique, we choose inter region contrast, intra region uniformity and combination of intra region and inter region disparity suggested by Levine and Nazif [107].

Inter region contrast is calculated from sum of contrasts of regions R_i balanced by their surface areas. The contrast of a region is calculated starting from contrasts with the regions which are conterminous to it. Let c_{ij}

be the contrast between two regions R_i and R_j having m_i and m_j as their mean gray levels respectively.

$$c_{ij} = \frac{|m_i - m_j|}{m_i + m_j} \quad (4.5)$$

The contrast of the region R_i is given as

$$c_i = \sum_{W_i} p_{ij} c_{ij} \quad (4.6)$$

where W_i denotes the indices of the regions adjacent to the region i and

$p_{ij} = \frac{l_{ij}}{l_i}$, the ratio of the length of the common boundary between R_i and R_j

to the perimeter of R_i . The inter region contrast is given as

$$C_{Inter} = \frac{\sum_{R_j} w_j c_j}{\sum_{R_i} w_i} \quad (4.7)$$

w_i is the weight associated to each region, and here it is taken as the area of the region [108].

The uniformity of a feature over a region is inversely proportional to the variance of the values of that feature evaluated at every pixel belonging to that region. A nil value for the variance requires all the pixels to have the exact same value for the feature, while a large variance would indicate a large spread from the mean of the feature value across the region. The intra region uniformity criterion suggested by Levine and Nazif [109] is defined by computing the sum of the normalized standard deviation of each region. Let $C(p)$ be the gray value of pixel p . The average gray level

value of a region R is $\bar{C}(R)$. Let S_i be a region, the average gray level value of the region is given as

$$\bar{C}(S_i) = \frac{1}{A_i} \sum_{p \in S_i} C(p) \quad (4.8)$$

where A_i is the number of pixels in the region S_i . The normalised gray level variance on the region S_i is given as:

$$\sigma^2(S_i) = 4 * \frac{\frac{1}{A_i} \sum_{p \in S_i} (C^2(p) - \bar{C}^2(S_i))}{\max_{p \in S_i} [C(p)] - \min_{p \in S_i} [C(p)]} \quad (4.9)$$

If the segmented image I_s is formed with N_s regions, the intra class uniformity is defined as

$$U_{Intra} = 1 - \sum_{i=1}^{N_s} \sigma^2(S_i) \quad (4.10)$$

Intra inter region disparity is another measure considered for evaluation. It combines with the inter region dissimilarity and inter region disparity. This is represented as follows:

$$D_{Intra-Inter} = \frac{1 + \frac{1}{C_{N_s}^2} \sum_{i,j=1;i \neq j}^{N_s} (|\bar{C}(S_i) - \bar{C}(S_j)| / 512 - 4/255^2 N_s) \sum_{i=1}^{N_s} \sigma^2(S_i)}{2} \quad (4.11)$$

where $C_{N_s}^2$ is number of combinations of two regions among N_s . Intra region disparity is computed by the normalized standard deviation of gray levels in each region. The inter regions disparity computes the dissimilarity of the average gray level of two regions in the segmentation result [110].

4.4 Segmentation approach for ROI separation in PET images

The proposed method is a two staged segmentation technique having GA filtering as first stage and region growing with automatic seed selection as the second stage. The original image first undergoes preprocessing in the form of morphological operations and image enhancement. The image enhancement is done by a modified type of high boost filtering as explained in section 3. The high pass filtered image which is obtained from the application of SWT and detail modulus on the image is added to the original image for enhancing it. The enhanced image is subjected to segmentation. The block diagram for the process is given in Fig 4.1.

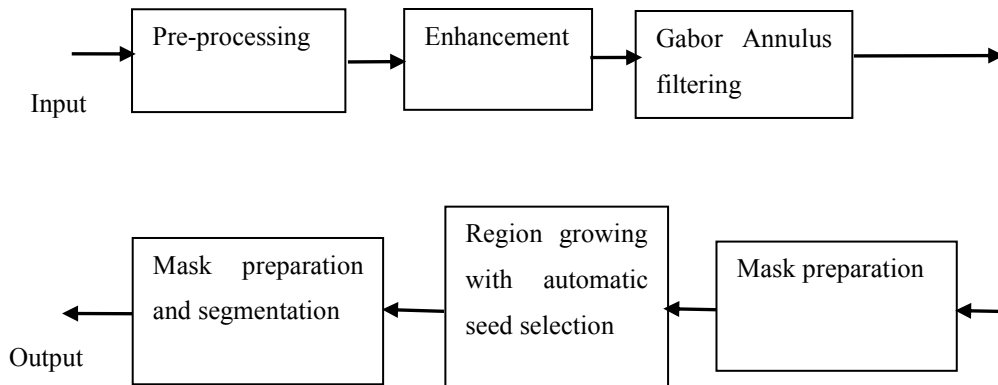


Fig. 4.1 Block diagram of proposed method

The proposed method consists of three stages of segmentation. The enhanced image is the input to the first stage i.e., GA filtering. The lesions and most of the prominent organs like brain, heart, etc. are almost circular in shape when considering axial slices. The kernel size, standard deviation of Gaussian envelope, wavelength and radius of annulus are determined

experimentally. The filtered image is subjected to dilation and edge detection using Laplacian of Gaussian operator (LoG) and operated morphologically upon and boundary is drawn to create the mask for segmentation.

Another level of segmentation is needed to reduce under-segmentation and we propose region growing with automatic seed selection. The region is iteratively grown by comparing all unallocated neighbouring pixels to the region. The difference between pixel intensity value and region mean is the measure of similarity chosen. The pixel with smallest difference measured is allocated to the respective region. The process stops when the difference is greater than a particular threshold.

For automatic seed selection, the image is divided into blocks of size 5 x 5 and standard deviation of each block is found. The block with largest standard deviation is identified and pixel with maximum value is selected as initial seed point. Threshold determination is another important aspect that has to be taken care of in region growing. Here we use the technique of finding largest pixel values along the column of the image. The average of the values thus obtained is found and rounded off. Half of this value serves as threshold in this case. The mask for second level of segmentation is obtained as a result of performing morphological operations on the result of region growing.

The flow chart provided in the next page in Fig 4.2 gives a clear understanding of the proposed algorithm.

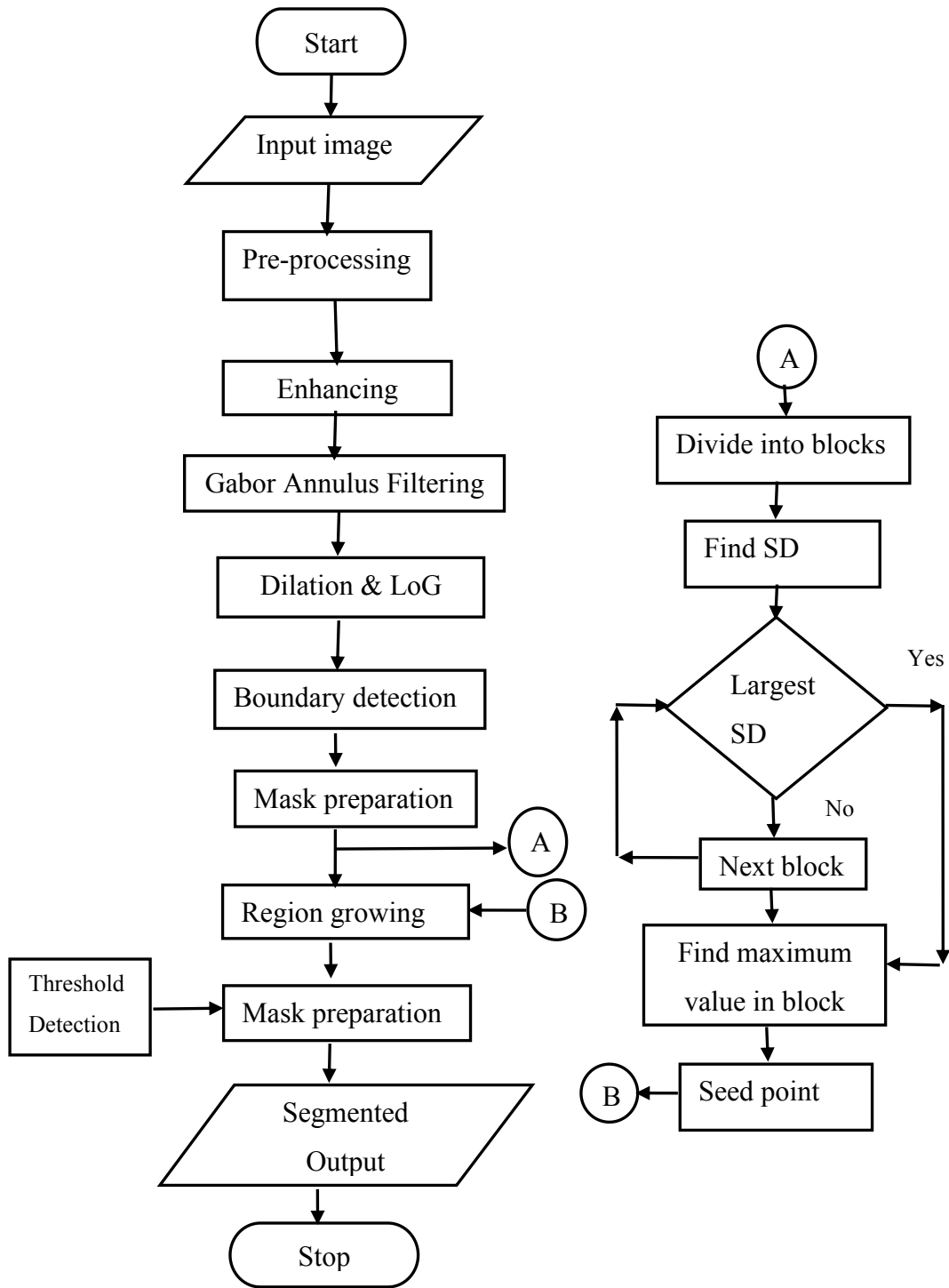


Fig. 4.2 Illustration for proposed segmentation algorithm

4.4.1 Experimental determination of GA filter parameters

The choice of filter parameters is crucial in deciding the output of any filter. The various parameters used in GA filtering viz., wavelength (λ), kernel size (S), radius of GA (r) and Gaussian deviation (σ) are determined experimentally. Fig 4.3 shows the segmentation results obtained for different values of GA filter parameters.

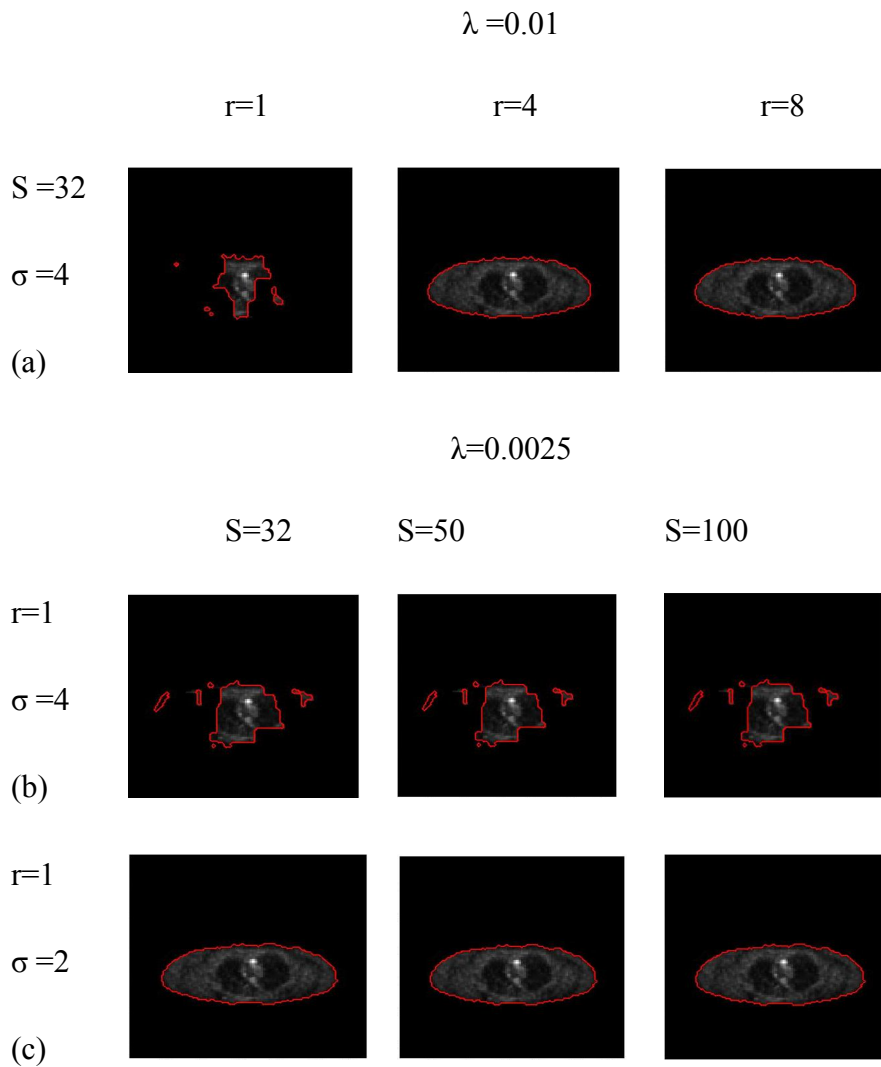


Fig. 4.3 Segmented images for various GA parameters

The segmented area is minimum for the choice of $r=1$ and $\sigma=4$. For other values it can be observed from the figure that the segmented region will have more area than the background region. Here since our aim is to retain the region having lesion as ROI and separate the rest as BG, the choice of r and σ is justified. Table 4.1 depicts the effect of variation in λ on segmented area in terms of number of pixels and mean SSIM (MSSIM), which clearly shows that fixing the value of λ as 0.0025, offers better MSSIM. The kernel size is chosen as 32 because an optimum segmentation both in objective and subjective terms could be obtained for this value which as seen from Fig 4.3(b)

Table 4.1: Effect of various λ on segmented area and MSSIM

λ	Segmented Area	MSSIM
0.01	947	0.9594
0.0025	1777	0.9601
0.001	3890	0.9570

The kernel size S limits the area under consideration, rather than considering the image as a whole. The deviation σ decides the support of basis size of image region being analysed. The wavelength λ decides the frequency being looked in the image. Using the selected values for various parameters, GA filtering is carried out in stage1 segmentation.

4.4.2 Unsupervised evaluation and results

Each image in this database is of size 128 x 128 x 375. SUV are widely used to measure FDG uptake. The more reliable SUV normalisation of FDG uptake for the body surface area is used here [100]. FDG, a short lived radio pharmaceutical, is used in oncology to assess glucose

metabolism activity in human body. To reduce the complexity of computation each of the axial slices is taken one by one and processed. The image after initial preprocessing is subjected to GA filtering with the experimentally chosen parameters. The filtered output of an image with a single lesion is shown in Fig 4.4 in which circle encompasses the lesion.

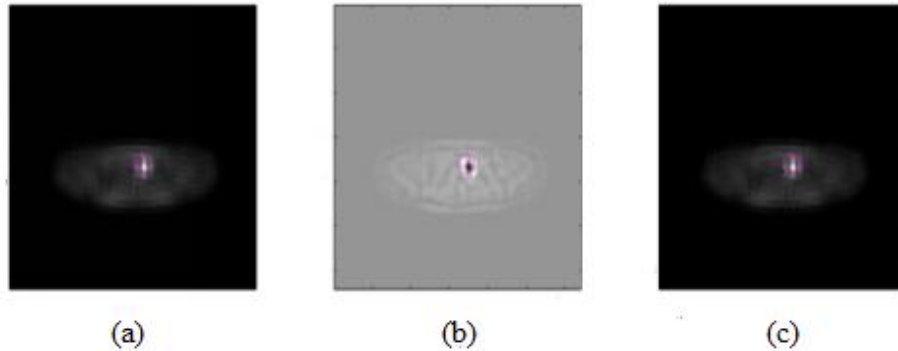


Fig. 4.4 GA filtered output of an image with a single lesion (a) Real part (b) Imaginary part (c) Absolute of complex image

Fig 4.5 gives the GA filtered output of the image without any lesion. The real part, imaginary part and absolute of the output image are shown separately.

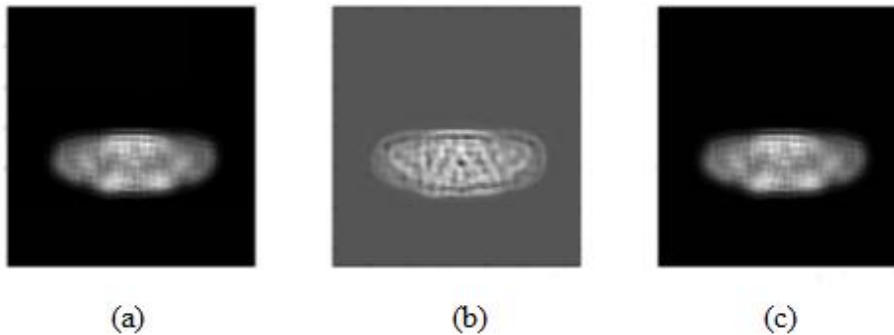


Fig. 4.5 GA filtered output of an image without any lesion (a) Real part (b) Imaginary part (c) Absolute of complex image

After filtering, the image is dilated and morphologically operated

upon using structuring element whose choice depending on the lesion shape and size as specified in the database. The database is based on lymphoma which affects lymph nodes and they are circular in shape and smallest lesion is of radius 1. So to make sure that the lesions are not missed radius is taken as 4. The result of these operations is given in Fig 4.6 and Fig 4.7.

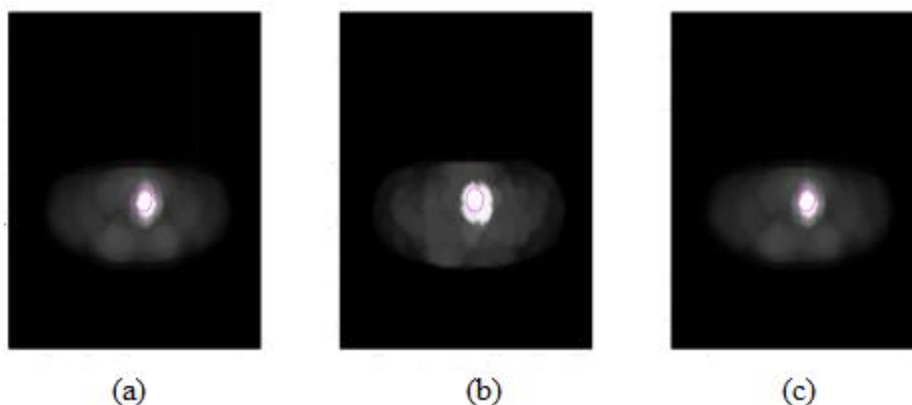


Fig. 4.6 GA filtered and dilated output of an image with a single lesion (a) Real part (b) Imaginary part (c) Absolute of complex image

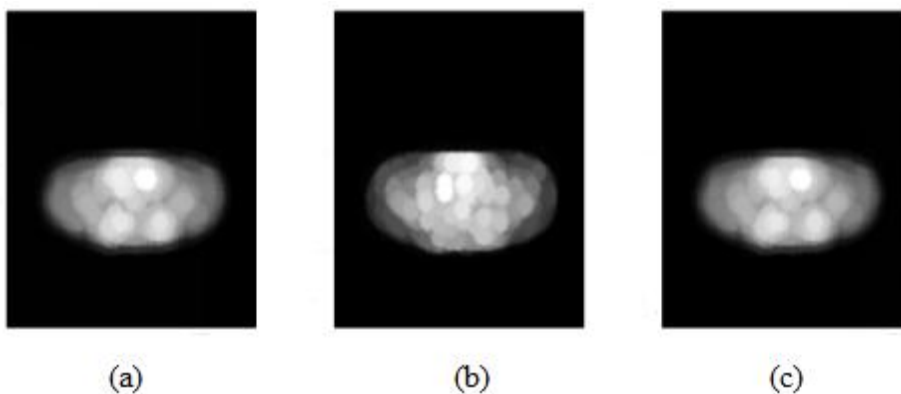


Fig. 4.7 GA filtered and dilated output of an image with no lesion (a) Real part (b) Imaginary part (c) Absolute of complex image

The segmentation is appraised using three unsupervised evaluation criteria viz., inter region contrast (inter), intra region uniformity (intra) and

combination of intra region and inter region disparity (intra- inter).

This segmented output is fed as input to region growing stage. The result of this stage on an image with a single lesion is given in Fig 4.8.

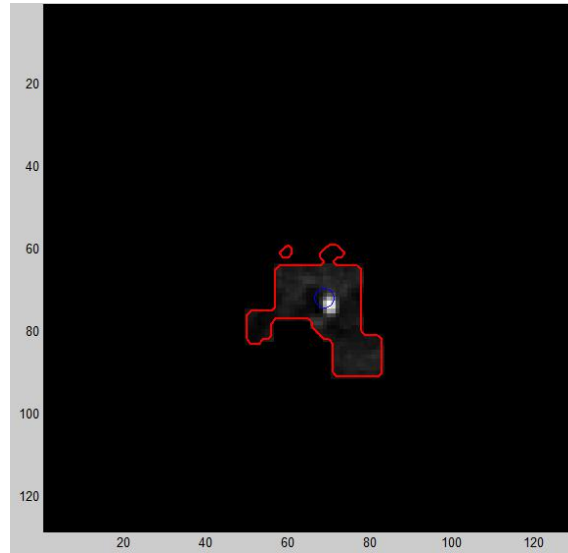


Fig. 4.8 Region growing output

This stage of segmentation gives better segmentation than single level segmentation. After this level, the three criteria are calculated.

The result of segmentation of an image having 2 lesions is shown in Fig 4.9. The two lesions present in the image are indicated by the white arrows. Fig 4.9(b) displays segmentation result after GA filtering and subsequent segmentation. Fig 4.9(c) shows the segmentation result after region growing on the result of first stage which provides a better segmentation in comparison with the first.

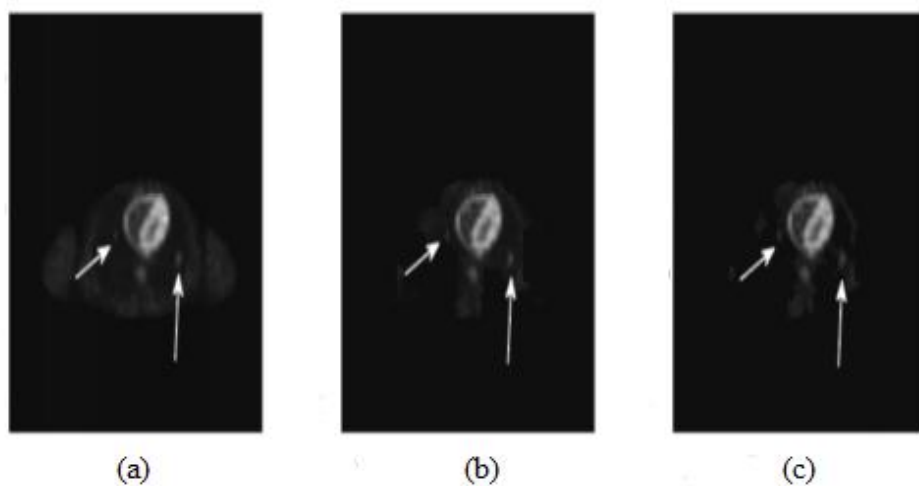


Fig. 4.9 Segmentation of an image with two lesions (a) Original preprocessed image (b) Segmented result after stage 1 (c) Segmented image after stage 2

Fig 4.10 shows the result of segmentation on another image having a small lesion. Only partial success is achieved in this case.

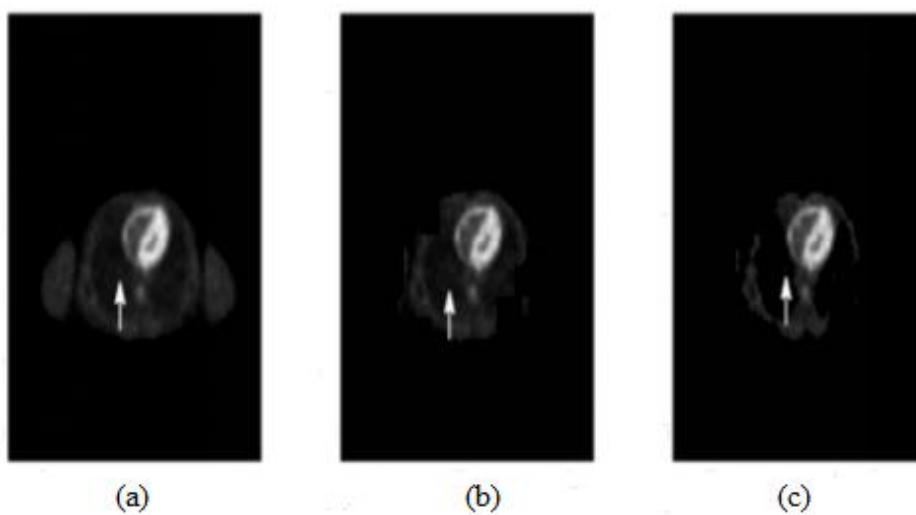


Fig. 4.10 Segmentation of an image with single lesion (a) Original preprocessed image (b) Segmented result after stage 1 (c) Segmented image after stage 2

Fig 4.11 shows the result of segmentation on an image having no lesions.

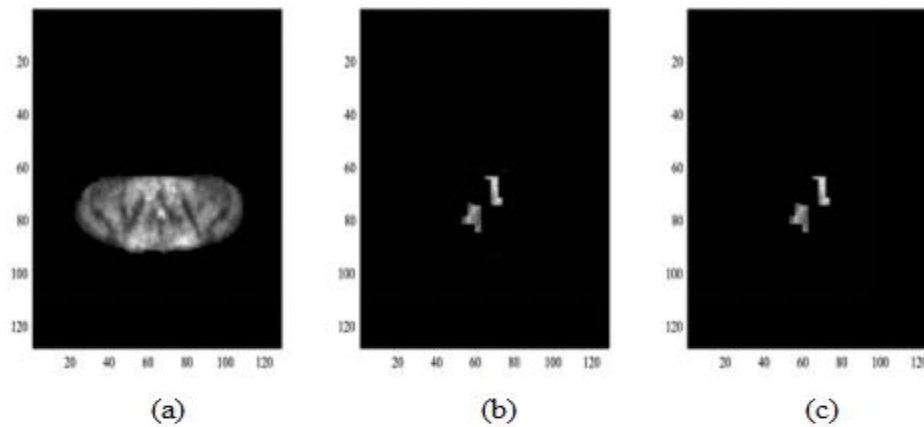


Fig. 4.11 Segmentation of an image without any lesion (a) Original preprocessed image (b) Segmented result after stage 1 (c) Segmented image after stage 2

The masks generated for the two segmentation stage are compared for the images with and without lesions. The result of comparison are given in Fig 4.12 and Fig 4.13

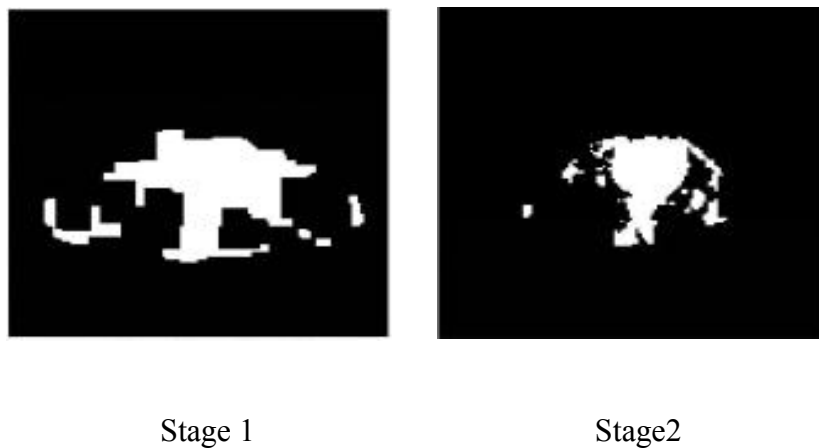


Fig. 4.12 Mask comparison at two stages of segmentation : 2 lesions

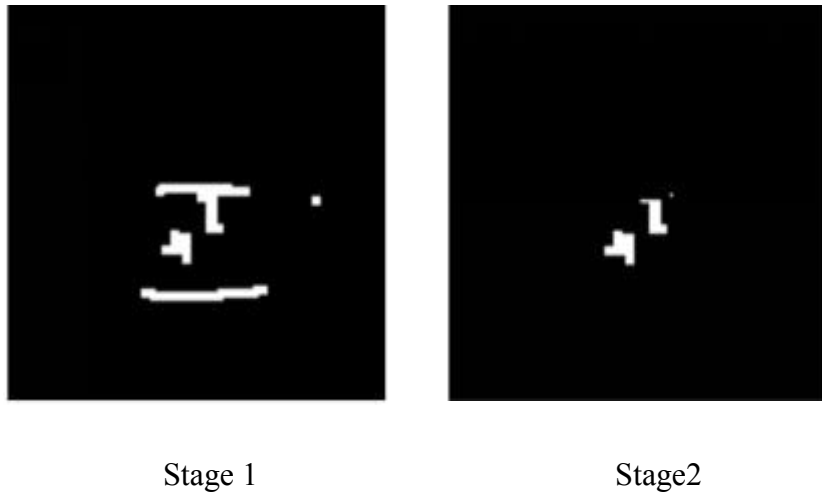


Fig. 4.13 Mask comparison at two stages of segmentation : no lesion

From the picture it is clear that considerable segmented area is reduced after the second stage of segmentation. The segmented area is less for image without any lesions when compared with the images having lesions.

The subjective evaluation is performed on 250 axial slices from 39 images for both level of segmentation. The average values for inter, intra and intrainter are calculated and tabulated in Table 4.2. It is observed that inter value after second level of segmentation is greater which clearly means a better segmentation after the region growing phase. Intra value is slightly better after first level of segmentation while intrainter value shows improved performance after second level of segmentation. For a better segmentation inter value should be closer to 1 while intra value should be less. Higher intrainter value indicates that segmentation quality is better.

Table 4.2: Performance measures for 2 stages of segmentation

Appraisal Norms	Segmentation Stage1	Segmentation Stage 2
Inter C_{Inter}	0.8477	0.8951
Intra U_{Intra}	0.0419	0.0444
Intra Inter $D_{Intra-Inter}$	0.5102	0.5230

Out of the 250 slices from different images considered for evaluation, the lesions were segmented correctly in 234 cases. In 14 slices, the lesions were missed while in two we could partly get lesions in the segmented regions. The partially detected cases have lesions in the first stage and partially lost them in the second stage of segmentation. After the first stage the lesions were missed in 10 slices. In the database examined here the lesions are spread out in blood pool, lungs, liver and spleen. The database consists of 2 categories of images - images with 5 lesions (MM_5) and images with 10 lesions (MM_10).

Table 4.3 shows the number of lesions detected from different locations in comparison to the actually present ones. The over all detection rate is 97.54% for blood pool lesions, 75.47% for lungs lesions and 100% for both liver and spleen lesions. The sensitivity of the proposed method is less for lungs lesions while compared to lesions in other locations. This may be due to the fact that the brightness of the lung lesions is comparable to other structures in lungs.

Table 4.3 Comparison of number of lesions detected in segmented images

Lesion Location	No. of Lesions Considered			No. of Lesions Segmented		
	MM_5	MM_10	Total	MM_5	MM_10	Total
Blood pool	73	49	122	71	48	119
Lungs	10	43	53	8	32	40
Liver	3	50	53	3	50	53
Spleen	1	21	22	1	21	22

The area of the segmented image in pixels is calculated after first and second stages of the proposed method. An average decrease of 40% in area is recorded in the comparison of segmented results after two stages. A maximum decrease of 73.46% is obtained while the minimum decrease in area obtained is 10.54%. Thus with this method under segmentation problem that existed with the single stage segmentation could be solved.

4.4.3 Comparison using CREASEG software

CREASEG is an open source software in MATLAB for the evaluation of the performance of different algorithms in the context of 2D image segmentation. Using a partial differential equation based method and solving the partial differential equation by a numerical scheme, one can segment the image. This technique is used in level set segmentation. Curve propagation is a popular technique in this category, with numerous

applications to object extraction, object tracking, stereo reconstruction, etc. The central idea is to evolve an initial curve towards the lowest potential of a cost function, where its definition reflects the task to be addressed.

The central idea is to represent the evolving contour using a signed function whose zero corresponds to the actual contour. According to the motion equation of the contour, one can easily derive a similar flow for the implicit surface that when applied to the zero level will reflect the propagation of the contour. Depending on the implementation or modeling issues, the level set interface may be allowed to evolve either on the whole domain at each iteration (allowing to develop new contours far from the zero level set) or only on a small region around its zero level set (region called narrow band).

The six algorithms compared here are Caselles - contour based approach, Chan & Vese - region approach, Li , Lankton - localised region based approach, Bernard - parametrised approach and Shi - discrete approximation. These algorithms are briefed in the subsequent paragraphs.

- (i) **Caselles method:** In Caselles method the gradient of the image is used to compute the force function. The curve will be driven to regions with high gradient. Any type of regularisation is not needed for this method as regularisation is intrinsic. For this algorithm we have propagation term as specific parameter and it act as force that pushes the contour inward or outward.
- (ii) **Chan & Vese method:** Chan & Vese algorithm tends to separate the image into two homogeneous regions according to their mean value. This method is sensitive to initialisation. Here the curvature

term λ is a specific term and it weighs the influence of regularisation.

- (iii) **Li algorithm:** Because of the localization introduced, Li algorithm is able to segment inhomogeneous objects. This algorithm segments the whole image. There are three specified parameters for this algorithm. They are curvature term, which weighs the influence of regularisation of contour, level regularisation term which weighs regularisation of shape and variance of the gaussian kernel.
- (iv) **Lankton method:** The feature term is computed locally in Lankton method. This property allows the algorithm to segment non-homogeneous objects. The method is sensitive to initialization. For Lankton method we have four specific parameter, viz., feature, neighbourhood, curvature term and radius.
- (v) **Bernard algorithm:** The algorithm computes the level set evolution on the whole image. So new contours could emerge far from the initialization. This algorithm is a region-based method and tries to separate the image into two homogeneous regions (according to their mean value). The specific parameter is scale factor which allows the selection of degree of smoothness of the contour.
- (vi) **Shi method:** This method is an approximation of level set based curve evolution. It is a very fast method and evolves only on the narrow band. The specific parameters in this case are variance of gaussian filter, size of the gaussian filter, number of iterations in regularisation cycle and number of iterations in data dependent cycle [111].

CREASEG software is mainly used for the comparison of visual and supervised evaluation parameters. Here we need reference image i.e., expected segmentation for comparison. We have used free hand initial contour for all the six methods in CREASEG. All these methods need some input from the user while the developed method is a fully automated one. Using the six methods described in the above paragraph the images are segmented and are compared and ranked for under segmentation. Lankton is the best among them as it has low under segmentation while Bernard is worst and has high under segmentation.

The parameters like dice coefficient, PSNR, Hausdorff distance and mean sum of square distance can also be compared. The dice coefficient is defined as

$$Dice = \frac{2(A \cap B)}{A + B} \quad (4.12)$$

where A and B are the reference mask region and the result mask region of an algorithm. Hausdorff distance is defined as

$$Hausdorff = \max(D_1(A, B), D_1(B, A)) \quad (4.13)$$

where A and B are the reference contour and the result contour of an algorithm and

$$D_1(A, B) = \max_{x \in A} (\min_{y \in B} (\|x - y\|)) \quad (4.14)$$

Mean sum of square distance (MSSD) is another measure of similarity criteria and can be defined as

$$MSSD = \frac{1}{N} \sum_{n=1}^N D_2^2(A, B(x_n)) \quad (4.15)$$

where A and B are the reference contour and the result contour of an algorithm, N is the size of the result contour and

$$D_2(A, B(x)) = \min_{y \in A} (\|y - x\|) \quad (4.16)$$

The evaluation parameters are calculated for 87 images. The graphs comparing average values of dice coefficient, PSNR, Hausdorff distance and MSSD of proposed method with the other six algorithms are shown in Fig 4.14(a-d).

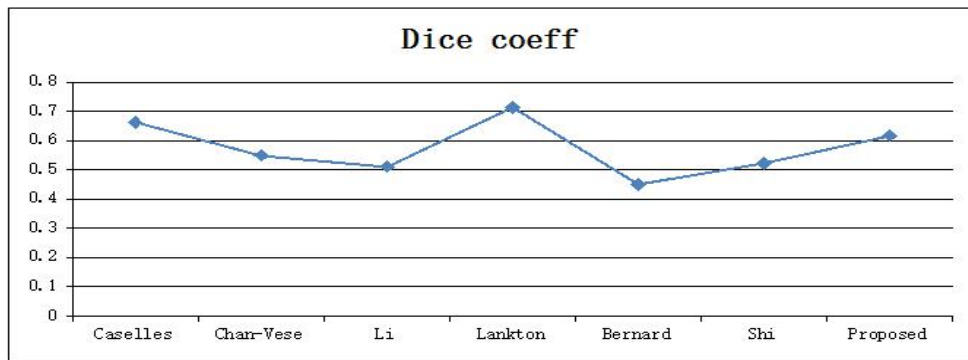


Fig. 4.14(a) Comparison of dice coefficient

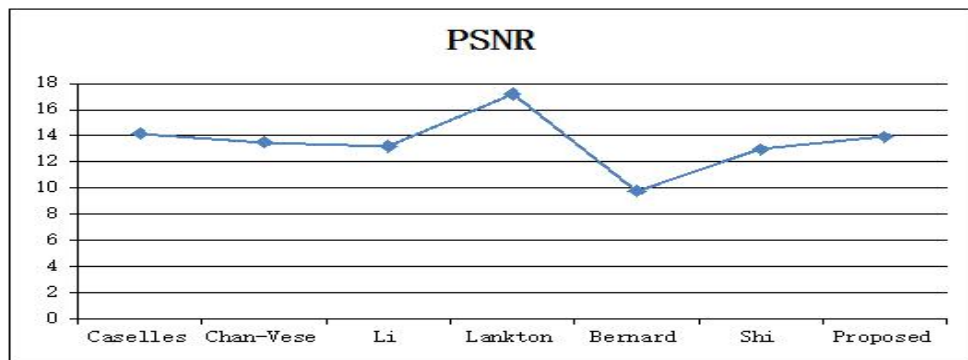


Fig. 4.14(b) Comparison of PSNR

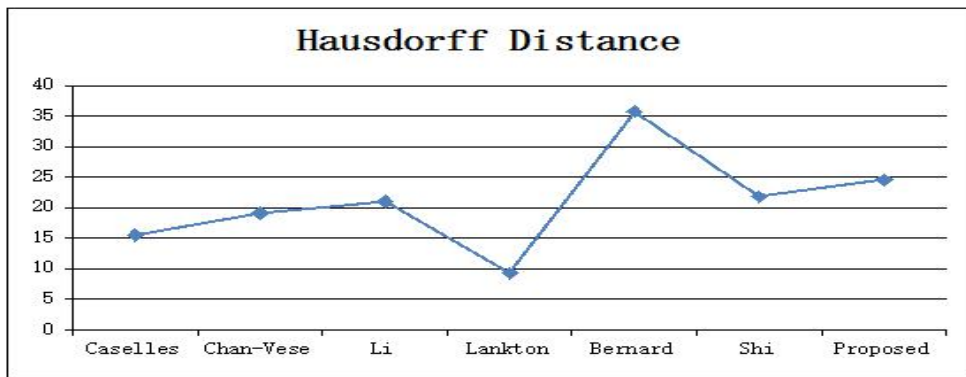


Fig. 4.14(c) Comparison of Hausdorff distance

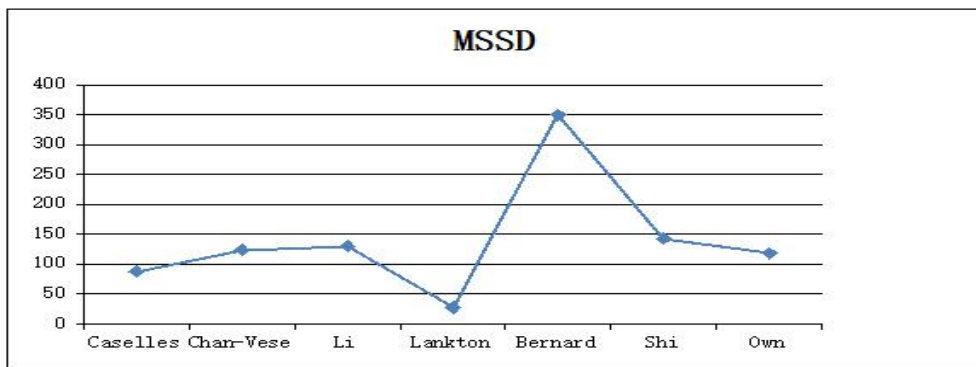


Fig. 4.14(d) Comparison of MSSD

The algorithms when ranked according to the parameters mentioned above are given in the Table 4.4. A consolidated view regarding the proposed algorithm effectiveness can be observed by a glance on the above mentioned table. Dice coefficient and PSNR should be maximum for a good segmentation algorithm while Hausdorff distance and MSSD should be minimum.

Table 4.4 Algorithms ranked acc. to Dice, PSNR, Hausdorff and MSSD

Algorithm	Dice	PSNR	Hausdorff	MSSD
Caselles	2	2	2	2
Chan Vese	4	4	3	4
Li	6	5	4	5
Lankton	1	1	1	1
Bernard	7	7	7	7
Shi	5	6	5	6
Proposed	3	3	6	3

The proposed algorithm ranks 3 in parameters except Hausdorff distance. In case of ranking according to under segmentation, the proposed method ranks the second. The lesion detection rate of the proposed method is same as that of Lankton algorithm which is 95.4% when considering 87 images. The main advantage of the proposed method is that it does not require any sort of input from the user.

4.5 Augmentation of developed approach to X-ray images

The method proposed is augmented for segmentation of mammographic images by using eccentricity for selecting ROI. In this method the mammographic region alone is segmented out. For this, the image is divided into blocks of size 128 x 128 pixels, then each block is enhanced using SWT, modulus maxima and high boost filtering technique as suggested in section 3.4.2 and contrast difference (C_{Diff}) between original

and processed image blocks are found out. The blocks that lie within the range specified by mean and standard deviation of C_{Diff} is retained while the rest are discarded. The lower range is the absolute value of the difference between mean and standard deviation of C_{Diff} and upper range is the absolute of sum of mean and four times the standard deviation of C_{Diff} .

Eccentricity is a shape descriptor which gives the amount of elongation in the shapes. The eccentricity of the different regions of resulting image is determined. The regions having eccentricity between 0.5 and 1 are separated. Using the mask prepared from the above result the segmented image is obtained. But the resultant image contains labels in the mammogram. The widely employed method of wielding the area of the region is applied so as to remove the labels. The region with largest area gives breast region from the image. The regions having the above said eccentricity range and largest area gives us the breast region in the mammogram which can be used as ROI for further processing.

The algorithm of the proposed method is given as follows:

Step1: Select the image of interest.

Step2: Perform SWT on the image.

Step3: Divide the image into block of size 128 x 128.

Step4: Enhance the image in the block and find contrast.

Step5: Find the contrast difference between the original and enhanced image.

Step6: Find the lower and upper range for pixels in the block.

Step7: Check whether the block lie within the range specified.

Step8: If yes, check eccentricity of image areas, if it is between 0.5 and 1, retain those image parts. Else discard the block.

Step9: Prepare mask according to the retained image areas.

Step10: Obtain the segmented image.

4.5.1 Results and Discussion

The proposed method is applied on normal images as well as images containing various types of abnormalities. The results of segmentation for various types of normal and abnormal mammogram images are shown in Fig 4.15. We can understand from visual examination that the proposed method performs well on mammographic images.

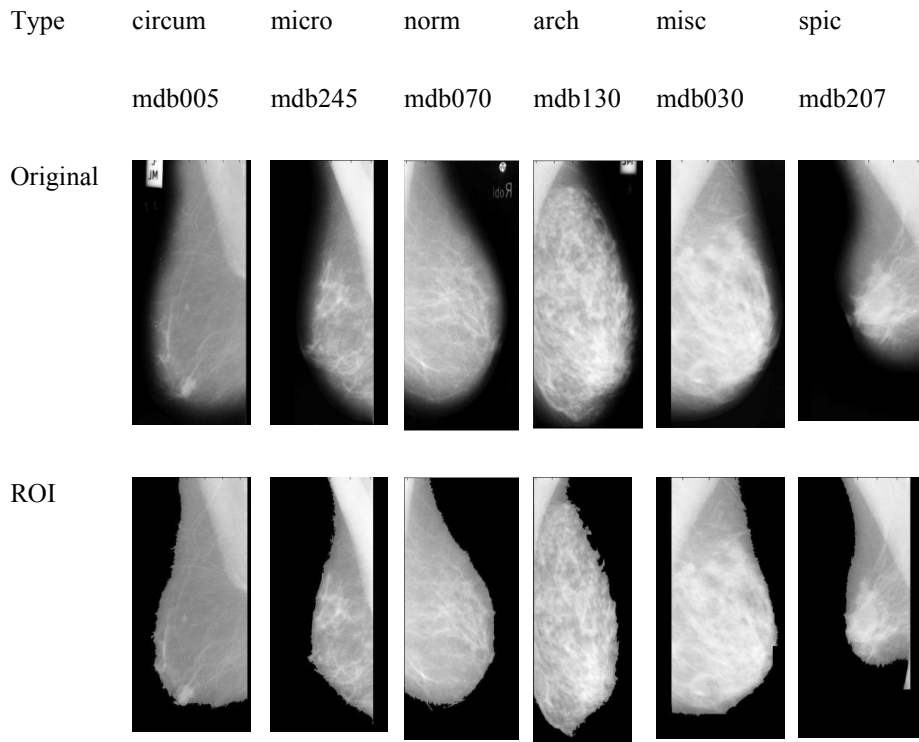


Fig. 4.15 Original and ROI segmented mammograms :Different abnormalities

The plots of average inter class contrast, intra class uniformity and intra inter class disparity against different types of images are shown in Fig 4.16.

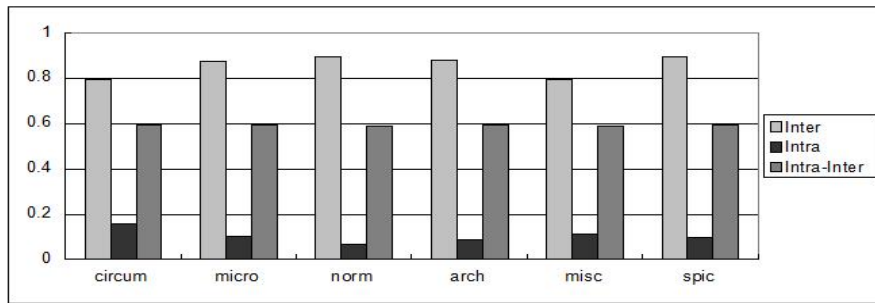


Fig. 4.16 Plot of performance measures

The average value of performance measures for each type of image in the database is calculated and the results are tabulated in Table 4.5 which clearly shows a good segmentation of mammographic images. The inter value is highest and intra value is lowest for normal images while intra inter value is almost same for all the types of images.

Table 4.5 Segmentation evaluation

Type of Abnormality	Performance Measures		
	C_{Inter}	U_{Intra}	$D_{Intra-Inter}$
Circumscribed masses	0.7968	0.1577	0.5938
Microcalcification	0.8751	0.1006	0.5918
Normal	0.8980	0.0664	0.5911
Architectural Distortion	0.8796	0.0893	0.5940
Miscellaneous	0.7940	0.1104	0.5889
Spiculated masses	0.8968	0.0989	0.5961

This work can be considered as an extension of enhancement and

hence it can reduce the number of steps in the processing of mammographic images.

4.6 Conclusion

The two stage segmentation proposed for PET images here exploits the concepts of edge based and region based segmentation effectively. GA filtering and region growing techniques form the backbone of the proposed method. The system is evaluated using three validation criteria viz. Inter region contrast, intra region uniformity and combination of intra region and inter region disparity. Another evaluation is done using CREASEG software. The successful lesion capture rate achieved using this technique is 93.6% when 250 slices are considered. The rate of partial success obtained is 0.8% while the failure rate acquired is 5.6%. The proposed method can be helpful in finding region of interest automatically in PET images.

Eccentricity and contrast difference are exploited to effect segmentation of mammographic images. The segmented image is evaluated using unsupervised evaluation parameters namely, Levine Nazif's inter region contrast, intra region uniformity and combination of intra region and inter region disparity.

This chapter deals with the segmentation of ROI in order to do ROI based compression. The segmentation technique make use of the concepts of GA and region growing. The developed method is evaluated objectively using various measures. The next chapter describes the compression techniques newly envisaged.

CHAPTER 5

COMPRESSION TECHNIQUES

5.1 Introduction

Teleradiology is a telemedicine application which involves transferring of large amount of multimedia data incorporating demographic and other patient information from one site to another. In this context we need to know how to compress large volume of data to allow images to be sent more economically and quickly followed by reconstruction at receiving end for viewing and interpretation. The digital images require large amounts of storage depending upon the resolution and digitization. Images are compressed to reduce the file size for efficient storage and transmission.

Compression techniques generally attempt to achieve a compromise between two undesirable outcomes: potentially deleting crucial information and insufficient reduction in file size. Compression and decompression techniques should not introduce error or artifacts. Compression techniques can be lossless or lossy. Performance and cost are the two factors that help to choose lossy or lossless type of compression. High performance compression requires more storage while lossy compression is acceptable at places where loss of data can be tolerated [89].

Image compression is a key issue to be addressed in the area of transmission and storage of images. The storage and transmission of large volumes of image data is a challenging task owing to limited storage space and bandwidth. With the emerging technologies, there are promises of

unlimited bandwidth. But the need and availability for images outgrow the increase in network capacity. The high costs involved in providing large bandwidth and huge storage space further necessitates the need for image compression.

5.2 Basics of compression

Image compression means reducing size of image without degrading image quality. In most of the images, the neighboring pixels are correlated, and image contains redundant information. Compression finds a less correlated representation of the image. Image compression reduces redundancy and irrelevancy. Redundancy reduction removes duplication from image, and irrelevancy reduction omits parts of the signal that will not be noticed by HVS.

The different types of redundancies are coding and inter pixel redundancies. Coding redundancy occurs when probabilities of occurrence of a symbol are not properly exploited. Inter pixel redundancies are of two types - spatial and temporal. This is due to correlation among pixels. Spatial redundancy occurs due to correlation among neighborhood pixels while temporal redundancy is due to correlation between successive frames. Image compression reduces number of bits needed to represent the image.

5.2.1 Compression models

A general image compression system consists of two distinct structural blocks, encoder and decoder as shown in Fig 5.1. An input image $f(x,y)$ is fed into the encoder, which creates a set of symbols from input data. After transmission over the channel the encoded representation is fed to the decoder, where a reconstructed output image $\hat{f}(x,y)$ is generated. If

$f(x, y) = \hat{f}(x, y)$, the system is error free. The encoder consists of a source encoder and a channel encoder which removes redundancies in the input images and a channel encoder which increases noise immunity of source encoder's output.

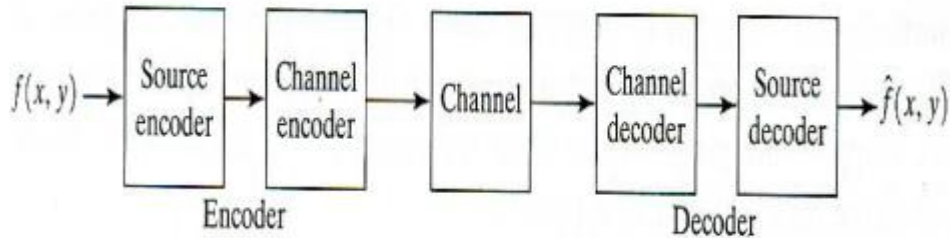


Fig. 5.1 Image compression model

The decoder includes a channel decoder followed by a source decoder. If the channel is noise free channel encoder and decoder can be omitted, which unfortunately is only an ideal case [8].

5.2.1.1 Source encoder and decoder

The source encoder is responsible for removing any type of redundancy in the input image. The specific application and associated fidelity requirements dictate the best encoding approach suited for any given situation. Fig 5.2 shows the block diagrams of encoder and decoder. The first stage of an encoder is a mapper that transforms input data into a format usually of non visual type to reduce inter pixel redundancies in the image. It is a reversible operation and need not strictly reduce the amount of data needed to represent the image. Run length encoding is one such example. The mapper transforms the image into an array of coefficients making accessing of inter pixel redundancies more accessible for compression at later stages.

The quantizer reduces the accuracy of mapper's output in accordance with some preestablished fidelity criteria. In this stage psychovisual redundancies are reduced. This is an irreversible process and it should be omitted if an error free compression is desired.

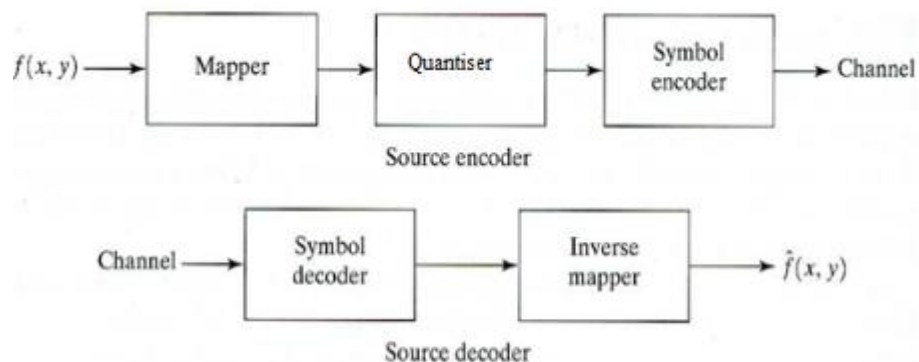


Fig. 5.2 Encoder and decoder

The last stage is a symbol encoder which creates a fixed or variable length code to represent quantizer's output and maps the output with code. In variable length coding shorter codes are used to represent frequently occurring values in the quantized data set while less frequent ones are represented with longer codes. Thus it reduces coding redundancy. All the three operations are not necessarily included in every compression system. In some compression techniques these blocks are also merged.

The decoder has two components - symbol decoder and inverse mapper. They perform the reverse operations of symbol encoder and mapper [8].

5.2.1.2 Channel encoder and decoder

The channel encoding and decoding plays an important role when the channel is noisy or prone to error. The impact of channel noise is reduced by adding controlled form of redundancy into the source encoded

data. The source encoder reduces redundancy while the channel encoder adds controlled redundancy sacrificing some amount of compression obtained. One of the mostly used channel coding encoding techniques is Hamming codes.

5.2.2 Image compression techniques

Among the error free compression techniques we have Huffman coding and Arithmetic coding which utilizes variable length coding to reduce coding redundancy. Huffman code is an instantaneous uniquely decodable block code which is highly acceptable because of its simplicity and speed. Arithmetic coding generates non block codes which have no one to one correspondence with the source symbols. An entire sequence of symbols is assigned a single codeword. This can offer better compression than Huffman coding because its code words can have effectively non integer bit lengths, whereas code words in Huffman coding can only have an integer number of bits.

Lempel Ziv Welch (LZW) coding attempts to reduce inter pixel redundancies and are integrated into many file formats like tagged image file format (TIFF), graphical interchange format (GIF) and portable document format (PDF). LZW assigns fixed length code words to variable length sequence of symbols and requires no a priori knowledge of probability of occurrence of the symbols. A unique feature of LZW coding is the code book or dictionary is created while data is being encoded.

Bit plane coding is another technique which reduces inter pixel redundancies and processes image's bit planes individually. Here the image is decomposed at multi level into a series of binary images and each binary image is compressed using well known binary compression

techniques. Gray coding the bit planes reduces the complexity of binary encoding.

For binary image compression we have constant area coding, one and two dimensional run length coding and contour tracing and coding. In constant area coding, special code words are used to identify large areas of contiguous '1's and '0's while in one dimensional run length coding each row is represented by sequence of lengths that describe successive runs of white and black pixels. Two dimensional run length coding is an extension of one dimensional run length coding and better known as relative address coding. In contour tracing and coding, each contour is represented by a set of boundary points or a single boundary points and set of directionals.

Predictive coding and transform coding are also prominent areas in image compression. Predictive coding predicts pixel value and tries to reduce the prediction error while the image is transformed to another domain to suit compression in transform coding [8].

The usefulness of image compression depends upon the quality of the processed images. Quality is an attribute which can have different definition and interpretation depending upon the use to which the images are put. A processed image visually indistinguishable from the original is referred to as perceptually lossless or transparent quality image [89]. In the next section we can have overview of evaluation measures which reflect the quality of the compressed and then subsequently decompressed image.

5.3 Wavelet and related concepts

Morlet and Grossman introduced the idea of wavelets as a family of functions constructed by using translation and dilation of single function, called mother wavelets, for analysis of nonstationary signals. Wavelets are

a mathematical tool that can be used to extract information from many different kinds of data, including audio signals and images. Wavelet analysis create a common link between mathematicians, physicists, and electrical engineers with applications as diverse as wave propagation, data compression, image processing, pattern recognition, computer graphics and other medical image technologies. Sets of wavelets are generally needed to analyze data fully [112]. It is better to obtain a correlation between time and frequency domains of a signal when we analyse non stationary signals. The wavelet transform provides localisation in both the time domain and frequency domain. The translations of the wavelet basis function give localisation in time domain while the localisation in frequency domain is provided by dilations of basis functions. The main objective of wavelet transform is to define the powerful wavelet basis functions and find efficient methods for their computation.

Even though, the Fourier transform is a useful tool to analyze the frequency components of the signal, it cannot give the instant at which a particular frequency rises. Short time Fourier transform (STFT) uses a sliding window to find spectrogram, which gives the information of both time and frequency. But the length of window limits the resolution in frequency [113]. Wavelet transform provides a solution to this problem by changing the width of wavelet function with each spectral component. The wavelet transform, at high frequencies, gives good time resolution and poor frequency resolution, while at low frequencies; the wavelet transform gives good frequency resolution and poor time resolution. The wavelet analysis is often very effective because it provides a simple approach for dealing with the local aspects of a signal. Wavelet transforms have advantages over traditional Fourier methods in analyzing physical situations where the signal contains discontinuities and sharp spikes.

5.3.1 Basic definition of wavelet transform

A wavelet is a mathematical function used to divide a given function or continuous time signal into different scale components. Usually one can assign a frequency range to each scale component. Each scale component is then studied with a resolution that matches its scale. A wavelet transform is the representation of a function by wavelets. The wavelets are scaled and translated copies (known as “daughter wavelets”) of a finite length or fast decaying oscillating waveform (known as the “mother wavelet”).

$$\psi_{a,b}(t) = \frac{1}{\sqrt{a}} \psi\left(\frac{t-b}{a}\right), \forall a, b \in R, a \neq 0 \quad (5.1)$$

where ψ is a wavelet function, a , is a scaling parameter which measure the degree of compression or scale, and b , is a translation parameter which determines the time location of the wavelet [112].

5.3.2 One dimensional DWT (1D DWT)

The wavelet series is just a sampled version of continuous wavelet transform (CWT) and its computation may consume significant amount of time and resources, depending on the resolution required. If the function being expanded is a sequence of numbers, like samples of a continuous function, the resulting coefficients are called the DWT of the function [112].

One dimensional wavelet theory defines a function ψ , the wavelet, and its associated scaling function ϕ , such that the family of functions $\{\psi^j(x)\} j \in Z$ are orthonormal, where

$$\psi^j(x) = \sqrt{2} \psi(2^j x) \quad (5.2)$$

The wavelet transform can be implemented by quadrature mirror filters G and H are given as $G = g(n)$ and $H = h(n)$, $n \in Z$ where

$$h(n) = \frac{1}{2} \left\langle \phi\left(\frac{x}{2}\right), \phi(x-n) \right\rangle; \quad g(n) = (-1)^n h(1-n) \quad (5.3)$$

($\langle \rangle$ denotes L^2 inner product). The term inner product is a generalised term for dot product. H corresponds to a low pass filter, and G is an octave wide high pass filter. The reconstruction filters have impulse responses as given in Equation (5.4) [114].

$$h^*(n) = h(1-n); \quad g^*(n) = g(1-n) \quad (5.4)$$

The main advantage of biorthogonal wavelet is that it is possible to have symmetric filters so that frequency response has linear characteristics. In biorthogonal wavelet representations have two scaling functions $(\phi(t), \tilde{\phi}(t))$, where $\phi(t)$ is the primal scaling function and $\tilde{\phi}(t)$ is the dual scaling functions. There are two wavelet functions $(\psi(t), \tilde{\psi}(t))$ among which $\psi(t)$ is the primal wavelet function and $\tilde{\psi}(t)$ is the dual wavelet functions. The primal functions and their dual are biorthogonal to each other. The primal scaling function is orthogonal with dual wavelet function while dual scaling function and primal wavelet functions are orthogonal. The wavelet transform can be implemented by quadrature mirror filters,

$$G = g(n), \tilde{H} = \tilde{h}(n) \quad \text{and} \quad H = h(n), \tilde{G} = \tilde{g}(n), \quad n \in Z,$$

$$\text{where } \tilde{g}(n) = (-1)^{1-n} h(1-n); \quad \tilde{h}(n) = (-1)^n g(1-n) \quad (5.5)$$

H, \tilde{H} correspond to low pass filters, and is an octave wide high pass filters.

A group of transform coefficients resulting from the same sequence of low pass and high pass filtering operations gives approximation and detail coefficients respectively.

5.3.3 Two dimensional DWT (2D DWT)

2D DWT is an extension of 1D DWT. The main area of its applications are image denoising, art authentication, digital forensics, etc. 2D DWT of an image can be obtained by applying a separable filter bank to the image. Applying the one dimensional transform in each row, we get two subbands - approximation and details coefficients in each row (L and H subbands). It is well known that approximation is the average value i.e., low frequency information while details gives high frequency information. Then applying 1D DWT column-wise on these L and H subbands, four subbands LL , LH , HL , and HH are obtained. LL is a coarser version of the original input signal called approximation image. LH , HL , and HH are the high frequency subbands containing the detail information (vertical, horizontal and diagonal details images). The decomposition performed on original image to obtain subbands is called subband decomposition [69]. Fig 5.3 shows 2D DWT performed in separable form on an image while Fig 5.4 depicts the two level decomposition of the image.

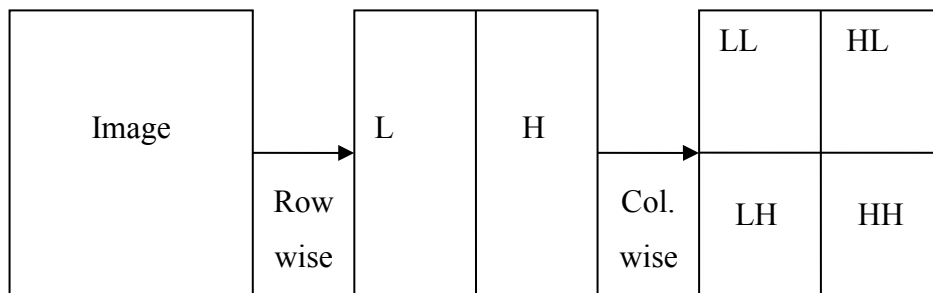


Fig. 5.3 Single level decomposition in 2D DWT computation

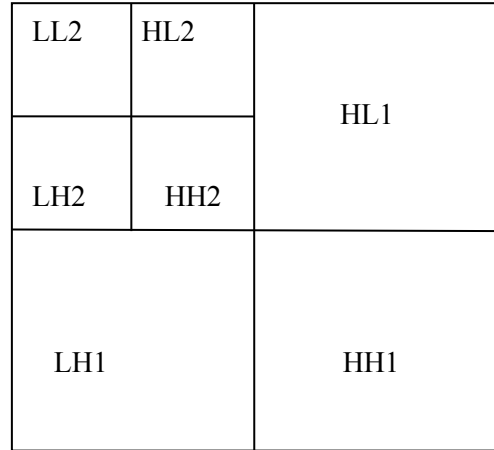


Fig. 5.4 Two level decomposition in 2D DWT computation

5.3.4 Correlational properties of wavelet transform

Let $f(t)$ be a signal whose wavelet transform is to be calculated. Let CA_j and CD_j be the approximation and details coefficients at decomposition level j . We assume the signal to be stationary and so transform coefficients also should have same property. The expectation of approximation coefficients at the j^{th} level can be given as

$$E[CA_j] = \sqrt{2^{-j}} \int f(t) E_n(\Phi(2^{-j}t - n)) dt \approx \frac{\sqrt{2^{-j}}}{N} \int f(t) dt \quad (5.6)$$

where E_n is an average operator while N is the length of support range of $\Phi(2^{-j}t - n)$. The expectation of approximation coefficients is proportional to the average of the original signal. It can also be found that detail coefficients have zero mean.

$$E[CD_j] = \sqrt{2^{-j}} \int f(t) E_n(\Psi(2^{-j}t - n)) dt \approx 0 \quad (5.7)$$

The autocorrelation of CA_j and CD_j are proportional to autocorrelation of original signal. CA_j and CD_j are decorrelated. The detail coefficients at different levels are also decorrelated. The property of localized wavelet transform coefficients is exploited in our method. This property will lead to more correlation of wavelet coefficients in the same prediction channel. The higher the correlation, the more is the scope for redundancy removal in prediction filtering [63].

5.4 Linear prediction

In predictive coding the information already received (in transmission) is used to predict future values. The difference between predicted and actual value is the error and it is encoded to get the compressed image. For decompression, the symbol is decoded and using predictor and error the original image is reconstructed. This is the case of lossless predictive coding. In case of lossy predictive coding, the error is quantized before decoding. Decompression is similar to lossless prediction coding. Optimal prediction and quantization minimizes mean square prediction error [8].

Images can be modeled using homomorphic systems, in which a logarithmic transformation is used to convert multiplicative superposition to additive superposition of signals. In such systems linear prediction can be compatible [115]. Linear prediction (LP) model optimally extract information about a current sample from a neighborhoods of samples in its causal past [116]. The process of signal or system modeling removes redundancy, which is the essence of data compression. Linear predictive coding (LPC) is a popular and efficient technique mainly used in signal compression and speech processing. The signal is modeled as a linear combination of its past values and a hypothetical input to a causal system

whose output is the given signal. In the frequency domain, this is equivalent to modeling the signal spectrum by a pole zero model [62]. The sample of the signal is predicted and if the prediction is done from weighted sum of other samples of the signal, the linear predictive model is auto regressive (AR) model [117]. The model parameters are obtained by a least squares analysis in the time domain and frequency domain [62].

Monson H Hayes [118] gives a good explanation about linear prediction. The AR model of a signal expresses the signal as finite linear aggregate of its previous values. Considering Markov model and exploiting the autocorrelation among the values Yule Walker Equations are obtained. Solving them we can obtain the predictor coefficients.

The values of stochastic process at equally spaced times, $n, (n-1), (n-2), \dots$ are denoted by $y(n), y(n-1), y(n-2), \dots$

$$y(n) = \alpha_1 y(n-1) + \alpha_2 y(n-2) + \dots + \alpha_p y(n-p) \quad (5.8)$$

Exploiting autocorrelation values (R) and predictor coefficients (α) the Yule Walker equations can be arrived at.

$$R_{yy}(k) = \sum_{m=1}^p \alpha_k R_{yy}(m-k) \quad (5.9)$$

Using Levinson Durbin algorithm the above equations can be solved. Levinson Durbin algorithm is as follows:

1. Initialise the recursion

$$\begin{aligned} \alpha_0(0) &= 1 \\ \varepsilon_0(0) &= r_{yy}(0) \end{aligned}$$

2. For $k=0,1,2,\dots,M$

$$\gamma_{p-1} = r_{yy}(p) + \sum_{k=1}^{p-1} \alpha_p(k) r_{yy}(p-k)$$

$$\Gamma_p = \frac{\gamma_{p-1}}{\varepsilon_{p-1}}$$

$$\alpha_p(k) = \alpha_{p-1}(k) + \Gamma_p \alpha_p^*(p-k)$$

$$\alpha_p(k+1) = \Gamma_p$$

$$\varepsilon_{p+1} = \varepsilon_p \left[1 - \left| \Gamma_{p+1} \right|^2 \right]$$

Thus we can obtain the predictor coefficients. In the above algorithm, Γ denotes the reflection coefficient, while ε prediction error. Using these coefficients, the signal can be predicted using Equation (5.8) [118].

5.5 Performance measures

Visually indistinguishable image for one person need not be indistinguishable for another. The same image may not appear indistinguishable under different circumstances like lighting, viewing distance and display characteristics. A compressed image can differ from the original without necessarily being worse.

There is no single approach to quality measurement which has universal acceptance. The various approaches to quality evaluation can be broadly classified as computable objective measures, subjective evaluation and simulation and statistical analysis of specific application for example, diagnostic accuracy [89].

The methods developed here are evaluated both subjectively and objectively. When an image is compressed some of the information will be

lost. It is required to quantify the nature and extent of information loss, so assessment criteria is adopted. When the level of loss of information is expressed as a function of original input image and the compressed and decompressed output image, it is based on objective fidelity criterion.

The commonly used objective fidelity criteria include root mean square error, mean square signal to noise ratio, peak signal to noise ratio etc.

Let $f(x, y)$ be the input image and $\hat{f}(x, y)$ be the output image. Then the above said criteria can be defined as follows: Root mean square error e_{rms} .

$$e_{rms} = \sqrt{\frac{1}{MN} \sum_{x=0}^{M-1} \sum_{y=0}^{N-1} [\hat{f}(x, y) - f(x, y)]^2} \quad (5.10)$$

Mean signal to noise ratio SNR_{rms} is defined as

$$SNR_{rms} = \frac{\sum_{x=0}^{M-1} \sum_{y=0}^{N-1} \hat{f}(x, y)^2}{\sum_{x=0}^{M-1} \sum_{y=0}^{N-1} [\hat{f}(x, y) - f(x, y)]^2} \quad (5.11)$$

Peak Signal to noise ratio SNR_{peak} is given by the expression

$$SNR_{peak} = 10 \log_{10} \frac{(L-1)^2}{\frac{1}{MN} \sum_{x=0}^{M-1} \sum_{y=0}^{N-1} [\hat{f}(x, y) - f(x, y)]^2} \quad (5.12)$$

where the image is of size $M \times N$ and L is the number of gray levels [8].

NAE is another measure of distortion to assess the quality of images in case of compression. The measure NAE is defined as

$$NAE = \frac{\sum_{x=1}^M \sum_{y=1}^N (f(x, y) - \hat{f}(x, y))}{\sum_{x=1}^M \sum_{y=1}^N f(x, y)} \quad (5.13)$$

NMSE is yet another distortion measure which evaluates the images and can be defined as

$$NMSE = \frac{\sum_{x=1}^M \sum_{y=1}^N (f(x, y) - \hat{f}(x, y))^2}{\sum_{x=1}^M \sum_{y=1}^N (f(x, y))^2} \quad (5.14)$$

NMSE and NAE give the measure of distortion or in other words how much the reconstructed image differs from the original [69]. Even though MSE or PSNR are easy to calculate and deal with for optimizations, they may not correlate well with the human perception of quality. So we choose SSIM as an objective fidelity criterion in addition to already well known ones. The task of similarity measurement is separated into three comparisons: luminance, contrast and structure. SSIM index between signals x and y is

$$SSIM(x, y) = [l(x, y)]^\alpha \cdot [c(x, y)]^\beta \cdot [s(x, y)]^\gamma \quad (5.15)$$

where $\alpha=\beta=\gamma=1$. SSIM values range from 0 to 1. Mean SSIM is used to evaluate overall image quality. It is obtained as

$$MSSIM(X, Y) = \frac{1}{M} \sum_{j=1}^M (x_j, y_j) \quad (5.16)$$

where X and Y are the reference and the distorted images, respectively; x_j and y_j are the image contents at the j^{th} local window; and M is the number of local windows in the image [119].

Subjective fidelity criteria measure the image quality by subjective evaluations of human observers. This can be done by showing decompressed image to a group of viewers and averaging their evaluations. The evaluations can be made using an absolute rating scale, for eg. $\{-3, -2, -1, 0, 1, 2, 3\}$ to represent evaluations as {much worse, worse, slightly worse, the same, slightly better, better, much better}[8].

Now after having an idea of general compression schemes and assessment criteria to evaluate the compression algorithms the focus is moved to the different compression techniques newly envisaged as a part of this research work. The developed algorithms involve the use of DWT and linear prediction on the images under consideration. The techniques developed are evaluated on natural as well as medical images.

5.6 Compression techniques using linear prediction and DWT

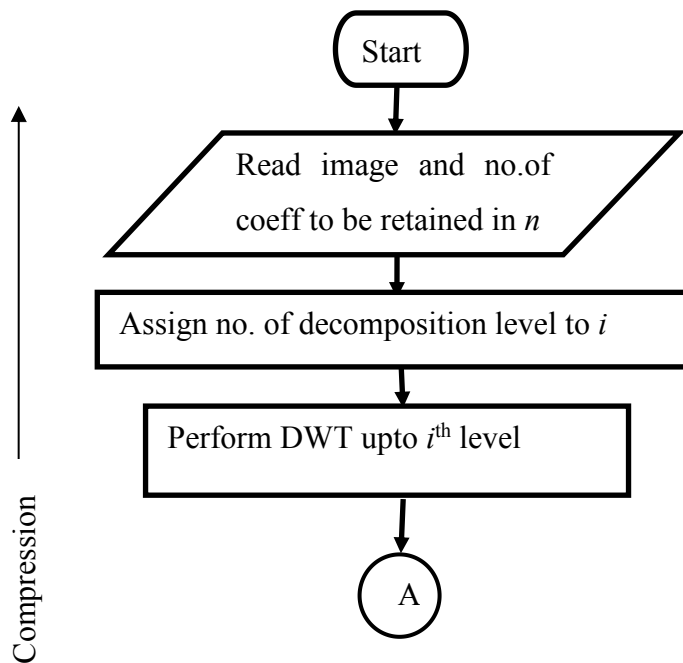
The algorithm starts with decomposition of the image using DWT and linear prediction is done on detail coefficients. Only few predictor coefficients and detail coefficients are retained in the compression. This algorithm uses linear prediction on row and columns of DWT decomposed image. Prediction on wavelet coefficients exploits the correlational properties of wavelet transform coefficients. Let CA_j and CD_j be the approximation and details coefficients of a signal at decomposition level j . The expectation of approximation coefficients is proportional to the average of the original signal. It can also be found that detail coefficients have zero mean. The autocorrelation of CA_j and CD_j are proportional to autocorrelation of original signal. CA_j and CD_j are decorrelated. The correlation of wavelet coefficients in the same prediction channel is due to

property of localised wavelet transform coefficients. The higher the correlation, the more is the scope for redundancy removal in prediction filtering.

Depending on the direction of decomposition and prediction three algorithms are developed. The first algorithm uses row/column wise linear prediction on row/column wise 1D DWT of the image while the second algorithm utilises row and column wise linear prediction on row/column wise 1D DWT of the image. The third algorithm utilizes 2D DWT and both row and column wise predictions. From the retained coefficients prediction is done to reconstruct the original image.

5.6.1 Generalised algorithm steps

The three algorithms can be generalised to have a simple representation. The flow chart of the generalised representation is given below:



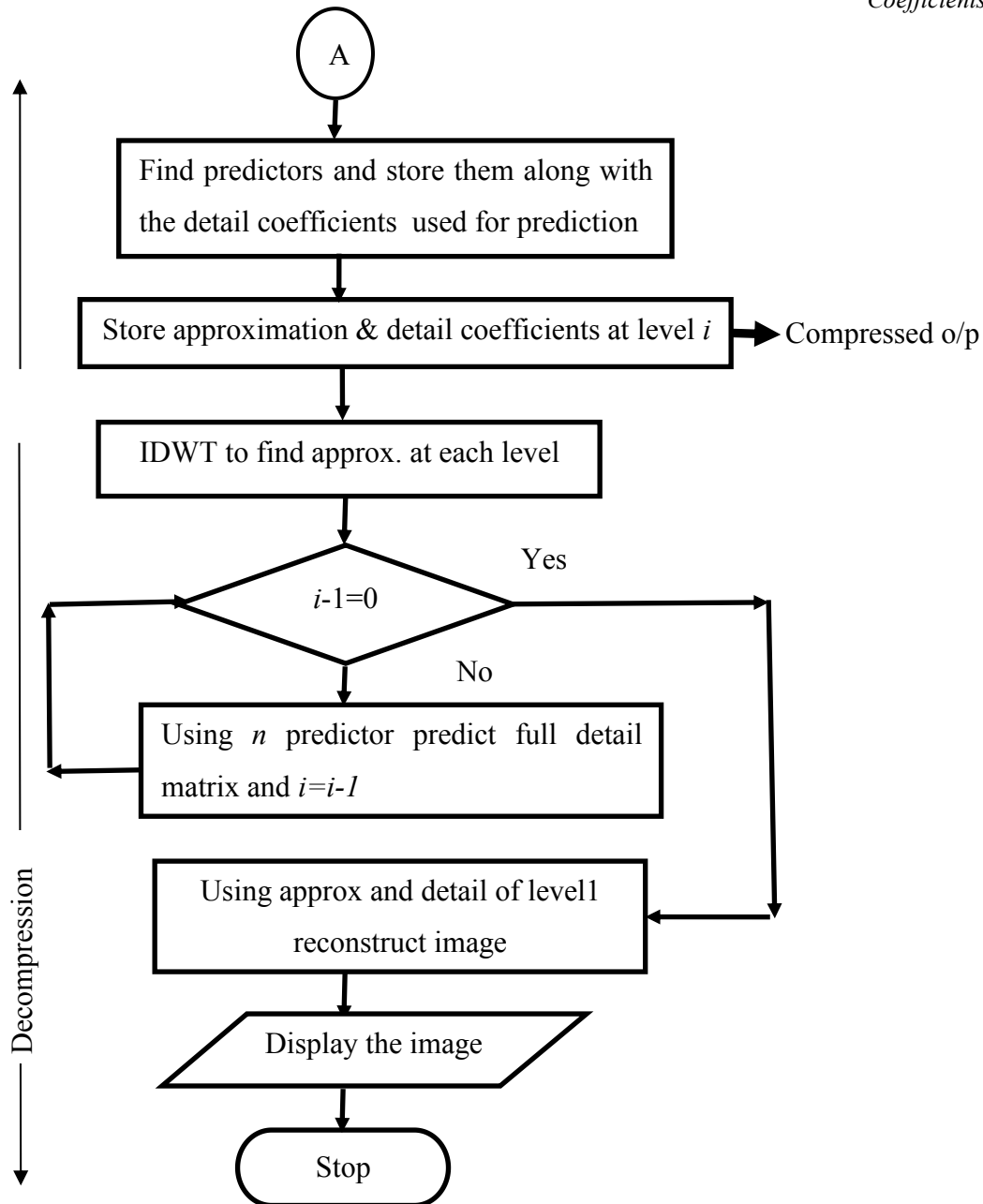


Fig. 5.5 Flow chart : generalised compression\decompression algorithm

The algorithms are explained in the subsequent subsections.

5.6.2 Row/column wise LP on row/column wise 1D DWT

The proposed algorithm performs a row/column wise DWT on the test image. Decomposition up to four levels is performed using *bior9/7*. The approximation and detail coefficients of fourth level only are retained for performing this algorithm. Predictor coefficients for each row/column in detail coefficients at $(i+1)^{th}$ level is obtained. Few prediction coefficients and that much detail coefficients, in each level are transmitted along with retained coefficients from fourth level. With as less as five predictor coefficients and that much detail coefficients in the i^{th} level, all the details coefficients in the i^{th} level can be reconstructed. Approximation coefficients for i^{th} level is obtained from inverse DWT on $(i+1)^{th}$ level of wavelet coefficients. Using approximation and detail coefficients of i^{th} level approximation of $(i-1)^{th}$ level is obtained. Thus the whole image is reconstructed.

5.6.3 Row and column wise LP on row/column wise 1D DWT

This method utilizes the correlation of localized wavelet transform coefficients. This property will lead to more correlation of wavelet coefficients in the same prediction channel. 1D DWT is performed along the rows/columns of the original image up to four levels and fourth level wavelet transform coefficients are retained. The predictor coefficients for each row/column in detail coefficients at $(i-1)^{th}$ level are calculated. The compressed image is formed from few prediction coefficients and that much detail coefficients, at each level along with retained coefficients .

In the decompression, with a few predictor coefficients and that much detail coefficients in the i^{th} level, all the details coefficients in the i^{th} level are reconstructed. Approximation coefficients for i^{th} level is obtained from inverse DWT on $(i+1)^{th}$ level of wavelet coefficients. Using

approximation and detail coefficients of i^{th} level, approximation of $(i-1)^{th}$ level is obtained. Thus the whole image is reconstructed.

The algorithms developed for the proposed method is shown below. This can be applied on the image either along the rows or columns. The algorithm is discussed in the next subsection while its results are discussed in the subsequent subsection.

Compression

Step1: Select the image of interest and input the number of coefficients, n to be retained.

Step2: Perform DWT on the image.

Decompose the image into wavelet transform coefficients applying 1D DWT on the image row/column wise.

Step3: Retaining the coefficients

Retain the fourth level decomposition coefficients so that they can be used for reconstruction. In addition to that n rows/columns of each level are also retained.

Step4: Obtain the predictor coefficients.

Take the first row/column and find n predictors for first row/column of detail coefficients. Similarly find n predictors for first n rows/columns. Also find column wise/row wise n predictors for the remaining columns/rows. Do this for all the levels of decomposition.

Decompression

Step1: Reconstruction of detail coefficients.

- a) Initialise an array for predicted coefficients.
- b) Using first n coefficients in the row/column and n predictors the

whole row/column is reconstructed. It is done for n number of rows/columns.

c) Now consider the first column/row. We have n elements in first column/row. Using the n column/row predictors the whole column/row is reconstructed.

d) Repeat step (c) for all columns/rows.

Step2: Reconstruction of approximation coefficients

Applying 1D IDWT on the corresponding rows/columns on $(i+1)^{th}$ level coefficients, i^{th} level approximation is reconstructed.

Step3: Reconstruction of previous levels.

Steps 1 and 2 are repeated till $i = \text{zero}$. Thus the original image is reconstructed from prediction.

5.6.4 Row and column wise LP on 2D DWT

This algorithm proposes two dimensional decomposition of the image using *bior9/7* wavelet. The other steps are similar to that in previously discussed algorithms. Here we propose four methods for compression utilising prediction on horizontal, vertical and diagonal detail coefficients at each level. In the first variant, row wise prediction of subband coefficients is done whereas the second one predicts column wise. In the third and fourth variants, horizontal subbands coefficients are predicted row wise and vertical subbands coefficients are predicted column wise. The two differs in the handling of diagonal coefficients. The diagonal elements are extracted from diagonal subbands and arranged in horizontal fashion and prediction is done row wise in the third variant while the fourth variant predicts in column wise direction.

5.7 Results and Discussion

The results of the algorithms described in the previous section is discussed in this section. The input and output images are shown to emphasise that quality of the image is not compromised. In addition to that, the performance measures like PSNR, NMSE, NAE and SSIM are also evaluated to have a look at the image quality of decompressed images.

5.7.1 Row / column wise LP on row/ column wise 1D DWT

The outcome and inference from the usage of the first algorithm is discussed in this section. The results of row wise prediction on row wise decomposition and column wise prediction on column decomposition variants are discussed separately.

5.7.1.1 Technique using row wise prediction and decomposition

The natural gray scale and medical images with large dimensions (above 1024 x 1024 pixels) are used for testing the algorithms developed. They are made available as bench mark for image compression and are in PGM format. Fig 5.6 and 5.7 show the original (left) and decompressed (right) versions of a computed radiographic (CR) images and natural image respectively. Fig 5.6 shows a *cr* of 7:1 while image shown in Fig 5.7 has a *cr* of 6.7:1.



Fig. 5.6 Reconstruction of a medical image using row wise decomposition
a) Original Image b) Reconstructed Image

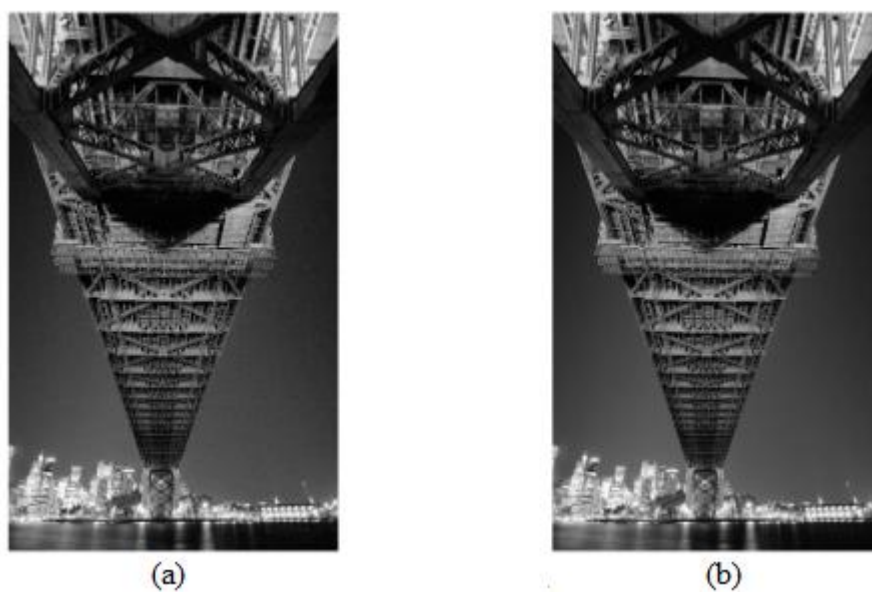


Fig. 5.7 Reconstruction of a natural image using row wise decomposition
a) Original Image b) Reconstructed Image

The biorthogonal wavelet which is suited for image compression is used here. The magnified versions of original and decompressed images are shown for comparison in Fig 5.8 and Fig 5.9.

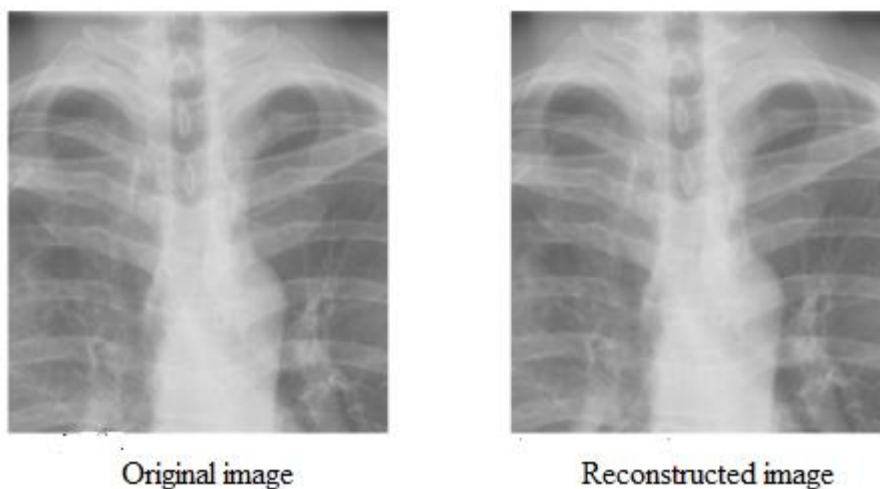


Fig. 5.8 Zoomed version of Fig. 5.6 by a factor of 2

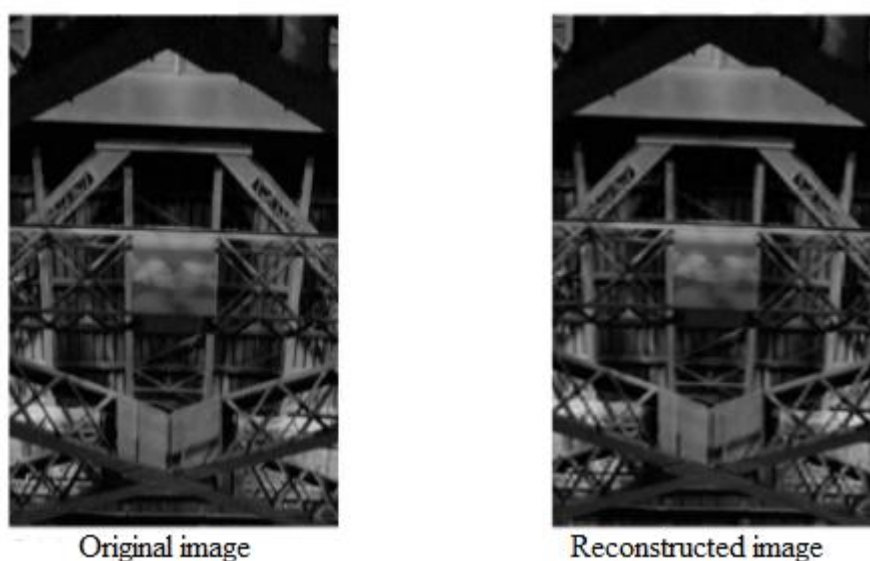


Fig. 5.9 Zoomed version of Fig. 5.7 by a factor of 4

The subjective assessment of the reconstructed images is also done. As per the feedback this method is found to be effective in compressing the images without losing their vital information.

The performance of the algorithm is validated using objective criteria like PSNR, NMSE, NAE and bits per pixel (bpp) and various

performance curves are shown in Fig 5.10. As expected PSNR decreases as compression ratio increases PSNR decreases but at higher compression ratio, PSNR decreases at slower rate. This method produced PSNR higher than 45dB for some images.

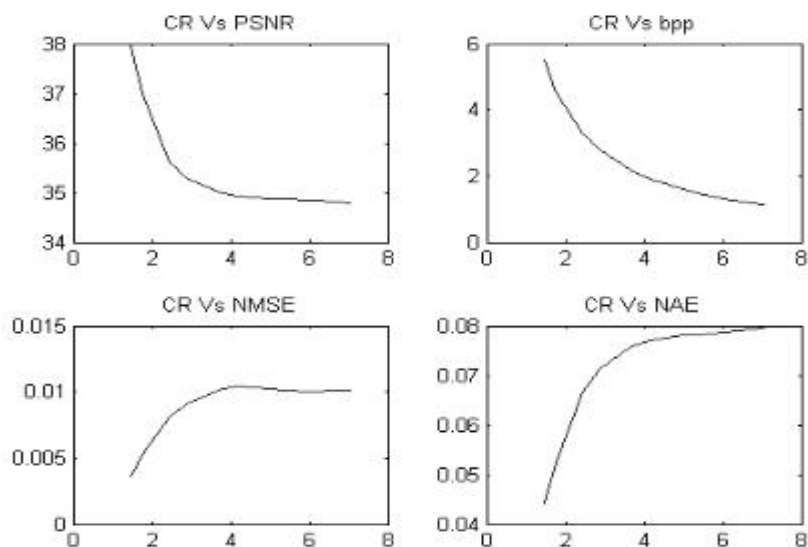


Fig. 5.10 Performance curves for algorithm using row wise decomposition

The proposed method works well with images of large dimensions. This method gives same compression ratio and bpp on images of same size. Here the correlation of each row in the image with its wavelet coefficients is exploited to predict the next wavelet coefficients. The prediction can be done with number of coefficients as small as five. The performance method is evaluated on the basis of subjective criteria and parameters like PSNR, NAE, NMSE and bpp. The experimental results show that the proposed method, in addition to achieving good compression gives a better performance.

5.7.1.2 Technique using column wise prediction and decomposition

The dataset used here is the medical image set made available by

Roman Starosolski. The set contains medical images of various modalities (CR, CT, MR and US) stored in the PGM P5 format [120]. The CR images usually have large matrix size. The biorthogonal wavelet is used here also. The original (left) and reconstructed (right) images are shown in Fig 5.11.



Fig. 5.11 Original and reconstructed images: using column wise decomposition

The performance of the algorithm is validated using objective criteria like PSNR, NMSE and various performance curves are shown in Fig 5.12. It is found that as the number of coefficients retained increases PSNR increases. At higher compression ratio, PSNR decreases at slower rate. Here PSNR is higher than 40dB for CR images. The variation of NMSE with compression ratio shows that at low compression ratio, NMSE increases at a rapid rate and for high compression ratio it decreases at a slower rate. The results are compared with the method in discussed in the previous subsection.

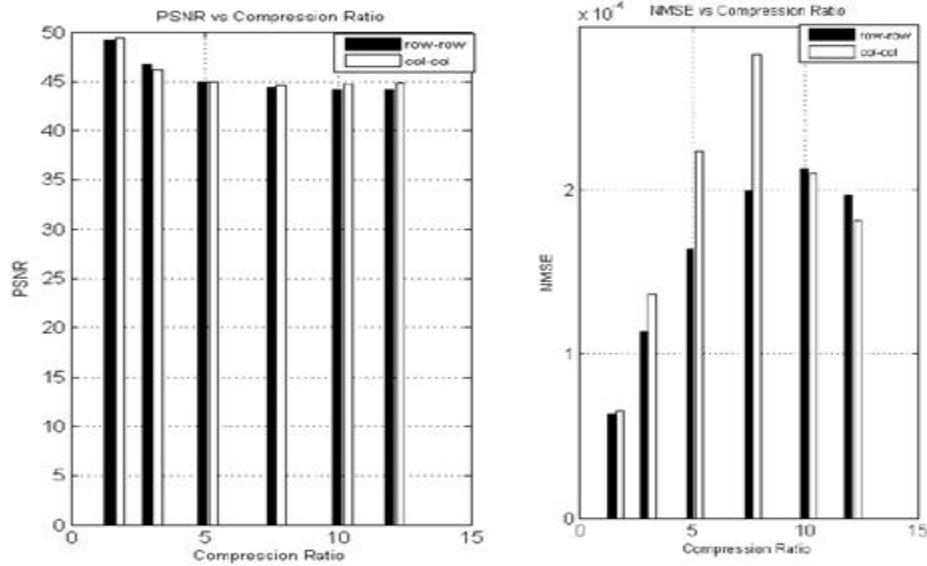


Fig. 5.12 Comparison of variations of PSNR & NMSE with cr .

It can be found from the graphs that both the methods give comparable performances in case of PSNR. The NMSE for the proposed method is slightly higher than the previous method. The performance curves are also plotted against number of detailed coefficients as shown in the Fig 5.13(a,b,c).

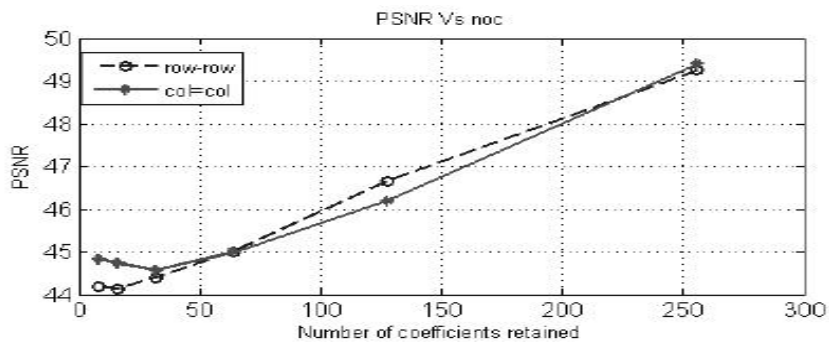


Fig. 5.13 (a) Variation of PSNR with number of coefficients

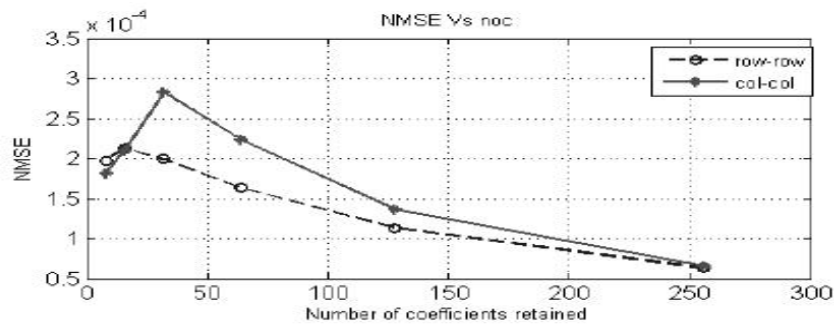


Fig. 5.13 (b) Variation of NMSE with number of coefficients

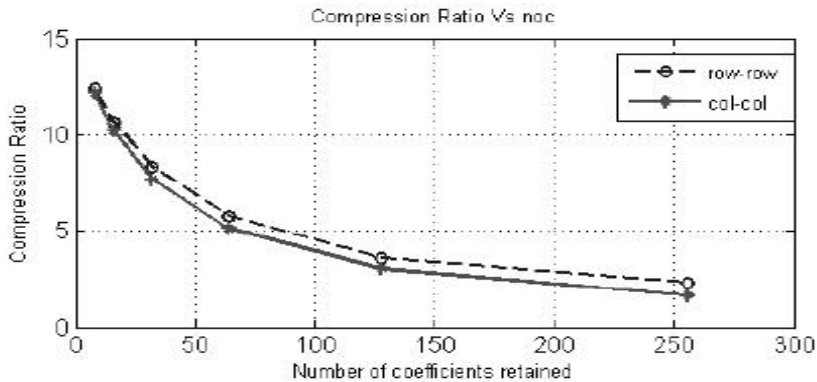


Fig. 5.13 (c) Variation of compression ratio with number of coefficients

The CR image contains lesser amounts of details. The detail is reduced and limited by the blurring that occurs at different stages of the imaging process. The amount of blurring depends upon the size and location of the object, motion and light spreading within the fluorescent screen. When an image is divided into pixels, some amount of blurring occurs. The pixel size is also a factor that contributes to limiting of details. This makes prediction of detail coefficients easy. So the method described here is suitable for CR images. The subjective assessment is also done on the reconstructed images. The original and decompressed images were shown to four different viewers and they were asked to rate the images. As per the feedback an average score of 2 was obtained on the absolute scale

{-3 to 3} representing {much worse to much better}. The value 2 indicates that the visual quality of decompressed image better and diagnostic information is not lost. This method is found to be effective in compressing the images without losing their vital information.

The performance of the method is evaluated on the basis of subjective criteria and parameters like PSNR and NMSE. The experimental results show that the proposed method, in addition to achieving good compression gives a better performance. We can conclude from the performance curves that for CR images with 1D DWT and prediction taken column wise gives a better result than taking 1D DWT and prediction row wise.

5.7.2 Row and column wise LP on row/ column wise 1DDWT

Here also the same test images and same wavelets as in previous sections are used. The algorithm is applied row wise and column wise on the images and results are compared. Fig 5.14 shows the result of row wise prediction on row wise decomposition (middle) and column wise prediction on column wise decomposition (right) on the original image (left) while Fig 5.15 shows magnified versions of the images by a factor of 4. The compression ratio obtained here is 14:1



Fig. 5.14 Comparison of original and reconstructed image (a) Original Reconstruction (b) row wise (c) col. wise

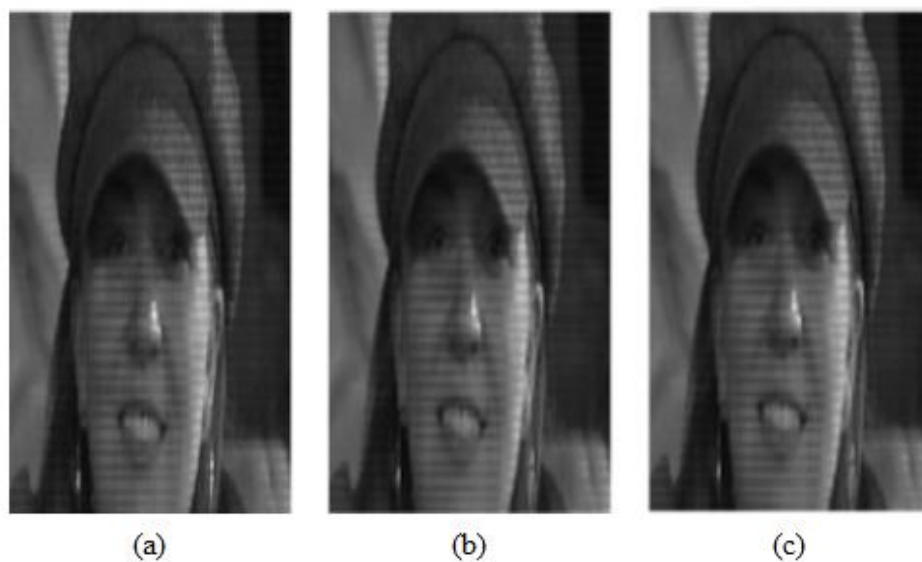


Fig. 5.15 Comparison of zoomed versions of original and reconstructed image (a) Original Reconstruction (b) row wise (c) col. wise

The performance of the algorithm is validated using objective criteria like PSNR, NMSE, NAE and bpp and various performance curves are shown in Fig 5.16. It is found that as compression ratio increase PSNR

first decreases and then increases. The column wise decomposition gives a better performance as there is not much variation in PSNR values with compression ratio. This method gives PSNR value as high as 45dB for some images. NMSE and NAE is less for column wise decomposition compared to row wise decomposition. The variation of compression ratio with bpp is almost same in the case of both the decomposition directions.

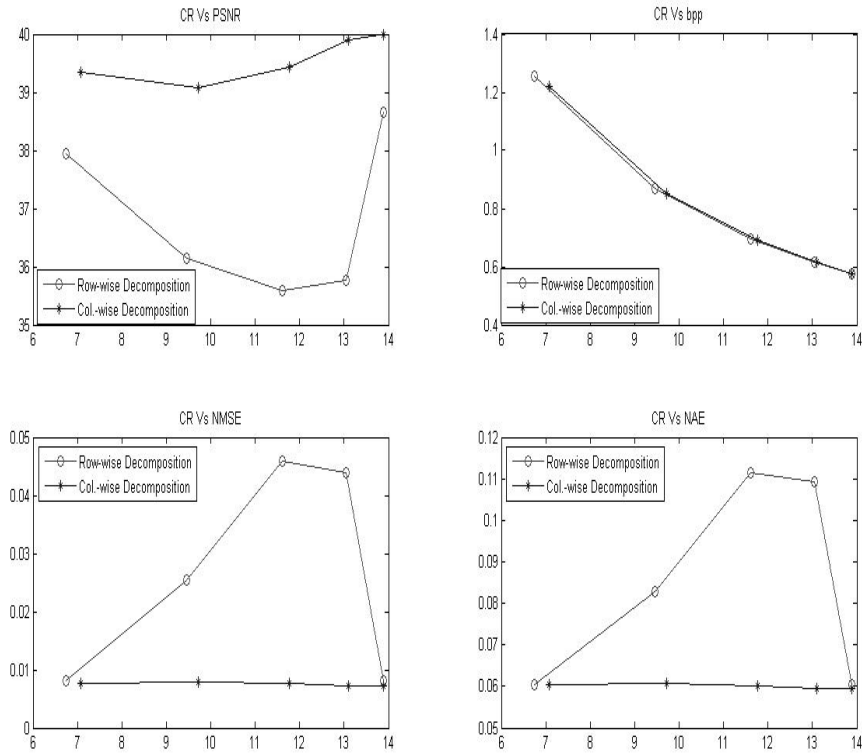


Fig. 5.16 Performance curves comparison

The algorithm was validated using Model Fest database [121]. Out of the 47 images in the database, algorithm worked fine with 39 images. For multi poles category image model the algorithm showed best result. For example, for the image Line31, PSNR is as high as 90dB while NMSE is almost zero and NAE is very low. Among the categories in the database, the row wise decomposition is suitable for Gabor patch with fixed size,

fixed cycles and an optional category with different phase. The reconstruction was possible with as less as 5 coefficients. The PSNR ranged from 53 to 73 dB. In the Gabor patch with fixed cycles category, the one model with high standard deviation after reconstruction contained noise. The noise can be reduced by increasing the number of coefficients retained. The PSNR can be improved to 55 dB by compromising on cr while NMSE and NAE also reduced.

The elongated Gabor patch, Gabor patch with different aspect ratio, Gabor patch with different orientation, Gabor patch with different subthreshold summation categories also showed good results for this method. The elongated Gabor patch and patch with different aspect ratio gives PSNR as high as 73dB, NMSE value as 0 and NAE as low as 0.000046.

For collinear patch category, the reconstructed images are corrupted by noise but still recognisable. Here also increase in the number of coefficients retained, removes noise and improves the performance in terms of PSNR, NMSE and NAE. But cr reduces.

In ModelFest database majority of the images have horizontal orientation and algorithm using row wise decomposition is best suited in this case. Some of the original and reconstructed images from the database using row wise decomposition algorithm are given in the Fig 5.17 and Fig 5.18.

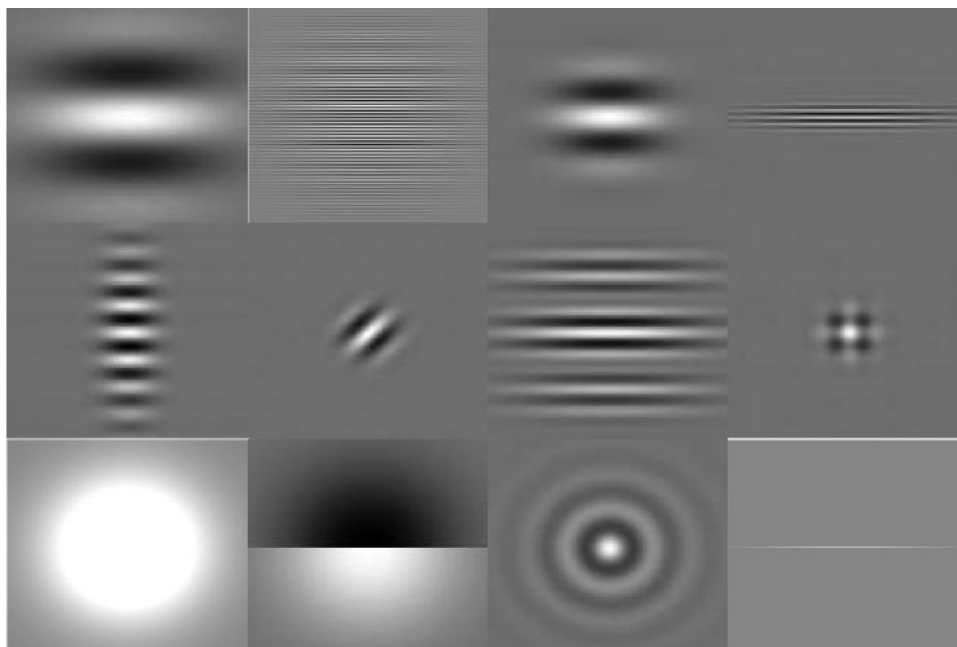


Fig. 5.17 Original images from ModelFest database

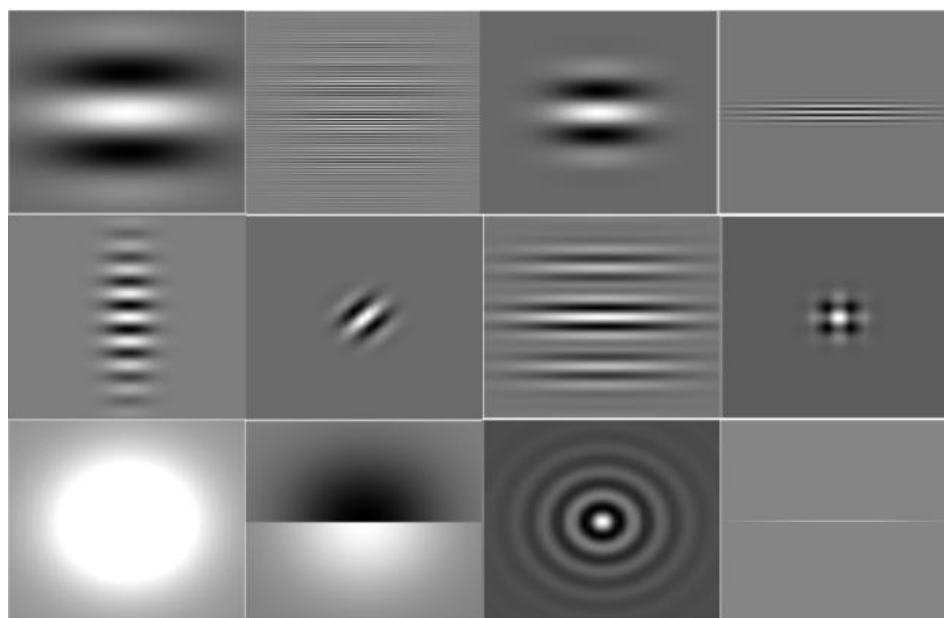


Fig. 5.18 Reconstructed images using row wise decomposition

On all the images, the algorithm using column wise decomposition is also tried out. The algorithm worked well for many images namely the category of Gabor patch with different phase. The algorithm using column wise decomposition when applied to those images after giving a rotation of ninety degrees is found to give good results. The images Bessel, Gaussian blob with higher standard deviation, Gabor patch with different orientation and plaids showed good results even without rotation of the images. The rotated images and their reconstruction using column wise decomposition are shown in Fig 5.19 and Fig 5.20.

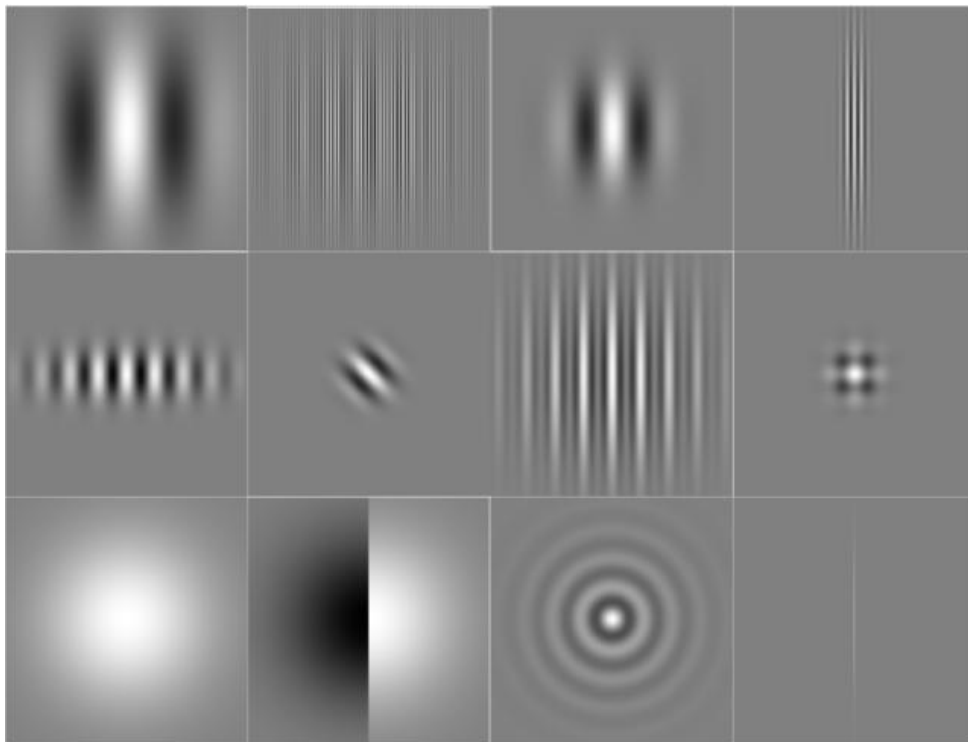


Fig. 5.19 Original images from ModelFest database rotated by 90 degrees

The subjective assessment of the reconstructed images is also done. The original and decompressed images were shown to different viewers and ratings of the images were obtained from them. As per the feedback

this method is found to be effective in compressing the images without losing their vital information.

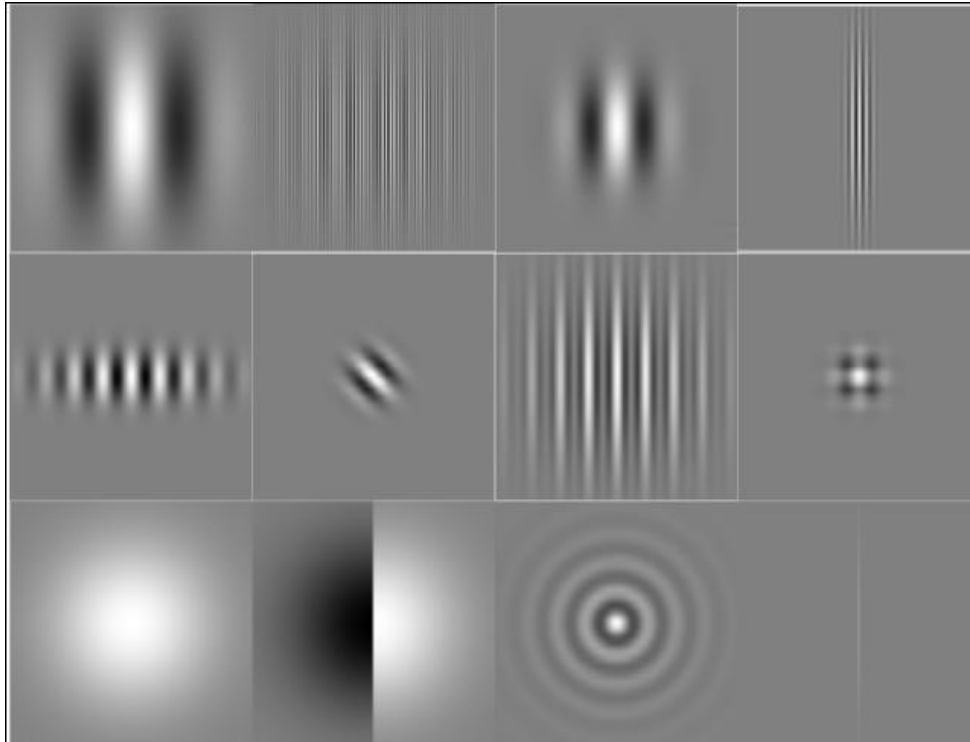


Fig. 5.20 Reconstructed images using column wise decomposition

The proposed method gives same compression ratio and bpp on images of same size. We can conclude that for images with horizontal orientation 1D DWT taken row wise gives a better result while taking 1D DWT column wise suits images with vertical orientation.

5.7.3 Row and column wise LP on 2D DWT

The algorithm is validated using same medical images as in previous algorithms. The biorthogonal wavelet which is suited for image compression is used here. CR images considered here are of dimensions greater than 1024 x 1024. CT and MR images have 512 x 512 dimensions. US images are of the size 640 x 480. The comparison of each performance

measure is done for all the four variants of the proposed method. The parameters plotted against number of coefficients retained for CR images are shown in Fig 5.21.

The performance of the algorithm is validated using objective criteria like PSNR, NMSE, NAE and MSSIM. It is found that as the number of coefficients retained increases PSNR and MSSIM increase whereas NMSE and NAE decrease. For CR images column wise prediction for diagonal subband method is best suited.

The parameters plotted against number of coefficients retained for CT images are shown in Fig 5.22. CT images have high MSSIM for column wise prediction for diagonal subband method. Column wise prediction for diagonal subband method and column wise prediction for all subband method show similar performance in the case of PSNR. Fig 5.23 portrays performance measures for MR images. In case of MR images row wise prediction for all bands shows slightly better performance than other methods when no. of retained coefficients is less. As number of coefficients increases, the performance becomes at par with other methods. Fig 5.24 shows the performance for US images while the original and reconstructed images are shown in Fig 5.25.

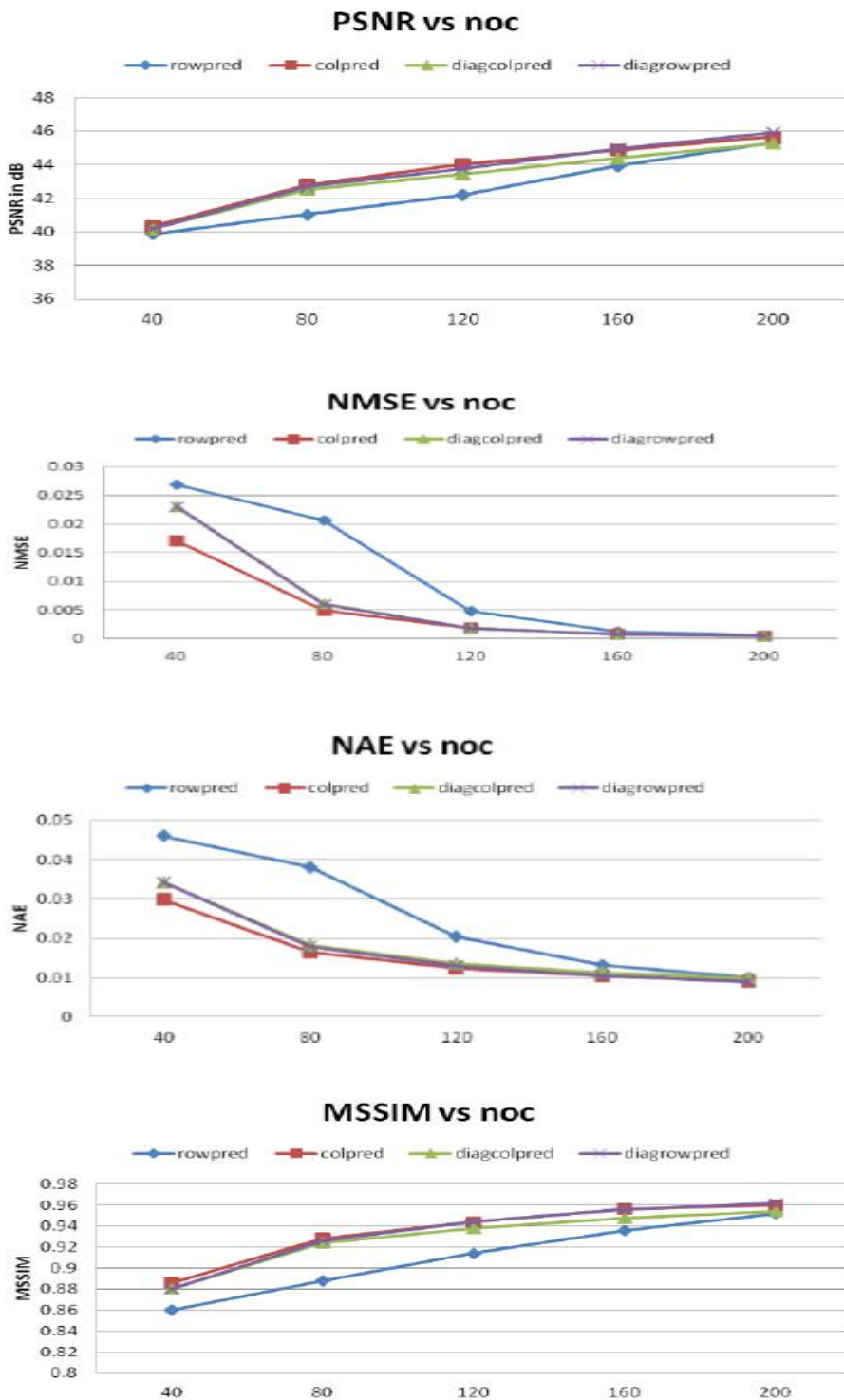


Fig. 5.21 Performance parameters for CR images

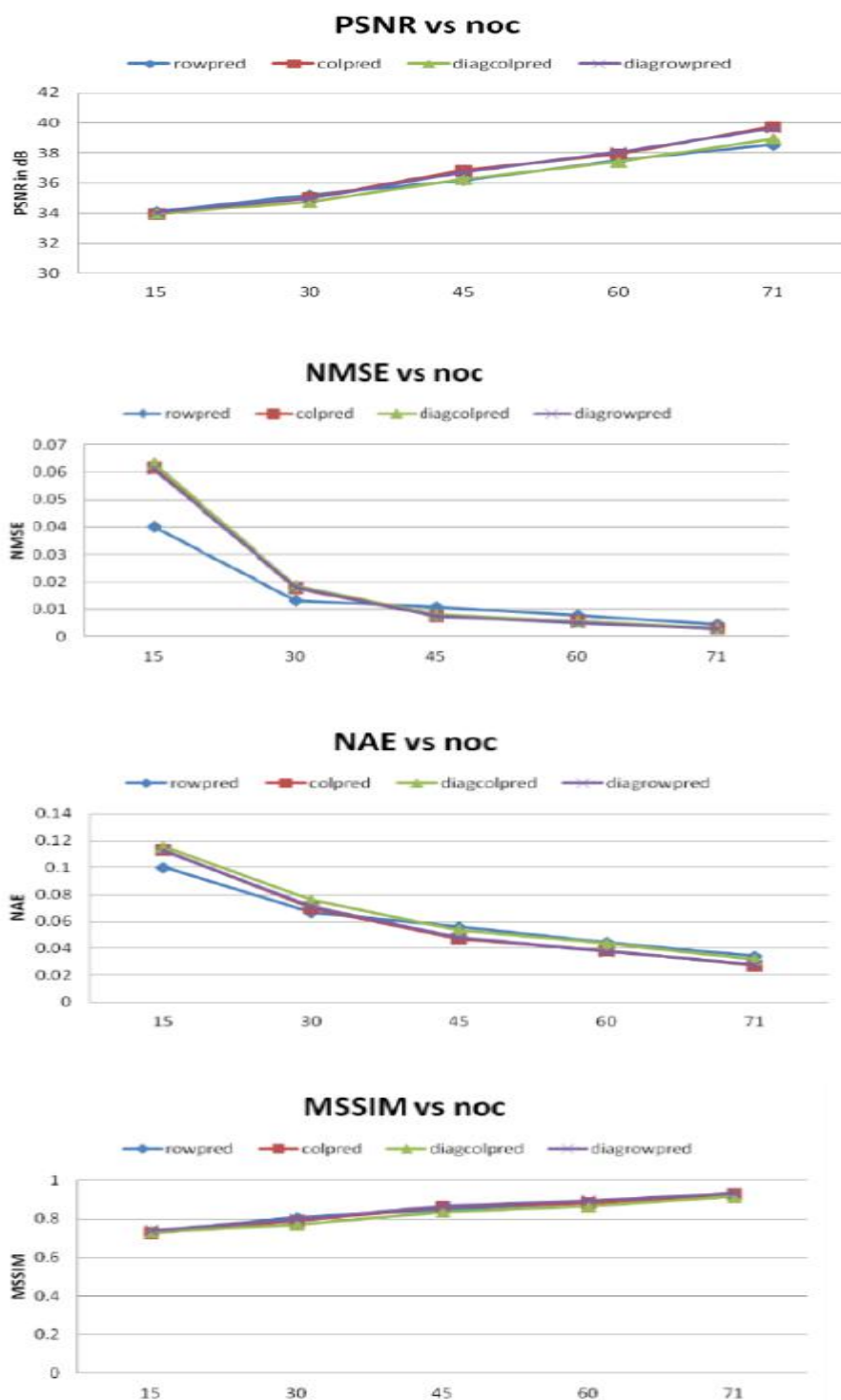


Fig. 5.22 Performance parameters for CT images

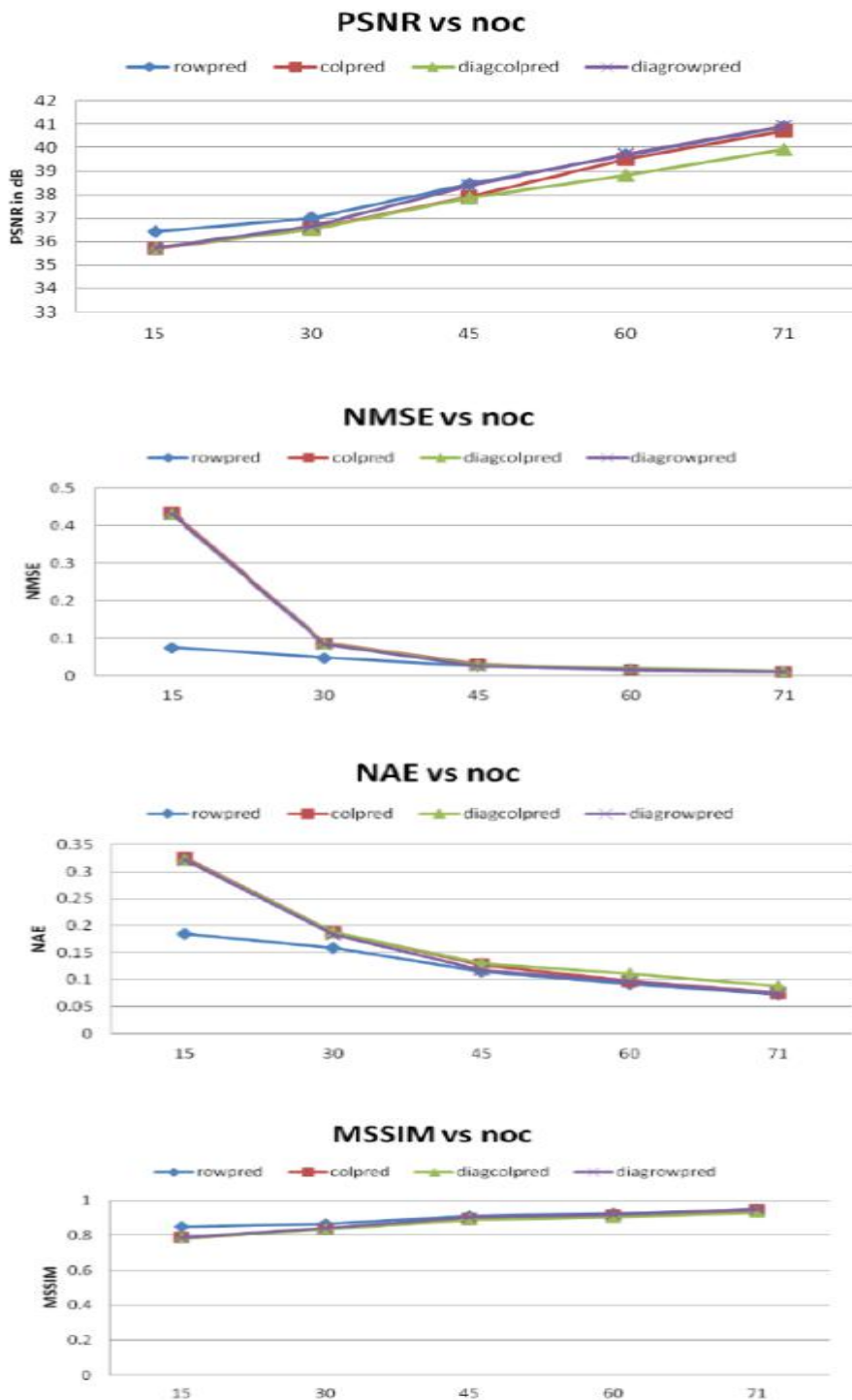


Fig. 5.23 Performance parameters for MR images

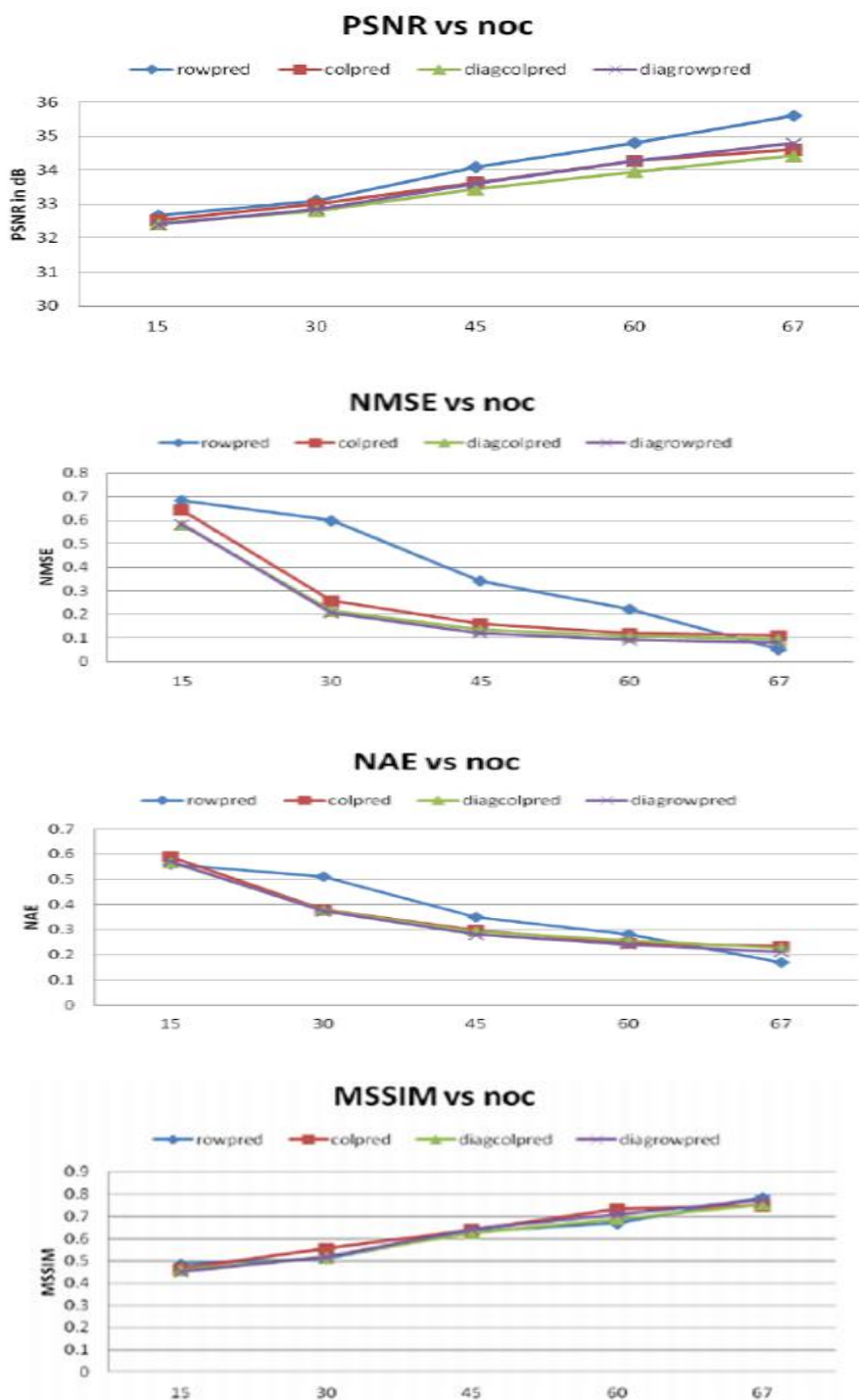


Fig. 5.24 Performance parameters for US images

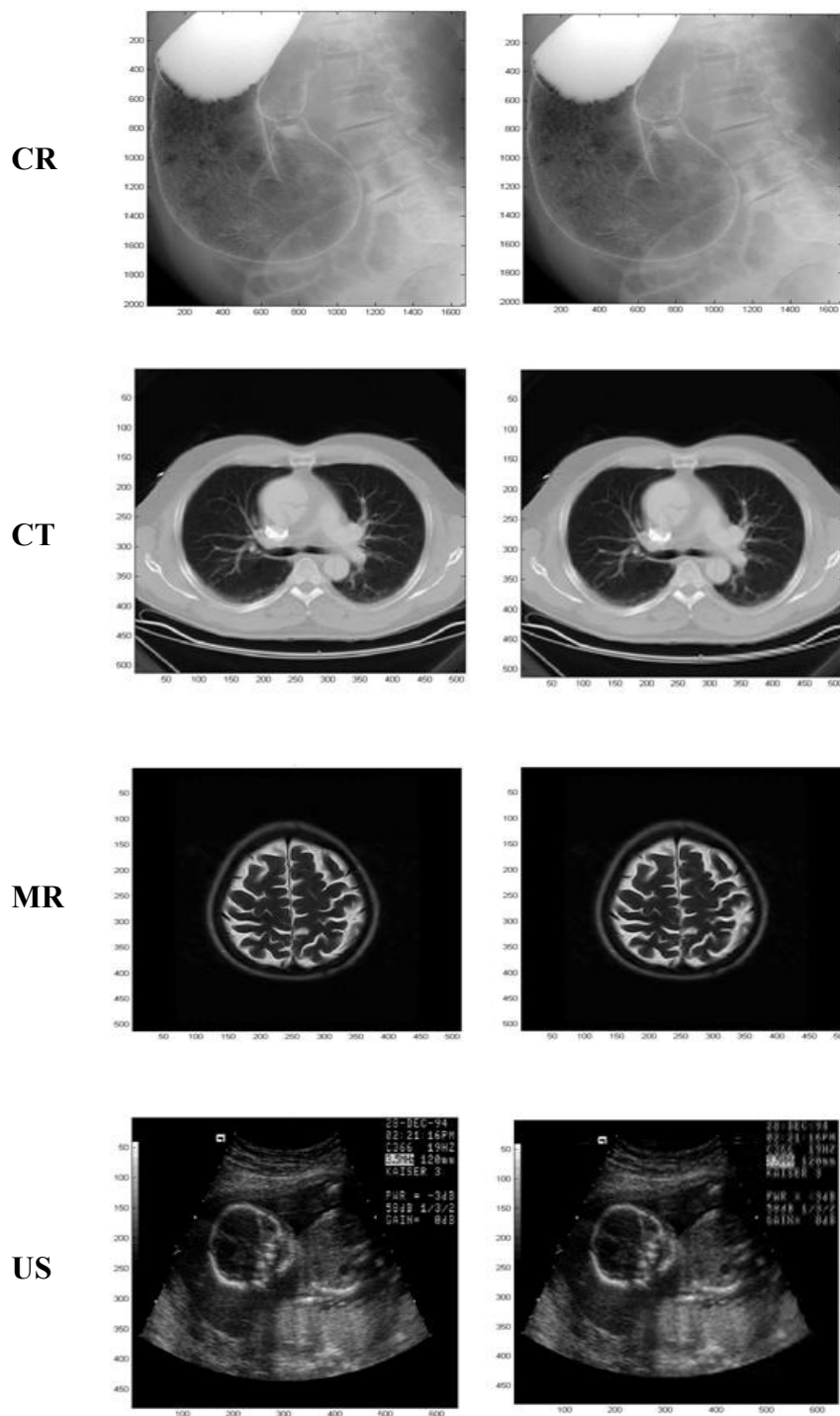


Fig. 5.25 Original(L) and Reconstructed (R)images

The CR image contains lesser amounts of details. The detail is reduced and limited by the blurring that occurs at different stages of the imaging process. The amount of blurring depends upon the size and location of the object, motion and light spreading within the fluorescent screen. When an image is divided into pixels, some amount of blurring occurs. The pixel size is also a factor that contributes to limiting of details. So the method described here is best suited for CR images.

The four variants of the proposed method are evaluated using subjective criteria parameters like MSSIM and NMSE. The experimental results show that the proposed method, gives good compression and better quality images. We can conclude that for CR images the method works best and for US images it gives poor performance.

ModelFest database used for validation consists of images that are high quality HVS models that can also be used to improve compression technologies. All the images are of size 256 x 256. The images in this database are classified into different categories. They are Gabor patch with fixed size, fixed cycles and an optional category with different phase, elongated Gabor patch, Gabor patch with different aspect ratio, Gabor patch with different orientation, Gabor patch with different subthreshold summation, collinear patches, plaid, multipoles, Gaussian blob, white noise and miscellaneous.

The plaid category model can also be compressed with this algorithm without affecting the quality of images. In Gaussian blob category, while algorithm works good for those with higher standard deviation, noise is introduced in the reconstructed versions of those with less standard deviation. Even though noise removal is possible with

increase in number of retained coefficients, ringing is observed in the output.

In the white noise category there are two stimuli - fixed white noise and random white noise. For both the stimuli, the algorithm could not work well. The introduced noise rendered the reconstructed image poor visual quality even when number of coefficients was increased.

In the miscellaneous category, the Bessel function stimulus which is narrow band in spatial frequency but broad band in orientation is present. This method gives good quality reconstructed image for Bessel function stimuli image. The disk image in this category which is a familiar target used in medical imaging research. With this image, on reconstruction the edges are smoothed out and ringing effect is observed. A natural image is also available in the database and its reconstructed image is a blurred one, even though noise can be removed by increasing the number of coefficients. The checker board image is another one in the miscellaneous category where ringing effect is observed [122].

5.8 Conclusion

Three algorithms based on prediction of wavelet coefficients using correlation among wavelet coefficients were developed for image compression. The methods developed can be summarized as follows. The image is decomposed using 1D DWT and linear prediction is done on detail coefficients and only few predictor coefficients and detail coefficients are retained in the compression. Depending on the direction of decomposition and prediction four algorithms are developed. The first algorithm uses row/column wise linear prediction on row/column wise 1D DWT of the image, the second row and column wise linear prediction on row/column

wise 1D DWT of the image while the third utilizes 2D DWT and both row and column wise predictions. From the retained coefficients, prediction is done to reconstruct the original image.

Among the methods developed the method with 2D DWT decomposition and both row and column wise prediction is found to suit PET images the best. The method using 1D DWT and column wise prediction is found to suit CR images.

CHAPTER 6

ROI BASED IMAGE COMPRESSION

6.1 Introduction

The objective of the research work is to develop a novel and efficient scheme for image compression for molecular images that can preserve the true diagnostic information and reduce storage and transmission costs. The technique developed here is modified and applied for mammographic images also. The enhancement and segmentation are done on PET images while compression methods are developed using natural and biomedical images in general. It is well known that an algorithm suiting for one type of image need not work well with other types of images. So the integration of different modules of the work needs description. Three of the widely used compression techniques are incorporated while doing integration. The next section deals with the explanation of the other methods incorporated here.

6.2 Philosophy

The theory on which any research work is based is significant because it shows the direction in which the research is steering to and also helps to have a better understanding of the work. The compression used for PET images have SPIHT and arithmetic coding incorporated along with the developed technique utilising wavelet transform and linear prediction. This section explains SPIHT, arithmetic coding and deflate algorithms.

6.2.1 Set Partitioning in Hierarchical Trees (SPIHT) algorithm

Set partitioning in hierarchical trees (SPIHT) is a compression method that generates a continuously scalable single bit stream that can be used to produce images at various bit rates and quality, without any drop in compression. The decoder simply stops decoding when a target rate or reconstruction quality has been reached. In the SPIHT algorithm, the image is first decomposed into a number of sub bands using hierarchical wavelet decomposition. The subbands obtained for a two level decomposition are shown in Fig 6.1.

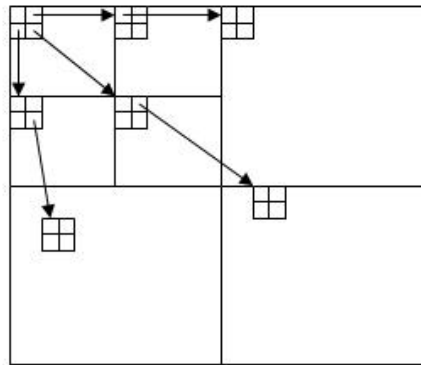


Fig. 6.1 Two level wavelet decomposition with spatial orientation tree

The sub band coefficients are then grouped into sets known as spatial orientation trees, which efficiently exploit the correlation between the frequency bands. The coefficients in each spatial orientation tree are then progressively coded bit plane by bit plane, starting with the coefficients with highest magnitude and at the lowest pyramid levels [1].

The SPIHT algorithm is unique in that it does not directly transmit the contents of the sets, the pixel values, or the pixel coordinates. It transmits the decisions made in each step of the progression of the trees that define the structure of the image. Because only decisions are being

transmitted, the pixel value is defined by what points the decisions are made and their outcomes, while the coordinates of the pixels are defined by which tree and what part of that tree the decision is being made on. The advantage to this is that the decoder can have an identical algorithm to be able to identify with each of the decisions and create identical sets along with the encoder [123].

The data structure in SPIHT algorithm is as follows:

The coefficients are grouped into 2 x 2 arrays except first band. All but one of the coefficients in the lowest resolution band are root nodes. The top left corner of the array does not have any offspring. The tree is partitioned into 4 type of sets which are given below:

- ✧ $O(i,j)$ is the set of coordinates of offsprings of coefficient at (i,j) .
- ✧ $D(i,j)$ is the set of all descendants of coefficient at (i,j) .
- ✧ H is the set of all root nodes.
- ✧ $L(i,j)$ is the set of coordinates of all descendants of coefficient at (i,j) .

where (i,j) is the location. The bits are numbered with LSB being zeroth bit, the next bit being first significant bit and k^{th} bit referred as $k-1$ most significant bit. The algorithm is explained in the following subsection

6.2.1.1 Algorithm

The SPIHT algorithm is given as follows:

Step1: Find the value of $n = \lfloor \log_2 c_{max} \rfloor$ where c_{max} is the highest coefficient.

There are three lists - list of insignificant pixels (LIP), list of insignificant sets (LIS) and list of significant pixels (LSP). LIP is

initialised with set H . Those elements of H that have descendants are also placed in LIS as D type entries. The LIP is initially empty.

Step2: In each pass the members of LIP and then members of LIS are processed. The members of LSP are processed in the refinement step.

Step3: While examining coordinates in LIP, if the coefficient is significant i.e., greater than 2^n , transmit 1 followed by a bit representing sign. Then move the coefficient to LSP list. If not significant transmit 0.

Step4: Next we examine LIS. If set of coordinates is not significant transmit 0, else transmit 1. Now check whether the set is D type or L type.

Step5: If it is of the type D , check the offspring of coefficient at that coordinate, which means to check the four coefficients whose coordinates are in $O(i,j)$.

✧ If coefficient is significant transmit 1, the sign of coefficient, then move the coefficient to LSP. For the rest transmit a 0 and add their coordinate to the LIP.

✧ Now coordinates of $O(i,j)$ are removed from $L(i,j)$. If this set is not empty, move it to the end of LIS and mark it to be of type L . If the set is empty, we remove the coordinate (i,j) from the list.

Step6: If the set is of the type L , we add each coordinate in $O(i,j)$ to the end of LIS as the root of a set of type D . The new entries in LIS are examined in this pass and remove (i,j) from LIS.

Step7: After processing sets in LIS, we go to refinement step. Here each coefficient that was in LSP prior to the current pass is examined and the n^{th} most significant bit of $|c_{ij}|$ is output.

Step8: This completes one pass. n is decremented and process is repeated [124].

6.2.2 Arithmetic coding

Arithmetic coding maps a string of data (source) symbols to a code string in such a way that the original data can be recovered from the code string. The encoding and decoding algorithms perform arithmetic operations on the code string. One recursion of the algorithm handles one data symbol. Arithmetic coding creates a code string which represents a fractional value on the number line between 0 and 1. The coding algorithm is symbol wise recursive; i.e., it operates upon and encodes (decodes) one data symbol per iteration or recursion. On each recursion, the algorithm successively partitions an interval of the number line between 0 and 1, and retains one of the partitions as the new interval. Thus, the algorithm successively deals with smaller intervals, and the code string, viewed as a magnitude, lies in each of the nested intervals. The data string is recovered by using magnitude comparisons on the code string to recreate how the encoder must have successively partitioned and retained each nested subinterval.

The procedure for generating the tag works by reducing the size of the interval in which the tag resides as more and more symbols of the sequence are added. First, we divide the unit interval into subintervals having length proportional to their probability of occurrence. We associate subintervals with the symbols. The appearance of the first symbol in the

sequence restricts the interval containing the tag to one of these subintervals [125].

6.2.3 Deflate algorithm

Deflate algorithm is a compression algorithm that uses the combination of LZ77 algorithm and Huffman coding. The block diagram of deflate algorithm is given in Fig 6.2. A deflate stream consists of a series of blocks. Each block is preceded by a three bit header where the first bit shows the last block in the stream marker. If it is one, the block is the last one in the stream. A zero means more blocks are to follow. The second and third bits represent the encoding method used for the block. 00 in second and third bits means data are stored in raw form whereas 01 indicates Huffman encoded data while 10 shows encoding with reference to a previous sequence (LZ77). In LZ77, a sequence being already part of the previous contents is addressed by the parameter pair 'sequence length' and 'distance'. Both parameters are encoded with the help of Huffman trees providing length and distance codes.

Within compressed blocks, if a repeated string is spotted, then a back reference is inserted, linking to the previous location of that identical string instead. An encoded match to an earlier string consists of a length and a distance. Relative back references can be made across any number of blocks, as long as the distance appears within the last 32kB of uncompressed data decoded [126].

After discussing the philosophy behind the integration, the integration adopted in this work is explored next. In this work the image under consideration is first enhanced and a suitable ROI is found and part of image inside ROI is compressed with low compression ratio while that

outside ROI is compressed with high compression ratio. The method adopted for PET and mammographic images are discussed separately.

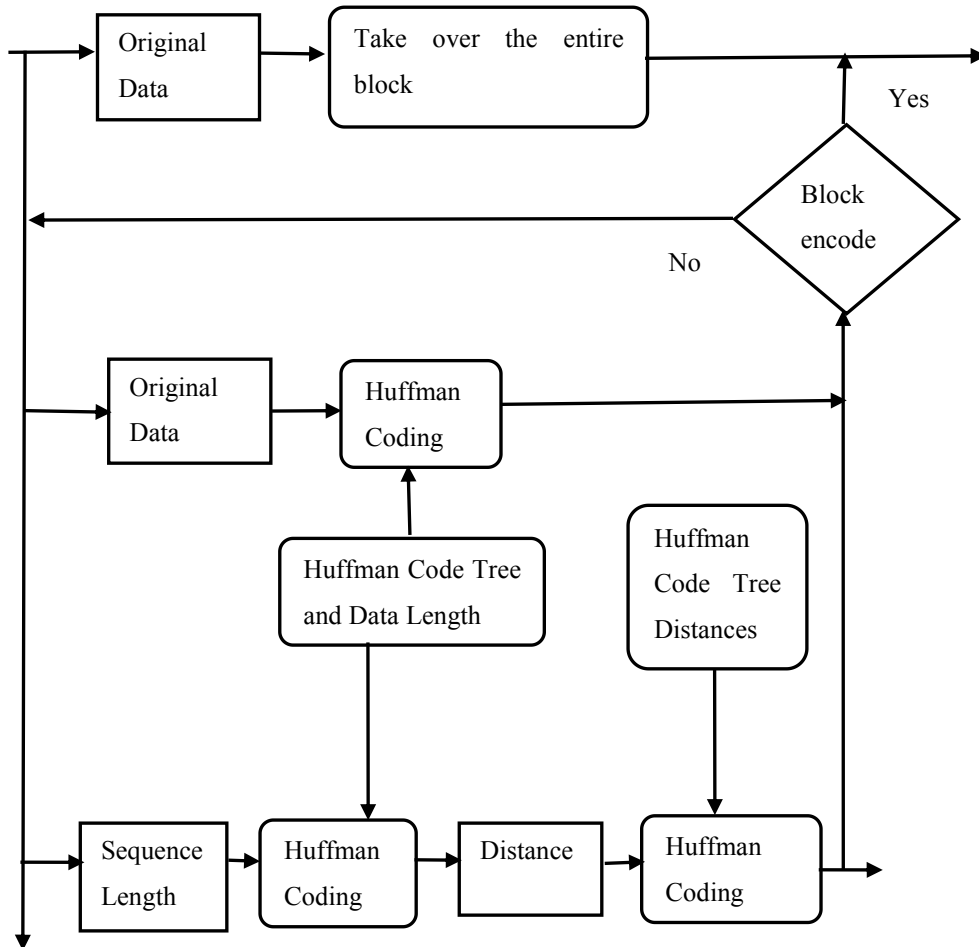


Fig. 6.2 Block diagram of deflate algorithm

6.3 ROI based compression scheme for PET images

The first step towards integration of the different modules of the work is preprocessing. The image under consideration is of the size 128 x 128 x 375. Here 2D processing of the image is done to reduce computational complexity. The image can have 3 views: axial, coronal and

sagittal. As the radiologists mostly prefer axial view for diagnosis, the image is considered slice by slice here in axial view. Thus there are 375 slices, with each slice having size of 128 x 128 pixels.

It is well known that PET image contains large amount of noise and much of this is located in the image area outside body torso. The image contains values as high as 65536 and values as low as 0. This creates lot of difficulties in differentiating the regions with lesions and those without as some of the organs have good amount of FDG intake. So we need to normalise the images and SUV normalisation is chosen in that context.

Some preprocessing is required before going for enhancement. The preprocessing steps include various morphological operations. The preprocessed image is subjected to enhancement. The enhancement scheme utilises stationary wavelet transform detail modulus and high boost filtering to provide an improvement in the appearance of the image. The enhanced image is applied to segmentation module.

The segmentation technique uses gabor annulus filtering and region growing to segment the ROI from the image. The challenges when segmenting ROI in the case of PET images is that the lesion should not be missed out and at the same time the image area identified as ROI should not be large. As the above said requirements are contradictory to a greater extent we have to find an optimum solution. The enhanced image is applied to a GA filter and the output is dilated, spur pixels removed, eroded, filled and boundary detected. The result is given as input to region growing. From the results of region growing a mask is prepared for ROI. Another mask can be obtained from this mask for BG.

The original image is multiplied with the ROI mask and region for low level of compression is separated. On this region SPIHT algorithm is applied. The wavelet used here is *bior4.4* and levels of decomposition used here is 4. The bit rate for compression, i.e., the maximum number of bits

that can be allocated, is chosen as 1. The bit stream output from SPIHT is encoded by arithmetic coding to remove coding redundancy.

The BG mask is used to provide compression at a higher rate for the image areas outside the ROI. The image is decomposed using *bior2.2* wavelet up to 4 levels. The linear prediction is done on the detail coefficients while approximation coefficients are not operated upon. The horizontal wavelet coefficients utilise row wise prediction while vertical coefficients are predicted column wise. The diagonal coefficients are handled in a slightly different way. The diagonal elements are extracted from the coefficient matrix and arranged in as each diagonal in a row. The diagonals are of different length and they are padded with zeros accordingly to arrange it in the form of a matrix. The prediction is performed on the rearranged diagonal coefficients, row wise. Using the retained detail coefficients and predictor coefficients the whole image can be reconstructed. The number of coefficients to be retained is decided. The coefficients, other than those needed for prediction are put to zero.

The resultant matrix is given as input to SPIHT algorithm and arithmetic coding. The bit rate is chosen as 0.1 to have more compression. The predictor coefficients are not integer values and hence applying SPIHT and arithmetic coding on them is very tedious. So deflate algorithm is implemented to handle the predictor coefficients. For decompressing we have decoding algorithm for deflate, arithmetic coding and SPIHT. Using the predictor coefficients, retained detail coefficients and approximation coefficients the original image is reconstructed. The whole process is repeated for all 375 slices.

6.3.1 Results and Discussion

The segmentation is performed with and without enhancement. The

need of enhancement step can be stressed in the case of images with lesions in lungs. Fig 6.3 shows the segmentation result with and without image enhancement on 168th slice in MM6_10 image, which has a lesion in lungs region. The white arrow in the sub images shows the position of lesion. From the figure it is clear that the lesion could become the part of ROI only when the image was preprocessed and enhanced before segmentation. The lesion is missing when the image is preprocessed but not enhanced and also when the image is either not preprocessed or enhanced. Many of the lungs lesions may be missed if the segmentation is done without enhancement.

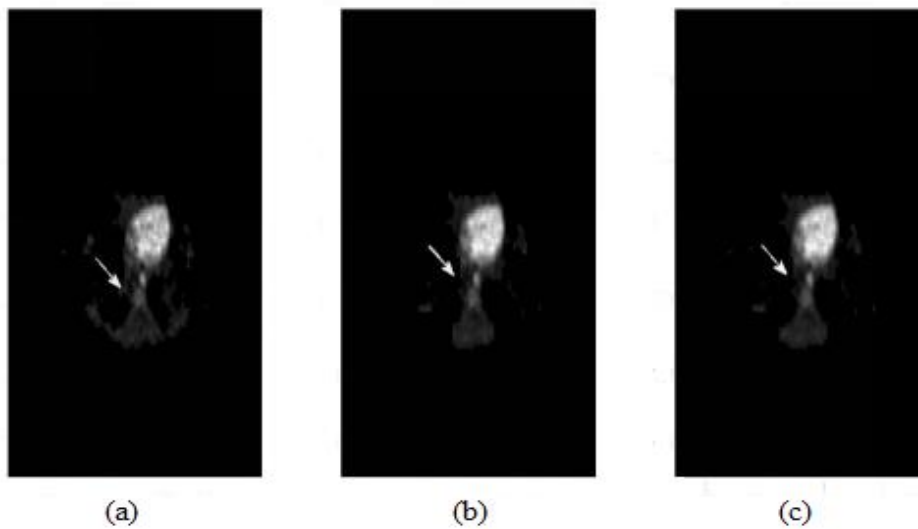


Fig. 6.3 Result of segmentation (lesion in lungs) (a) After preprocessing and enhancement (b) Enhancement only (c) Without preprocessing and enhancement

Fig 6.4 shows the result of the segmentation with and without preprocessing and enhancement on 203th slice in MM7_10 image, in which lesion is located in the liver region. It can be seen that the lesion is not lost in this case.

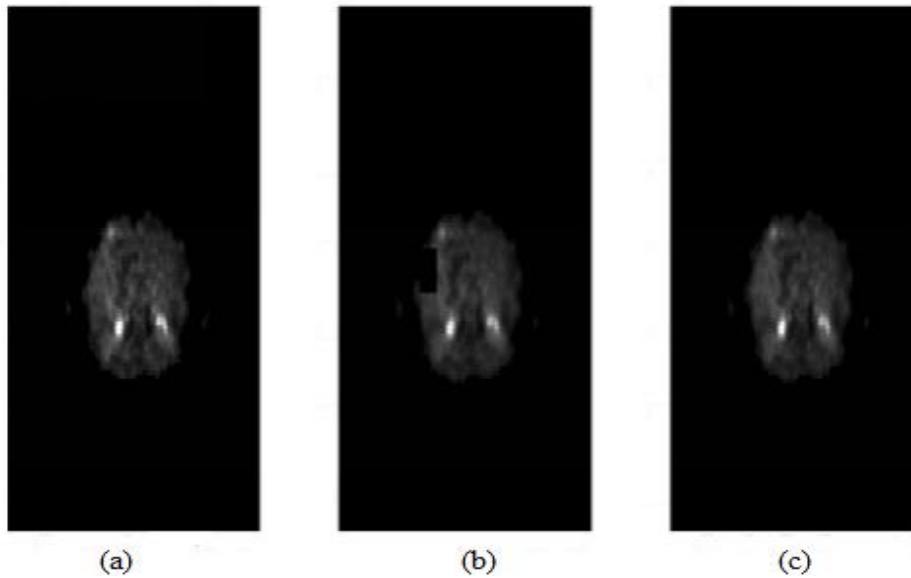


Fig. 6.4 Result of segmentation (lesion in liver) (a) After preprocessing and enhancement (b) Enhancement only (c) Without preprocessing and enhancement

Various parameters like compression ratio percentage, PSNR and MSSIM are studied by compressing and decompressing the image slices. The result of the study is illustrated with 121th slice of MM1_5. The performance measures of this slice are compared for different number of coefficients retained and also with standard true wavelet compression method using SPIHT algorithm in MATLAB. In general JPEG2000 standard, for lossy compression *bior4.4* is used while for lossless compression *bior2.2* is used. Since JPEG2000 is a standard technique, the same wavelets; *bior2.2* for ROI and *bior4.4* for BG along with SPIHT algorithm is adopted for this study. The level of wavelet decomposition is chosen as four for both ROI and BG. The results are tabulated in Table 6.1.

Table 6.1 Performance measures with number of coefficients retained

No.of Coefficients Retained	cr%	crroi%	crbg%	PSNR	MSSIM
2	2.4044	1.4084	0.9960	37.0399	0.96052
5	8.3858	1.4084	6.9775	37.0399	0.9605
8	16.5868	1.4084	15.1784	36.8534	0.9601
10	22.0529	1.4084	20.6445	36.8534	0.9601
12	27.5369	1.4084	26.1285	36.8534	0.9601
ROI-bior2.2 BG-bior4.4	16.5954	8.5510	8.0444	28.5873	0.9118

The compression ratio in the above table show the percentage of the amount of space required by the compressed data in comparison to the original size. In other words here cr% 2.4044 means, in the compressed form it requires only 2.4044% of the original image for storage. The cr% in the case of 8 retained coefficients is comparable to that of standard compression technique and we can observe that the proposed method in this case has better PSNR and MSSIM when compared with the other. The crroi% remains same in the table while crbg% increases with the increase in the number of retained coefficients. Even though there are instances where standard method has better cr% than the proposed one, it outperforms the other in case of PSNR and MSSIM.

The results of the proposed compression scheme and standard method are shown in Fig 6.5. The original image is slice 206 from MM2_10 image and this slice has got 2 lesions. The two white arrows in the original image shows the locations of the lesions. In the figure we can see that the result of the proposed method has clearly preserved the lesions

while in the standard method the results show that the lesions appear rather smeared or spread out. In the standard method even though the lesions appear more bright, the over all clarity of the picture seems to have been compromised.

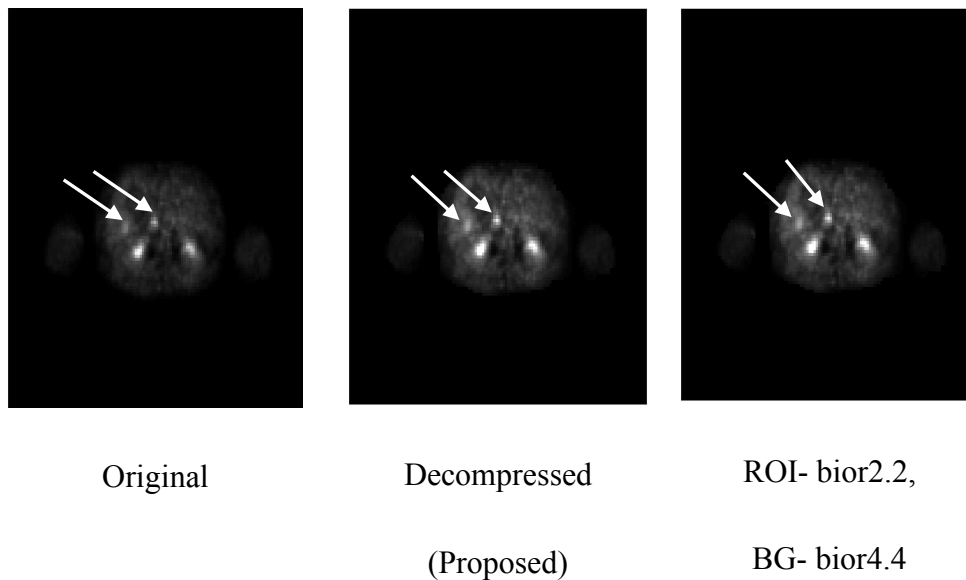


Fig. 6.5 Original & decompressed images of slice 206 of MM2_10

The performance measures are calculated for 4 level decomposition of ROI and BG is decomposed at different levels retaining 5 coefficients. The plot of cr%, against the levels of decomposition of BG are shown in Fig 6.6. In addition to the proposed method, jpeg2000 method mentioned earlier which is taken as reference for comparison, is also analysed here.

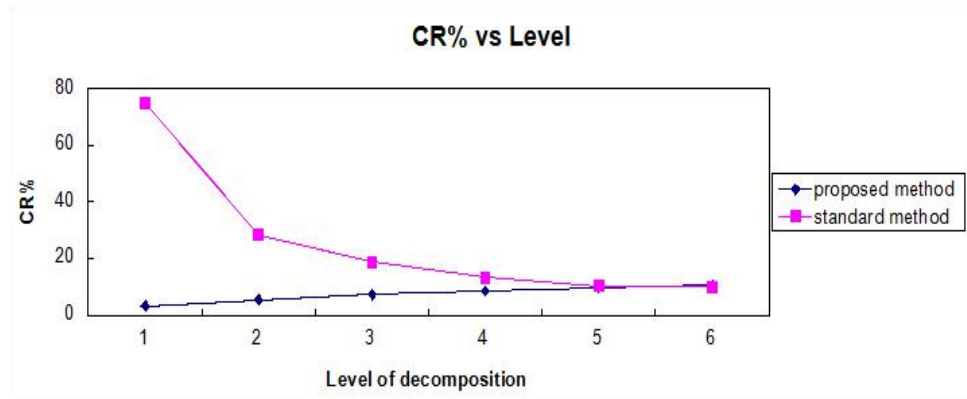


Fig. 6.6 Plot of cr percentage vs level of decomposition of BG

The $cr\%$ increases with the increase in the level of decomposition as we retain coefficients from each level. The standard method mentioned here has $cr\%$ decreasing with increase in the level of decomposition. From the figure it is evident that $cr\%$ is low in the case of proposed method. This means that the proposed method requires less space to accommodate the image in compressed form. When the level of decomposition approaches 5 and 6, the $cr\%$ becomes comparable to the referenced one.

The PSNR value for the the methods are plotted in the graph shown in Fig 6.7. The proposed method has obtained better PSNR when compared to the other methods. The blue line indicates values for proposed method, magenta for reference compression method. The proposed method works better in terms of PSNR for wavelet decomposition up to 6 levels for BG. The PSNR value is expressed here in decibels.

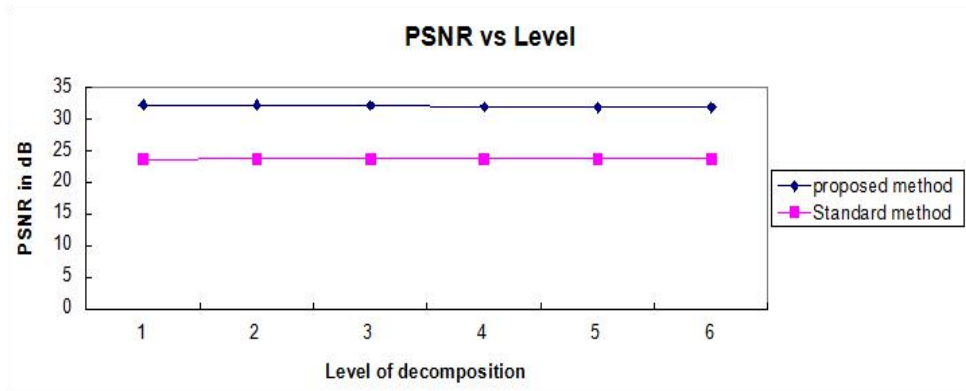


Fig. 6.7 Plot of PSNR vs level of decomposition of BG

Fig 6.8 show the comparison of the methods under consideration in terms of MSSIM. This value indicates the similarity of decompressed images with the original in numerical value.

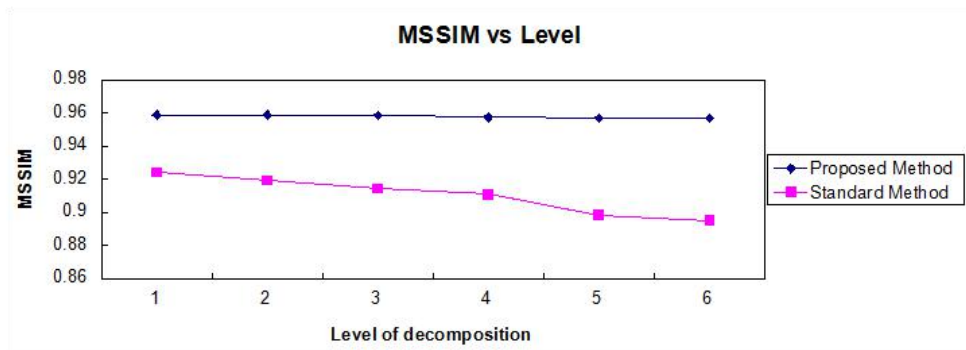


Fig. 6.8 Plot of MSSIM vs level of decomposition of BG

When the level of decomposition of both ROI and BG are same in the proposed method, for different number of retained coefficients the PSNR value and MSSIM value are almost same especially at lower levels. In the standard method, PSNR and MSSIM have lower value when compared with the proposed method. The results of the proposed method are consolidated taking the average values and is given in Table 6.2.

Table 6.2 Comparison of performance measures: images with and without lesions

Image Types \ PM	cr%	PSNR	MSSIM
With lesions	4.5944	31.4202	0.9358
Without lesions	4.5397	31.1212	0.9346
Average	4.5670	31.2707	0.9352

The above said are the results of the application of the proposed method on single slice of an image. The algorithm was applied on several images, each having 375 slices and belonging to two categories images containing lesion and those having no lesions as given in ONCOPET_DB database.

From Table 6.2 it is clear than the suggested method reduces the space required for storing the PET images to about 4.5% of its original size. We have an average value of 31.27dB as PSNR while average MSSIM is 0.9352. Many of the slices in an image does not have any lesion but we cannot reduce the storage space. This is because many of the organs have good FDG intake and since they are absolutely necessary for organ delineation which is another step in the process of diagnosis. Hence those image areas cannot be separated as BG.

In this section, the integration of developed enhancement method, segmentation method and compression technique to compress PET images

is examined. The method is found to be better when compared with standard ROI based compression using SPIHT algorithm. In the following section integration to suit a ROI based compression scheme for mammographic images is discussed.

6.4 ROI based compression for mammograms

For separating the ROI from mammograms, the method proposed here uses contrast improvement and eccentricity. The image is thresholded at first. The eccentricity of the different regions of resulting image is found. The regions having eccentricity between 0.5 and 1 are separated. Using the mask prepared from the above result, the segmented image is obtained. But the resultant image contains labels in the mammogram. The widely employed method of calculating the area of the region so as to remove the labels is applied here. In order to remove the label the area of the regions are found along with eccentricity. The regions having the above said eccentricity range and largest area is retained.

The resultant image is divided into blocks of size 128 x 128 pixels. Each block is enhanced using SWT, modulus maxima and high boost filtering technique and contrast difference (C_{Diff}) between original and processed image blocks are found out. The blocks that lie within the range specified by mean and standard deviation of C_{Diff} is retained while the rest are discarded. The lower range is the absolute value of the difference between mean and standard deviation of C_{Diff} and the upper range is the absolute of sum of mean and four times the standard deviation of C_{Diff} .

This gives us the breast region in the mammogram which can be used as ROI for further processing. The mask for compression is prepared from complement of found ROI. The image is decomposed into 4 levels using

1D DWT column wise and predictor coefficients for detail coefficients are identified. The approximation and some of the detail coefficients and equal number of predictor coefficients are retained and they form the compressed image. The prediction for the detail coefficients are done column wise. The column prediction compression technique developed is identified as suitable for compressing area outside ROI.

The results of this integration are discussed in the next sub section. The resultant images are evaluated both subjectively and objectively.

6.4.1 Results and Discussion

The compression and image quality after compression is quantified using measures like compression ratio, PSNR, NMSE, NAE and MSSIM. The performance measures of mdb002 are compared for different levels of wavelet decomposition and are given in Table 6.3. The optimum wavelet decomposition level for compression technique is identified as 6.

Table 6.3 Comparison of performance measures: various levels

Decomposition level	Compression ratio	PSNR	NMSE	NAE	MSSIM
4	6.97	42.46	0.00198	0.02387	0.98
5	12.19	40.07	0.00551	0.04316	0.96
6	19.32	38.06	0.00899	0.06725	0.95
7	26.95	34.95	0.02870	0.13424	0.89
8	33.03	32.85	0.04490	0.21866	0.82

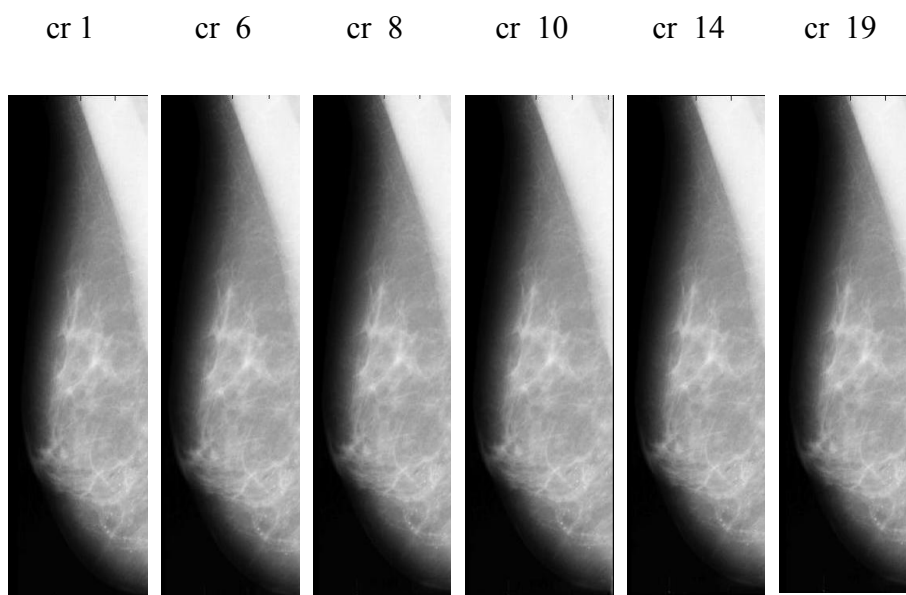


Fig. 6.9 Decompressed images of mdb245 compressed with different cr

The results of the compression scheme used on mdb245 for different compression ratios are shown in Fig 6.9. The performance measures PSNR, NAE, NMSE and MSSIM of mdb245 are compared for different compression ratios and are shown in Table 6.4

Table 6.4 Comparison of performance measures: different cr

Compression ratio	PSNR	NMSE	NAE	MSSIM
19	43.39	0.001026	0.026306	0.98
14	43.41	0.001000	0.026854	0.98
10	43.22	0.001148	0.029961	0.97
8	43.27	0.001072	0.028755	0.97
6	42.65	0.001249	0.030376	0.97

Table 6.5 given below tabulates the results of compression on different types of mammogram images using 6 levels of wavelet decomposition.

Table 6.5 Performance measures for compression

Type	Compression ratio	PSNR	NMSE	NAE	MSSIM
Circumscribed Masses	19.32	41.16	0.00358	0.03572	0.97265
Micro calcification	19.32	41.46	0.00298	0.03306	0.97605
Normal	19.32	42.59	0.00217	0.02720	0.97749
Architectural distortion	19.32	41.90	0.00190	0.02587	0.98283
Miscellaneous	19.32	42.93	0.00179	0.02329	0.98473
Spiculated Masses	19.32	41.83	0.00162	0.02817	0.97065
Average	19.32	41.98	0.00234	0.02889	0.97740

The recommendations on the achievable compression ratios published by Canadian Association of Radiologists (CAR), German Röntgen Society (DRG) and Royal College of Radiologists (RCR) suggests a compression ratio for mammographic images as 20 in UK, 25 in Canada and 15 in Germany [67]. Here a compression ratio of 19.32 which lies well within the acceptable range is achieved. Average PSNR value obtained is 41.98 which shows that the noise content in the image is too small to get noticed. The values of NMSE and NAE indicate that the difference between the original and decompressed image is very small. The measure

MSSIM measures the structural similarity between the two images and a value of 1 indicates that both the images have same structural content. Here we have obtained an average value of 0.9774. This indicates that the original and decompressed images have almost same structural content.

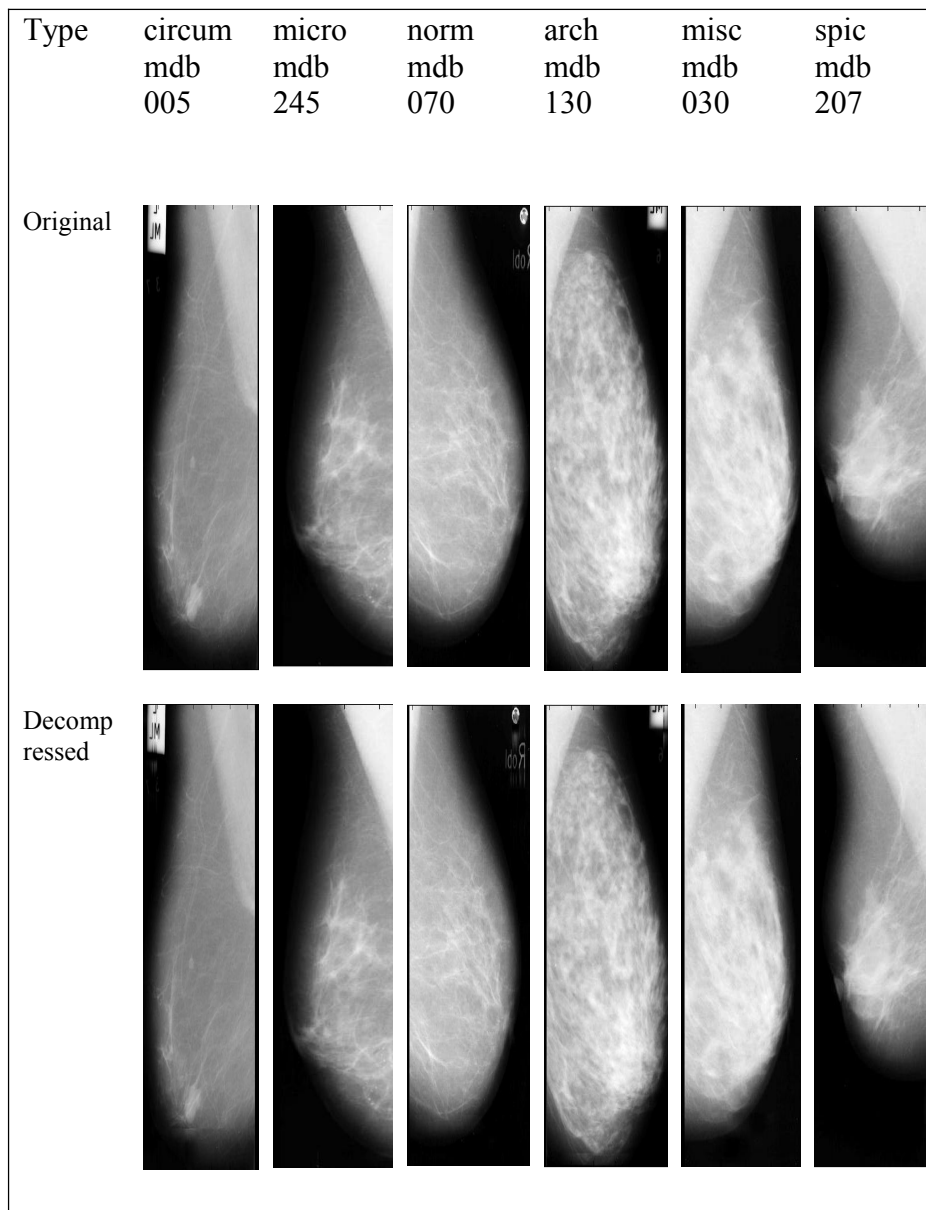


Fig. 6.10 Original and decompressed versions used in validation with $cr=19$

Fig 6.10 shows different types of images compared for compression ratio of 19.32. It can be visually experienced that the compression has not affected the quality of images. As samples, images from different categories - images having different types of abnormalities and normal images are selected. The original images and decompressed images which were compressed with the proposed algorithm using six levels of decomposition are shown in the figure.

6.5 Conclusion

The integration of developed enhancement, ROI separation using segmentation and compression methodologies in case of both PET and mammographic images are discussed. The compression for PET is validated against standard ROI method used for medical images while mammographic image compression is verified against the standards suggested by CAR, DRG and RCR. Even though CAR suggest compression ratio to be 5 for nuclear images the other two bodies have not specified any compression ratio for nuclear images.

CHAPTER 7

Conclusions

7.1 Introduction

This chapter presents a summary of the work done for compression of both PET and mammographic images. The future scope for the methods suggested for both types of images are also discussed. While working on compression of different types of medical images, the method for mammographic image discussed in this research work was obtained as a by product, as the focus was mainly on molecular images and mammographic images cannot be included in that category. The important conclusions derived from the study are highlighted in this chapter.

7.2 Summary, important conclusions and future scope

The method suggested in this work is fully automatic and requires no input from the user. The ROI based compression requires delineation of ROI and BG. Segmentation is needed at this stage while to have a better segmentation it is advisable to have an image enhancement. On separated ROI and BG the compression techniques are applied and the results are evaluated as a whole.

7.2.1 PET image compression

The first task in any image processing technique is identification of a suitable database for carrying out the study. ONCOPET_DB is identified as the one in case of PET images. The image is SUV normalised and slices are accessed axially one by one. After initial preprocessing and enhancing

the image using SWT, detail modulus and high boost filtering, the image is submitted to segmentation. The GA filtering and automatic seed selected region growing method developed are applied up on the enhanced image. A mask is obtained for ROI and a complement of that mask is utilised as mask for BG. The image area inside ROI is compressed using SPIHT and arithmetic coding algorithms while for BG linear prediction on 2D wavelet coefficient and deflation on prediction coefficients are made use of in addition to SPIHT and arithmetic coding.

The compression and image quality is evaluated both subjectively and objectively. The results are verified and validated. A PET image could be reduced to 4.5% of its original size. For example an image of size 24.5MB could be reduced to 1.1MB. The other measures used for objective evaluation are PSNR and MSSIM. The enhancement, segmentation and compression techniques developed are also evaluated separately. The successful lesion capture rate achieved using this technique is 93.8% and missed out lesions are primarily located in the lungs. The lack of a common reference database of images representing different imaging modalities and/or pathologies impedes a clear classification and comparison with many of the already known algorithms.

7.2.2 Mammographic image compression

The database to be used is identified as mini-MIAS database. The image is thresholded and eccentricities of different regions are found. The image is enhanced using developed enhancement technique using SWT and high boost filtering. The contrast difference in the original and enhanced image and eccentricity are used to segment ROI. Only the region outside ROI is compressed using the developed method of linear column wise prediction on column wise wavelet decomposed image. The compression and image quality is evaluated both subjectively and objectively. The

results are verified and validated for mammographic as well as other radiographic images. With slight modifications the algorithm developed here can be applied to other types of biomedical images. The algorithms developed were validated using other types of images also.

7.2.3 Future Scope

The methods suggested are computationally expensive for real time applications. The approaches to speed up the algorithm can be considered as one among the future scope of this research. The technique developed evidently has a weak spot and that being lungs. The lesions in the lungs are easy to be missed out. So methods can be suggested to improve successful capture of lungs lesion while separating ROI. Two dimensional processing of 3D images are done in the research work. 3D processing of the 3D images can also be considered as a future work. In case of method developed for mammograms, the well known lossless techniques like Huffman coding, Arithmetic coding, LZW etc can be studied for compression inside ROI. A study can be conducted on the developed method using embedded zero trees of wavelet transform (EZW), SPIHT and other algorithms. The generation of a standard database containing ample number of images having various abnormal images and ground truth at various resolution can be done as an extension.

References

- [1]. **Rollo, F.D.** (2002). Molecular imaging: An overview and clinical applications. *Radiology management* 25(3), 28-32.
- [2]. **Bonekamp, D., Hammoud, D.A., and Pomper, M.G.** (2010). Molecular imaging: Techniques and current clinical applications. *Applied Radiology* 39(5), 10-21.
- [3]. **Dougherty, G.** (2009). *Digital Image Processing for Medical Applications*, Cambridge University Press.
- [4]. **Dougherty, G.** (2011). *Medical Image Processing: Techniques and Applications*. Springer.
- [5]. **Leslie, D.A.** (2007). *Imaging for students*. 3rd Edition, Hodder Arnold.
- [6]. **Turkington, T. G.** (2011). PET Imaging Basics. In *Clinical PET-CT in Radiology : Integrated Imaging in Oncology* (pp. 21-28). Springer.
- [7]. **Tomei, S., Reilhac, A., Visvikis, D., Boussion, N., Odet, C., Giammarile, F., and Lartizien, C.** (2010). Oncopet DB: A freely distributed database of realistic simulated whole body 18F-FDG PET images for oncology. *IEEE Transactions on Nuclear Science*, 57(1), 246–255.
- [8]. **Gonzalez, R. C., and Woods, R. E.** (2002). *Digital Image Processing*. Prentice Hall.
- [9]. **Suckling, J., et al.** (1994). The mammographic image analysis society digital mammogram database. In *Excerpta Medica, International Congress Series* (Vol. 1069, pp. 375-378).
- [10]. **Ansari, M. A., and Anand, R. S.** (2008). Recent trends in image compression and its application in telemedicine and teleconsultation. In *XXXII National Systems Conference, NSC* (pp. 17-19).
- [11]. **Guan, H., Kubota, T., Huang, X., Zhou, X. S., and Turk, M.** (2006). Automatic hot spot detection and segmentation in whole body FDG-PET images. In *IEEE Int. Conference on Image Processing*, 2006 (pp. 85-88). IEEE.
- [12]. **Davis, P. B., and Abidi, M. A.** (1989) Enhancement of PET images. In *Medical Imaging* (pp. 584-591). International Society for Optics and Photonics.

- [13]. **Saadah, D., Sami,S., and Moussa, A.** (2006). Enhancement techniques for positron emission tomography (PET) imaging. In *4th Int. Multiconference on Computer Science and Information Technology*, (pp. 54–58).
- [14]. **Erlandsson, K. et.al** (2006). Quantitative wavelet domain image processing of dynamic PET data. In *28th Annual International Conference on Engineering in Medicine and Biology Society*, 2006. (EMBS '06) (pp. 2787–2790).
- [15]. **Erol, H., K "okl" ukaya, E., and Alkan, A.** (2006). Image enhancement in positron emission tomography using expectation maximization. *Seluk Journal of Applied Mathematics*, 7(2), 27–40.
- [16]. **Nagabhyru, S., Gudipalli, A., and Tirumala, R.** (2013). Hybrid composite edge detection algorithm for PET scanner images. *Journal of Theoretical & Applied Information Technology*, 57(1), 61–66.
- [17]. **Yavariabdi, A., Samir, C., and Bartoli, A.** (2011). 3D medical image enhancement based on wavelet transforms. *ALCoV-ISIT Universit'e d' Auvergne Clermont-Ferrand*, pp. 1–5, 2011.
- [18]. **Jin, Y., Angelini, E.D., Esserand, P.D., and Laine, A.F.** (2003). Denoising SPECT/PET images using cross-scale regularization. In *Medical Image Computing and Computer-Assisted Intervention-(MICCAI 2003)*, (pp. 32–40) Springer.
- [19]. **Grecchi, E., O'Doherty, J. and Turkheimer, F.** (2014). Exploiting anatomical information for PET image enhancement: A phantom experiment for algorithm validation. In *Nuclear Science Symposium and Medical Imaging Conference(NSSMIC 2014)*
- [20]. **Cheng, H., Cai, X., Chen, X., Hu, L., and Lou, X.** (2003). Computer-aided detection and classification of micro-calcifications in mammograms: A survey. *Pattern Recognition*, 36(12), 2967 – 2991.
- [21]. **Kimme-Smith, C., Gold, R., Bassett, L., Gormley, L. and Morioka, C.** (1989). Diagnosis of breast calcifications: comparison of contact, magnified, and television-enhanced images. *American Journal of Roentgenology*, 153(5), 963-967.
- [22]. **Biltawi, M., Al-Najdawi, N., and Tedmori, S.** (2012). Mammogram enhancement and segmentation methods: Classification, analysis, and evaluation. In *Int. Arab Conference on Information Technology (ACIT2012)*. (pp 477-85).

- [23]. **Schiabel, H., Santos, V.T., and Angelo, M.F.** (2008). Segmentation technique for detecting suspect masses in dense breast digitized images as a tool for mammography CAD schemes. In *ACM Symposium on Applied Computing*. (pp 1333-1337).
- [24]. **Sampat, M.P. and Bovik, A.C.** (2003). Detection of spiculated lesions in mammograms. In *25th Annual International IEEE Conference on Engineering in Medicine and Biological Society*. (pp.810-813) IEEE .
- [25]. **Dabour, W.** (2008). Improved wavelet based thresholding for contrast enhancement of digital mammograms. In *International Conference on Computer Science and Software Engineering, 2008* (Vol. 4, pp. 948-951). IEEE.
- [26]. **Kalra, P. K., and Kumar, N.** (2010). An automatic method to enhance microcalcifications using normalized Tsallis entropy. *Signal Processing*, 90(3), 952-958.
- [27]. **Jiang, J., Yao, B., and Wason, A. M.** (2005). Integration of fuzzy logic and structure tensor towards mammogram contrast enhancement. *Computerized Medical Imaging and Graphics*, 29(1), 83-90.
- [28]. **Yu, Z., and Bajaj, C.** (2004). A fast and adaptive method for image contrast enhancement. In *Int. Conference on Image Processing, (ICIP'04)*. (Vol. 2, pp. 1001-1004). IEEE.
- [29]. **Sivaramakrishna, R., Obuchowski, N. A., Chilcote, W. A., Cardenosa, G., and Powell, K. A.** (2000). Comparing the performance of mammographic enhancement algorithms: A preference study. *American Journal of Roentgenology*, 175(1), 45-51.
- [30]. **Chang, C. M., and Laine, A.** (1997). Enhancement of mammograms from oriented information. In *International Conference on Image Processing, 1997*.(Vol. 3, pp. 524-527). IEEE.
- [31]. **Gagnon, L., Lina, J. M., and Goulard, B.** (1995). Sharpening enhancement of digitized mammograms with complex symmetric Daubechies wavelets. In *IEEE 17th Annual Conference on Engineering in Medicine and Biology Society, 1995*, (Vol. 1, pp. 543-544). IEEE.

- [32]. **Papadopoulos, A., Fotiadis, D. I., and Costaridou, L.** (2008). Improvement of microcalcification cluster detection in mammography utilizing image enhancement techniques. *Computers in Biology and Medicine*, 38(10), 1045-1055.
- [33]. **Scharcanski, J., and Jung, C. R.** (2006). Denoising and enhancing digital mammographic images for visual screening. *Computerized Medical Imaging and Graphics*, 30(4), 243-254.
- [34]. **Stefanou, H., Kakouros, S., Cavouras, D., and Wallace, M.** (2005). Wavelet-based mammographic enhancement. In *Int. Conference on Network (INC)2005* .
- [35]. **KK, R., and Raju, G.** (2011). Enhancement of mammograms using tophat filtering and wavelet decomposition. *Journal of Computer and Mathematical Sciences*, 2(6), 780-898.
- [36]. **Erdt, M., Steger, S., and Sakas, G.** (2012). Regmentation: A new view of image segmentation and registration. *Journal of Radiation Oncology Informatics*, 4(1), 1-23.
- [37]. **Boudraa, A. O., and Zaidi, P. D. H.** (2006). Image segmentation techniques in nuclear medicine imaging. In *Quantitative analysis in nuclear medicine imaging* (pp. 308-357). Springer.
- [38]. **Amira, A., Chandrasekaran, S., Montgomery, D. W., and Uzun, I. S.** (2008). A segmentation concept for positron emission tomography imaging using multiresolution analysis. *Neurocomputing*, 71(10), 1954-1965.
- [39]. **Hsu, C. Y., Liu, C. Y., and Chen, C. M.** (2008). Automatic segmentation of liver PET images. *Computerized Medical Imaging and Graphics*, 32(7), 601-610.
- [40]. **Li, H., et. al .** (2008). A novel PET tumor delineation method based on adaptive region-growing and dual-front active contours. *Medical Physics*, 35(8), 3711-3721.
- [41]. **Bağci, U., Yao, J., Caban, J., Turkbey, E., Aras, O., and Mollura, D. J.** (2011). A graph-theoretic approach for segmentation of PET images. In *Annual International Conference on Engineering in Medicine and Biology Society, EMBC, 2011* (pp. 8479-8482). IEEE.

- [42]. **Yang, F., and Grigsby, P. W.** (2012). Delineation of FDG-PET tumors from heterogeneous background using spectral clustering. *European journal of radiology*, 81(11), 3535-3541.
- [43]. **Abdoli, M., Dierckx, R. A. J. O., and Zaidi, H.** (2013). Contourlet - based active contour model for PET image segmentation. *Medical Physics*, 40(8), 082507-1--082507-12.
- [44]. **Zeng, Z., Wang, J., Tiddeman, B., and Zwiggelaar, R.** (2013). Unsupervised tumour segmentation in PET using local and global intensity-fitting active surface and alpha matting. *Computers in Biology and Medicine*, 43(10), 1530-1544.
- [45]. **Foster, B. et al.** (2014). Segmentation of PET images for computer-aided functional quantification of tuberculosis in small animal models. *IEEE Transactions on BioMedical Engineering*, 61(3), 711–724.
- [46]. **Foster, B., Bagci, U., Mansoor, A., Xu, Z., and Mollura, D. J.** (2014). A review on segmentation of Positron Emission Tomography images. *Computers in Biology and Medicine*, 50, 76-96.
- [47]. **Zaidi, H., and El Naqa, I.** (2010). PET-guided delineation of radiation therapy treatment volumes: A survey of image segmentation techniques. *European Journal of Nuclear Medicine and Molecular imaging*, 37(11), 2165-2187.
- [48]. **Mahmood, F. H., and Hussein, A. A.** (2013). Automatic segmentation and identification of abnormal breast region in mammogram images based on statistical features. *Iraqi Journal of Science*, 54(3), 709-716.
- [49]. **Raba, D., Oliver, A., Martí, J., Peracaula, M., and Espunya, J.** (2005). Breast segmentation with pectoral muscle suppression on digital mammograms. In *Iberian Conference on Pattern Recognition and Image Analysis*, (pp. 471-478). Springer Berlin Heidelberg.
- [50]. **Nordin, Z. M., Isa, N. A. M., Zamli, K. Z., Ngah, U. K., and Aziz, M. E.** (2008). Semi-automated region of interest selection tool for mammographic image. In *Int. Symposium on Information Technology, 2008 (ITSim 2008)*. (Vol. 1, pp. 1-6). IEEE.
- [51]. **Qi, F., Wu, J., and Shi, G.** (2009). Extracting regions of attention by imitating the human visual system. In *IEEE Int. Conference on*

- Acoustics, Speech and Signal Processing, (ICASSP 2009)*. (pp. 1905-1908). IEEE.
- [52]. **Janaki, R., Tamilarasi, A., and Kumar, K.** (2012) Enhanced ROI (Region of Interest) algorithms for medical image compression. *International Journal of Computer Applications*, 38(2), 38-43.
- [53]. **Nagi, J., Kareem, S. A., Nagi, F., and Ahmed, S. K.** (2010). Automated breast profile segmentation for ROI detection using digital mammograms. In *IEEE EMBS Conference on Biomedical Engineering and Sciences (IECBES 2010)*. (pp. 87-92). IEEE.
- [54]. **Maitra, I. K., Sumathi, S. and Bandyopadhyay, S. K.** (2011). Accurate breast contour detection algorithms in digital mammogram. *International Journal of Computer Applications*, 25(5), 1-13.
- [55]. **Ashidi, I. M. N., and Ting, S. S.** (2012). Automatic segmentation and detection of mass in digital mammograms. In *11th Int. Conference on Telecommunications and Informatics*.(pp. 143-146) .
- [56]. **Yadav, R. and Dass, R.** (2012). Breast boundary detection in mammogram using entropy. *International Journal of Science and Research*, 1(3), 150-152.
- [57]. **Yapa, R. D. and Harada, K.** (2007). Breast skin-line estimation and breast segmentation in mammograms using fast-marching method. *International Journal of Medical, Health, Biomedical and Pharmaceutical Engineering*, 1 (5), 217-225.
- [58]. **Wani, I. U. I., Hanumantharaju, M.C., and Gopalakrishna, M. T.** (2014). Review of mammogram enhancement techniques for detecting breast cancer. In *Int. Conference on Information and Communication Technologies ICICT(1)*. (pp. 6-10). IJCA.
- [59]. **Sukanesh, R., Harikumar, R., Balaji N. S., and Balasubramaniam, S. R.** (2009). Analysis of image compression by minimum relative entropy & restoration through region growing techniques for medical images. *Engineering Letters* ,14(1),84-89.
- [60]. **Grgic, M., Ravnjak, M., and Zovko-Cihlar, B.** (1999). Filter comparison in wavelet transform of still images. In *IEEE Int. Symposium on Industrial Electronics, (ISIE'99)*, (Vol. 1, pp. 105-110), IEEE.

- [61]. **Eskicioglu, A. M. and Fisher, P. S.** (1995). Image quality measures and their performance. *IEEE Transactions on Communications*, 43(12), 2959-2965.
- [62]. **Makhoul, J.** (1975). Linear prediction- A tutorial review. In *IEEE*, 63(4), 561-579.
- [63]. **Huang, J. S., Nguyen, D. T., Negnevitsky, M., and Phillips, C. J. E.** (1999). Correlation properties of wavelet transform and applications in image coding. In *5th Int. Symposium on Signal Processing and Its Applications, (ISSPA'99)*. (Vol. 2, pp. 611-614).
- [64]. **Udomhunsakul, S., and Hamamoto, K.** (2004). Wavelet filters comparison for ultrasonic image compression. In *IEEE Region 10 Conference TENCN 2004*. (pp. 171-174). IEEE.
- [65]. **Villasenor, J.D., Belzer, B. and Liao, J.** (1995). Wavelet filter evaluation for image compression. *IEEE Transactions on Image Processing*, 4(8), 1053-1060.
- [66]. **Doukas, C. N., Maglogiannis, I., and Kormentzas, G.** (2006). Medical image compression using wavelet transform on mobile devices with ROI coding support. In *27th Annual Int. Conference on Engineering in Medicine and Biology Society, (IEEE-EMBS 2005)*, (pp. 3779-3784). IEEE.
- [67]. **European Society of Radiology(ESR).** (2011). Usability of irreversible image compression in radiological imaging. A position paper by the European Society of Radiology (ESR). *Insights Imaging*, 2(2), 103-115.
- [68]. **Vidhya,K. and S. Shenbagadevi, S.** (2009). Performance analysis of medical image compression. In *Int. Conference on Signal Processing Systems*. (pp. 979-983).
- [69]. **Shahhoseini, E., Nejad, N. A., Behnam, H., and Shahhoseini, A.** (2010). A new approach to compression of medical ultrasound images using wavelet transform. In *Third Int. Conference on Advances in Circuits, Electronics and Micro-Electronics (CENICS 2010)* (pp. 40-44). IEEE.
- [70]. **Kai, X., Jie, Y., Min, Z. Y., and Liang, L. X.** (2005). HVS-based medical image compression. *European Journal of Radiology*, 55(1), 139-145.
- [71]. **Bairagi, V. K., and Sapkal, A. M.** (2009). Selection of wavelets for medical image compression. In *Int. Conference on Advances*

- in *Computing, Control, & Telecommunication Technologies, (ACT'09)*. (pp. 678-680). IEEE.
- [72]. **Knezović, J., et.al.** (2007). Application of novel lossless compression of medical images using prediction and contextual error modeling. *Collegium antropologicum*, 31(4), 1143-1150.
- [73]. **Chen, Y. T., and Tseng, D. C.** (2007). Wavelet-based medical image compression with adaptive prediction. *Computerized Medical Imaging and Graphics*, 31(1), 1-8.
- [74]. **Menegaz, G.** (2006). Trends in medical image compression. *Current Medical Imaging Reviews*, 2(2), 165-185.
- [75]. **Zukoski, M. J., Boulton, T., and Iyriboz, T.** (2006). A novel approach to medical image compression. *International Journal of Bioinformatics Research and Applications*, 2(1), 89-103.
- [76]. **Ansari, M. A., and Anand, R. S.** (2008). DWT based context modeling of medical image compression. In *XXXII National Systems Conference, NSC* (pp. 17-19).
- [77]. **Ansari, M. A., and Anand, R. S.** (2008). Context based medical image compression with application to ultrasound images. In *Annual IEEE India Conference, (INDICON 2008)*. (Vol. 1, pp. 28-33). IEEE.
- [78]. **Dahlbom, M. et.al** (1992). Whole-body positron emission tomography. Part I. Methods and performance characteristics. *The Journal of Nuclear Medicine* 33(6) 1191-1199.
- [79]. **Tsai, M. J., Villasenor, J. D., Chatziioannou, A., and Dahlbom, M.** (1995). Positron Emission Tomograph compression by using wavelet transform. In *IEEE Conference on Nuclear Science Symposium and Medical Imaging, (NSSM'95)* (Vol. 3, pp. 1434-1437). IEEE.
- [80]. **Seeram, E.** (2006). Irreversible compression in digital radiology. A literature review. *Radiography*, 12(1), 45-59.
- [81]. **Dahlbom, M., Gardner, K. A., Chatziioannou, A., and Hoh, C. K.** (1994). Whole body PET image compression. In *IEEE Nuclear Science Symposium and Medical Imaging, (NSSM '94)*. (Vol. 3, pp. 1394-1398). IEEE.
- [82]. **Masood, S., Sharif, M., Yasmin, M., Raza, M., and Mohsin, S.** (2013). Brain image Compression: A brief survey. *Research Journal of Applied Sciences*, 5(1), 49-59.

- [83]. **Wang, J., and Huang, H. K.** (1996). On-line structure-lossless digital mammogram image compression. In *Medical Imaging: Image Display 1996* (Vol. 2707, pp. 456-462). International Society for Optics and Photonics.
- [84]. **Wong, H. S., Guan, L., and Hong, H.** (1995). Compression of digital mammogram databases using a near-lossless scheme. In *Int. Conference on Image Processing, (ICIP '95)*, (Vol. 2, pp. 21-24). IEEE.
- [85]. **Grinstead, B., Sari-Sarraf, H., Gleason, S., and Mitra, S.** (2000). Content-based compression of mammograms for telecommunication and archiving. In *13th IEEE Symposium on Computer-Based Medical Systems, (CBMS 2000)*. (pp. 37-42).
- [86]. **Askelöf, J., Carlander, M. L., and Christopoulos, C.** (2002). Region of interest coding in JPEG 2000. *Signal Processing: Image Communication*, 17(1), 105-111.
- [87]. **Tahoces, P. G., Varela, J. R., Lado, M. J., and Souto, M.** (2008). Image compression: Maxshift ROI encoding options in JPEG2000. *Computer Vision and Image Understanding*, 109(2), 139-145
- [88]. **Bartrina-Rapesta, J., Serra-Sagristà, J., and Aulí-Llinàs, F.** (2011). JPEG2000 ROI coding through component priority for digital mammography. *Computer Vision and Image Understanding*, 115(1), 59-68.
- [89]. **Bankman, I.** (Ed.). (2008). *Handbook of medical image processing and analysis*. Academic press.
- [90]. **Demirel, H., and Anbarjafari, G.** (2011). Image Resolution enhancement by using Discrete and Stationary Wavelet Decomposition. *IEEE Transactions on Image Processing*, 20(5), 1458-1460.
- [91]. **Nason, G. P., and Silverman, B. W.** (1995). The stationary wavelet transform and some statistical applications. In *Wavelets and statistics* (pp. 281-299). Springer.
- [92]. **Jumah, A.A.** (2013). Denoising of an Image Using Discrete Stationary Wavelet Transform and Various Thresholding Techniques. *Journal of Signal and Information Processing*, 4(1), 33-41.
- [93]. **Qi, X., Tyler, J. M., and Pianykh, O. S.** (2000). Diagnostically lossless medical image compression via wavelet-based

- background noise removal. In *AeroSense 2000* (pp. 470-480). International Society for Optics and Photonics.
- [94]. **Nowak, R. D., and Baraniuk, R. G.** (1996). Optimally weighted highpass filters using multiscale analysis. In *IEEE Southwest Symposium on Image Analysis and Interpretation*. (pp. 224-229). IEEE.
- [95]. **Prat, W. K.** (2001). *Digital Image Processing*. John Wiley.
- [96]. **Jain, A. K.** (1989). *Fundamentals of Digital Image Processing*. Prentice Hall.
- [97]. **Zaveri, T., and Zaveri, M.** (2011). A novel region based multimodality image fusion method. *Journal of Pattern Recognition Research*, 6(2), 140-153.
- [98]. **Wu, S., Zhu, Q., Yang, Y., and Xie, Y.** (2013). Feature and Contrast Enhancement of Mammographic Image based on Multiscale Analysis and Morphology. *Computational and Mathematical Methods in Medicine*.
- [99]. **Agaian, S. S., Panetta, K., and Grigoryan, A. M.** (2000). A new measure of image enhancement. In *IASTED Int. Conference on Signal Processing & Communication*. (pp. 19-22). Citeseer.
- [100]. **Kim, C. K., Gupta, N. C., Chandramouli, B., and Alavi, A.** (1994). Standardized uptake values of FDG: body surface area correction is preferable to body weight correction. *The Journal of Nuclear Medicine*, 35(1), 164-167.
- [101]. **Rhodes, A., and Bai, L.** (2011). Circle Detection Using a Gabor Annulus. In *British Conference on Machine Vision, (BMVC 2011)*, (pp. 108.1-108.11).
- [102]. **Ghule, A. G., and Deshmukh, P. R.** (2012). Image segmentation available techniques, open issues and region growing algorithm. *Journal of Signal and Image Processing*, 3(1), 71-75.
- [103]. **Yang, Y., Peng, H., Jiang, Y., Huang, X., and Zhang, J.** (2013). A Region-based Image Segmentation method under P-systems*. *Journal of Information & Computational Science*, 10(10), 2943-2950.
- [104]. **Zhang, H., Fritts, J. E., and Goldman, S. A.** (2008). Image segmentation evaluation: A survey of unsupervised methods. *Computer Vision and Image Understanding*, 110(2), 260-280.

- [105]. **Chabrier, S., Emile, B., Laurent, H., Rosenberger, C., and Marché, P.** (2004). Unsupervised Evaluation of Image Segmentation- Application to Multi-spectral images. In *17th Int. Conference on Pattern Recognition, (ICPR 2004)*. (Vol. 1, pp. 576-579). IEEE.
- [106]. **Chabrier, S., Rosenberger, C., Laurent, H., Emile, B., and Marché, P.** (2004). Evaluating the segmentation result of a gray-level image. In *12th European Conference on Signal Processing, (EUSIPCO'04)*, (pp. 953-956). IEEE.
- [107]. **Levine, M. D., and Nazif, A. M.** (1985). Dynamic measurement of computer generated image segmentations. *IEEE Transactions on Pattern Analysis and Machine Intelligence*, 7(2), 155-164.
- [108]. **Philipp-Foliguet, S., and Guigues, L.** (2008). Multi-scale criteria for the evaluation of image segmentation algorithms. *Journal of Multimedia*, 3(5), 42-56.
- [109]. **Ouattara, S., Loum, G. L., Clément, A., and Vigouroux, B.** (2011). Analysis of the relevance of evaluation criteria for multi-component image segmentation. *Journal of Software Engineering and Applications*, 4(6), 371-378.
- [110]. **S. Chabrier, S., Emile, B., Rosenberger, C., and Laurent, H.** (2006). Unsupervised performance evaluation of image segmentation. *EURASIP Journal on Applied Signal Processing*, 2006, 1–12.
- [111]. **Dietenbeck, T., Alessandrini, M., Friboulet, D., and Bernard, O.** (2010). CREASEG: A free software for the evaluation of image segmentation algorithms based on level-set. In *17th IEEE International Conference on Image Processing (ICIP 2010)*. (pp. 665-668).
- [112]. **Barbhuiya, A. H. M. J. I and Hemachandran, K.** (2013). Wavelet Transformations and Its Major Applications in Digital Image Processing. *International Journal of Engineering*, 2(3), 1-5.
- [113]. **Chun-Lin, R., and Liu.** (2010). A Tutorial of the Wavelet Transform
- [114]. **Lewis, A.S. and Knowles, G.** (1992). Image Compression Using the 2-D Wavelet Transform. *IEEE Transactions on Image Processing*, 1(2), 244-250.
- [115]. **Maragos, P. Schafer, R.W. and Mersereau, R.M.** (1984). Two-Dimensional Linear Prediction and Its Application to Adaptive

Predictive Coding of Images processing in the context of a visual model. *IEEE Transactions on Acoustics, Speech and Signal Processing*, 32(6), 1213-1229.

- [116]. **Rajagopalan, R., Orchard, M.T., and K. Ramchandran, K.** (1996). Optimal Supports for Linear Predictive Models. *IEEE Transactions on Signal Processing*, 44(12), 3150-3153.
- [117]. **Hu, J. H., Wang, Y. and Cahill, P. T.** (1997). Multispectral Code Excited Linear Prediction Coding and Its Application in Magnetic Resonance Images. *IEEE Transactions on Image Processing*, 6(11), 1555-1566.
- [118]. **Hayes, M. H.** (1996). *Statistical Digital Signal Processing and Modeling*. John Wiley.
- [119]. **Wang, Z., Bovik, A.C., Sheikh, H.R. and Simoncelli, E.P.** (2004). Image Quality Assessment: From Error Visibility to Structural Similarity. *IEEE Transactions on Image Processing*, 13(4), 600-612.
- [120]. <http://sun.iinf.polsl.gliwice.pl/~rstaros/mednat/index.html>.
- [121]. Carney, T.: ModelFest Web Site
<http://www.neurometrics.com/projects/Modelfest/IndexModelfest.html>
- [122]. **Carney, T., et.al.** (1999). The development of an image/threshold database for designing and testing human vision models. In *Electronic Imaging '99* (pp. 542-551). International Society for Optics and Photonics.
- [123]. **Said, A., and Pearlman, W.A.** (1996). A new, fast and efficient image codec based on set partitioning in hierarchical trees. *IEEE Transactions on Circuits Systems for Video Technology*, 6(3), 243-250.
- [124]. **Sayood, K.** (2000). *Introduction to data compression*. 2nd edition, San Francisco, Calif.: Morgan Kaufmann.
- [125]. **Printz, H.** (1994). A tutorial on Arithmetic Coding.
- [126]. **Feldspar, A.** An explanation of the deflate algorithm. Available at <http://www.zlib.org/feldspar.html>

Publications

Journals

1. **Devi, P. A.** and **Mini, M. G.** (2016). PET Image Segmentation Based on Gabor Annulus Filtering and Region Growing. *International Journal of Computer Theory and Engineering*, 8(5), 409-414.
2. **Mini, M.G.** and **Devi, P, A.** (2016). Enhancement Technique for PET Images Using Stationary Wavelet Transform and High Boost Filtering. *International Journal of Electronics and Communication Engineering* , 5(1), 55-66.
3. **Devi, P. A.** and **Mini, M. G.** (2015). Mammographic Image Enhancement based on SWT and High Boost Filtering. *International Journal of Computer Theory and Engineering*, 7(5), 374-378.
4. **Devi, P. A.** and **Mini, M. G.** (2012). Compression of Medical Images by Prediction on Wavelet Transform Coefficients. *Bonfring International Journal of Advances in Image Processing*, 2(4), 8-16.
5. **Devi, P. A.** and **Mini, M. G.** (2012). Gray Scale Image Compression based On Wavelet Transform and Linear Prediction. *The International Journal of Multimedia and its Applications*, 4(1) 47-62.

Conferences

1. **Devi, P. A.** and **Mini, M. G.** (2015). Segmentation of Mammographic Images by Eccentricity and Contrast difference. *National Conference on VLSI Embedded Systems, Opto Electronics and Signal Processing, (NCVOS 2015)* Kochi, to be published by IEEE Xplore.
2. **Devi, P. A.** and **Mini, M. G.** (2014). Mammographic Image Enhancement Based on SWT and High Boost Filtering. In *4th Int. Conference on Computer Design and Engineering, (ICCDE 2014)* .
3. **Devi, P. A.** and **Mini, M. G.** (2012). Compression of Computed Radiographic Images using Linear Prediction on Wavelet

- Coefficients. In *International Conference on Advances in Computing and Communications (ICACC 2012)*. (pp. 130-133). IEEE.
4. **Devi, P. A., and Mini, M. G.** (2012). Compression of gray scale images using linear prediction on wavelet coefficients. In *2nd Int. Conference on Computer Science and Information Technology, (CCSIT 2012)*, (Vol.86, pp. 49-58). Springer Berlin Heidelberg.

Resume

Personal profile

Name: Arya Devi P S

Sex: Female

Date of Birth: 10-05-1975

Area of Interest: Digital image processing ,
Information Theory & Coding

Languages known: English, Hindi, Malayalam, Tamil

Computer Skills: C, C++, Visual Basic, MATLAB

Professional Experience: 10 years of teaching experience.

Worked as Research Scholar and Project Fellow in the field of image processing and compression in Department of Electronics, Model Engineering College, Thrikkakkara



Professional Memberships:

Life member- ISTE, Life member- IETE, Member- IEEE.

Publications

International/ National Conferences : 4 Journal Publications : 5

Qualifications	Branch /Specialization	Year	University	Percentage /CGPA
B. E	Electronics & Communication Engineering	1996	Bharatidasan University	65.1 %
M.Tech	Applied Electronics	2008	Mahatma Gandhi University	74.1%
PhD	Image Processing	Doing	CUSAT (Model Engg. College)	GPA 8.25 (Course Work)

Email Address : aryabinoy@gmail.com, aryaps@mec.ac.in

Permanent Address : “Anima”, Parat Lane, Aluva, Kerala,

PIN: 683101

Phone No : 0484-2624595(Res), 9446128296(Mob)